

สภาพการนำโปรตอนในแบเรียมเซอร์โคเนตที่โดไปด้วยอิตเทียม
สำหรับเซลล์เชื้อเพลิงไดเรกต์เอทานอลที่อุณหภูมิระดับกลาง



นางสาวอรธิดา โกษาแสง

ศูนย์วิทยทรัพยากร จุฬาลงกรณ์มหาวิทยาลัย

วิทยานิพนธ์นี้เป็นส่วนหนึ่งของการศึกษาตามหลักสูตรปริญญาวิทยาศาสตรมหาบัณฑิต

สาขาวิชาเทคโนโลยีเซรามิก ภาควิชาวัสดุศาสตร์

คณะวิทยาศาสตร์ จุฬาลงกรณ์มหาวิทยาลัย

ปีการศึกษา 2552

ลิขสิทธิ์ของจุฬาลงกรณ์มหาวิทยาลัย

PROTON CONDUCTIVITY IN Y-DOPED BARIUM ZIRCONATE FOR
INTERMEDIATE TEMPERATURE DIRECT ETHANOL FUEL CELL



Miss Onthida Kosasang

ศูนย์วิทยทรัพยากร
จุฬาลงกรณ์มหาวิทยาลัย

A Thesis Submitted in Partial Fulfillment of the Requirements
for the Degree of Master of Science Program in Ceramic Technology

Department of Materials Science

Faculty of Science

Chulalongkorn University

Academic Year 2009

Copyright of Chulalongkorn University

Thesis Title **PROTON CONDUCTIVITY IN Y-DOPED BARIUM
ZIRCONATE FOR INTERMEDIATE TEMPERATURE
DIRECT ETHANOL FUEL CELL**


By **Miss Onthida Kosasang**

Field of Study **Ceramic Technology**

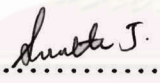
Thesis Advisor **Rojana Pornprasertsuk, Ph.D.**

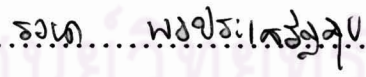
Thesis Co-Advisor **Sujarinee Kochawattana, Ph.D.**


Accepted by the Faculty of Science, Chulalongkorn University in
Partial Fulfillment of the Requirements for the Master's Degree



..... Dean of the Faculty of Science
(Professor Supot Hannongbua, Dr.rer.nat.)


THESIS COMMITTEE


..... Chairman
(Assistant Professor Sirithan Jiemsirilers, Ph.D.)


..... Thesis Advisor
(Rojana Pornprasertsuk, Ph.D.)


..... Thesis Co-Advisor
(Sujarinee Kochawattana, Ph.D.)


..... Examiner
(Assistant Professor Thanakorn Wasanapiarnpong, Ph.D.)


..... External Examiner
(Pongpan Chindaudom, Ph.D.)

อริศา โภษาแสง : สภาพการนำโปรตอนในแบเรียมเซอร์โคเนตที่โคปด้วยอิตเทรียมสำหรับ เซลล์เชื้อเพลิง ไคเรกต์เอทานอลที่อุณหภูมิระดับกลาง. (PROTON CONDUCTIVITY IN Y-DOPED BARIUM ZIRCONATE FOR INTERMEDIATE TEMPERATURE DIRECT ETHANOL FUEL CELL) อ. ที่ปรึกษาวิทยานิพนธ์หลัก: คร. รจนา พรประเสริฐสุข, อ. ที่ปรึกษาวิทยานิพนธ์ร่วม: คร.ศุจาริณี คชวัฒน์, 95 หน้า.

งานวิจัยนี้ได้ทำการศึกษาผลของความเข้มข้นของอิตเทรียมต่อคุณสมบัติทางโครงสร้าง และสภาพการนำโปรตอนใน $BaZr_{1-x}Y_xO_{3-\delta}$ (BYZ) ได้ทำการเตรียม $BaZr_{1-x}Y_xO_{3-\delta}$ (BYZ) แบบแผ่นหนาที่ $x = 0.06-0.4$ จากวิธีปฏิบัติวิชาสถานะของแข็ง เมื่อศึกษาโครงสร้างจุลภาคของ BYZ แบบแผ่นหนา แสดงให้เห็นว่าโครงสร้างที่ผิวหน้าของ BYZ แบบแผ่นหนามีความหนาแน่นต่ำกว่าเนื้อด้านใน ซึ่งคาดว่าเป็นผลจากการสูญเสีย BaO ด้วยการระเหยเป็นไอ เมื่อวัดค่าความหนาแน่นเฉลี่ยของ BYZ แบบแผ่นหนาพบว่ามีความหนาแน่นมากกว่า 95% และไม่มีรูที่ต่อเนื่องจึงทำให้สามารถช่วยป้องกันการรั่วซึมของเอทานอลได้ ผลของการวัดสภาพการนำโปรตอนพบว่า ค่าสภาพการนำโปรตอนในเนื้อเกรนมีค่าสูงกว่าที่ขอบเกรน และมีค่าสูงสุดเมื่อ $x=0.1$ ซึ่งมีค่าพลังงานกระตุ้นที่ 0.42-0.47 eV ในขณะที่สภาพการนำโปรตอนที่ขอบเกรน สูงสุดเมื่อ $x=0.2$ และมีค่าพลังงานกระตุ้นอยู่ในช่วง 0.68-0.82 eV ซึ่งเมื่อรวมเป็นสภาพการนำโปรตอนรวมของวัสดุ $BaZr_{0.8}Y_{0.2}O_{3-\delta}$ มีสภาพการนำโปรตอนสูงที่สุด

แผ่นฟิล์มบางของ BYZ ขึ้นรูปจากเทคนิคโค-สปีดเตอริงและสปีดเตอริง 2 ชั้นตอน มีความหนาอย่างสม่ำเสมอที่ 140-200 nm และ ไม่พบรูพรุนบนแผ่นฟิล์ม เมื่อศึกษาโครงสร้างทางเฟสในตัวอย่างที่ขึ้นรูปด้วยเทคนิคโค-สปีดเตอริง พบว่าเมื่อใช้พลังงานบนทาร์เกต Y มาก ปริมาณที่มากขึ้นของ Y ก่อให้เกิดการแยกเฟสของ Y_2O_3 ในขณะที่ตัวอย่างที่ขึ้นรูปจากเทคนิค สปีดเตอริง 2 ชั้นตอน เมื่อเพิ่มมุมในการเปิดมากจะเกิดการแยกเฟสของ Y_2O_3 โคป ZrO_2 เพิ่มมากขึ้นตามลำดับ เมื่อวัดค่าสภาพการนำโปรตอนพบว่าสภาพการนำโปรตอนของแผ่นฟิล์มบาง BYZ มีค่าสูงกว่าแบบแผ่นหนาประมาณ 100 เท่า ซึ่งความแตกต่างที่เกิดขึ้น คาดว่าจะเกิดจากความแตกต่างระหว่างโครงสร้างจุลภาค ขนาดเกรน วิธีการวัด และกลไกการนำไอออนในชั้นงาน

ภาควิชา วัสดุศาสตร์..... ลายมือชื่อนิติศ..... อริศา โภษาแสง
สาขาวิชา ...เทคโน โลยีเซรามิก ลายมือชื่อ อ.ที่ปรึกษาวิทยานิพนธ์หลัก... อ.รจนา พรประเสริฐสุข
ปีการศึกษา2552 ลายมือชื่อ อ.ที่ปรึกษาวิทยานิพนธ์ร่วม ... ศุจาริณี คชวัฒน์

5072559823 : MAJOR CERAMIC TECHNOLOGY

KEYWORDS : BARIUM ZIRCONATE/ PROTON CONDUCTOR/ FUEL CELL

ONTHIDA KOSASANG : PROTON CONDUCTIVITY IN Y-DOPED BARIUM ZIRCONATE FOR INTERMEDIATE TEMPERATURE DIRECT ETHANOL FUEL CELL. THESIS ADVISOR: ROJANA PORNPRASERTSUK, Ph.D., THESIS CO-ADVISOR: SUJARINEE KOCHAWATTANA, Ph.D., 95 pp.

$BaZr_{1-x}Y_xO_{3-\delta}$ (BYZ) pellets with $x=0.06-0.4$ were fabricated by solid state reactions with a relative density higher than 95%. The microstructures of the BYZ pellets reveal that BYZ surface has higher porosity than that of bulk, which may arise from the BaO evaporation during sintering process. The impedance analysis shows that the higher values of the bulk conductivity than those of the grain boundary. The highest bulk proton conductivity is obtained at $x=0.1$, while the highest grain boundary and total proton conductivity is at $x=0.2$. The activation energies of the proton conductivity are between 0.42-0.47 eV and 0.68-0.82 eV in the bulk and grain boundary, respectively.

The dense and uniform BYZ thin films of 140-200 nm in thickness were obtained by co-sputtering (M1) and 2-step sputtering (M2) techniques. The XRD patterns of M1-BYZ thin films show that the concentration of Y is increased with the increasing DC power of the Y target. Y_2O_3 phase segregation is observed in the M1-BYZ files, while the YSZ phase segregation appears in the M2-BYZ thin films. The conductivities of the BYZ thin films are about 100 times than those of the pellet samples. This high conductivity may be caused by microstructure, grain size, impedance measurement, impurities, and ionic conduction mechanism.

Department :Materials Science..... Student's Signature :

Field of Study :Ceramic Technology... Advisor's Signature :

Academic Year :2009..... Co-Advisor's Signature :

ACKNOWLEDGEMENTS

The fulfillment of this thesis would be impossible without assistance from so many people. Among them, I am especially grateful to my advisor and co-advisor, Dr. Rojana Pornprasertsuk and Dr. Sujarinee Kochawattana who introduced me to the field of fuel cell, guided me through out the entire work, and encouraged me to a higher level of success.

I warmly thank Asst.Prof.Dr. Sirithan Jiemsirilers, Asst.Prof.Dr. Thanakorn Wasanapiarnpong and Dr. Pongpan Chindaudom for taking time to serve on my committee, whom made valuable contributions and productions to my thesis

Part of the work was performed with the assistance and the equipment of other groups. My sincerely thanks go to Mr.Adisak Thueploy for the help with cold isostatic pressing (MMRI, Chulalongkorn University), Dr. Pongpan Chindaudom, Dr. Mati Horphatum and Ms. Puenisara Limnonthakul for the BYZ thin film fabrication (NECTEC), Dr. Sumittra Charojrochkul and Dr. Pimpa Limthongkul for the EIS equipment and the insightful discussion on the proton conductivity measurement (MTEC).

Many thanks go to all teachers and my dear friends here at Chulalongkorn University for giving assistance and valuable friendship. And of course, thank to Mr. Kittichai Somroop for EIS measurement, Mr. Nopporn Rujisamphan and Ms. Nawarat Ekkarntong for the knowledge of \LaTeX and constant encouragement.

Finally, I am eternally grateful to my beloved family for their forever support, love and encouragement throughout my life.

This research was supported by National Center of Excellent for Petroleum, Petrochemicals and Advance Materials, Chulalongkorn University and the Development and Promotion of Science and Technology Talents Project (DPST).

CONTENTS

	Page
ABSTRACT IN THAI	iv
ABSTRACT IN ENGLISH	v
ACKNOWLEDGEMENTS	vi
CONTENTS	vii
LIST OF TABLES	xi
LIST OF FIGURES	xii
CHAPTER	
I INTRODUCTION	1
1.1 Introduction	1
1.2 Motivation for Direct Ethanol Fuel Cell	2
1.3 Motivation for Proton Conducting Oxide	2
1.4 Research Objectives	4
1.5 Thesis Organization	5
II LITERATURE REVIEWS	6
2.1 State-of-Art of Fuel Cell	6
2.1.1 What is a fuel cell ?	6
2.1.2 Direct ethanol fuel cell	8
2.1.3 Fuel cell performance	11
2.2 Proton Conducting Solid Electrolyte	13

2.2.1	BaZrO ₃ structure	13
2.2.2	Protonic defect formation in Y-doped BaZrO ₃	14
2.2.3	Proton conductivity of Y-doped BaZrO ₃	15
2.2.4	Sintering property of Y-doped BaZrO ₃	17
2.3	Background on The Sputtering Techniques	19
2.3.1	Direct current (DC) sputtering	20
2.3.2	Radio frequency (RF) sputtering	21
2.3.3	Magnetron sputtering	21
2.4	Parameters in The Sputtering Technique	22
2.4.1	Substrate materials	22
2.4.2	Partial pressure of Ar	23
2.4.3	Substrate Temperature	23

III EXPERIMENTAL METHODS AND CHARACTERIZATION

TECHNIQUES	24
3.1 Pellet Samples Preparation	24
3.2 Thin Film Fabrication	27
3.2.1 Sputter deposition	27
3.2.2 BYZ sputtering methods	29
3.3 Characterization Techniques	33
3.3.1 Particle size by Light scattering method	33
3.3.2 Density by Archimedes method	33
3.3.3 Microstructures by Scanning electron microscopy (SEM)	34
3.3.4 Microstructure by Field emission scanning electron microscopy (FE-SEM)	35
3.3.5 Crystallography by X-Ray diffraction	36
3.3.6 Proton conductivity by electrochemical impedance spectroscopy	38

IV RESULTS AND DISCUSSION: BaZr_{1-x}Y_xO_{3-δ} PELLETS	44
4.1 Particle Size of Raw Materials	44
4.2 XRD Patterns of BYZ Pellet Samples	46
4.3 Microstructure of BYZ Pellet Samples	49
4.3.1 Densification	49
4.3.2 Microstructure	50
4.4 Proton Conductivity of BYZ Pellet Samples	53
4.4.1 Impedance spectra analysis	53
4.4.2 Temperature dependence on the proton conduction mechanisms of BYZ pellets	54
4.4.3 The Y content dependence on the proton conductivities of BYZ pellets	55
4.4.4 The proton conductivities measured in different atmospheres	59
4.4.5 Dependence of BaO loss on the proton conductivities	61
4.4.6 Comparison of the proton conductivity with the results from the previously reported literatures	63
V RESULTS AND DISCUSSIONS: THIN FILMS	65
5.1 XRD Patterns of BYZ Thin Films	65
5.1.1 BaZrO ₃ thin films	65
5.1.2 Y-doped BaZrO ₃ (BYZ) thin films	66
5.2 Microstructure of BYZ Thin Films	69
5.3 Uniformity and Depth profiling of M1-BYZ Thin Films	71
5.4 Proton Conductivity of BYZ Thin Films	73
5.4.1 The EIS result of M1-BYZ thin films in air	73
5.4.2 The EIS result of M2-BYZ thin films in air	74
5.4.3 Proton conductivities of M2-BYZ thin films in H ₂	75

5.5 Comparison of the BYZ thin film conductivities to those of the BYZ pellets and the result from the previously reported literatures	77
VI CONCLUSIONS and FUTURE WORKS	80
6.1 Conclusions	80
6.2 Future Works	82
REFERENCES	83
APPENDICES	87
Appendix A: Particle Size Distribution (PSD)	88
Appendix B: Densities of BYZ Pellet Sample	91
Appendix C: JCPDS	92
VITAE	95

ศูนย์วิทยทรัพยากร
จุฬาลงกรณ์มหาวิทยาลัย

LIST OF TABLES

2.1	The melting points and thermal expansion coefficients of some substrate materials [27, 28].	22
3.1	Mass loss after calcination at different dopant concentrations . . .	25
3.2	Deposition parameters of BaZrO ₃ thin film	30
3.3	Deposition parameters of Y-doped BaZrO ₃ (BYZ) thin film . . .	30
3.4	Deposition parameters of Yttrium film on the BaZrO ₃ target . . .	32
3.5	Deposition parameters of BYZ thin films fabricated by the M2 method	32
4.1	Particle size of raw materials	45
4.2	Particle size of calcined powders	45
4.3	Bulk, grain boundary and total activation energies of nano-Y ₂ O ₃ -BYZ pellets	58
B.1	Relative density of green and sintered bodies of micro-Y ₂ O ₃ -BYZ	91
B.2	Relative density of green and sintered bodies of nano-Y ₂ O ₃ -BYZ	91

LIST OF FIGURES

1.1	The calculation of proton conductivity in various oxides.[6]	3
2.1	Comparison between operational mechanism of SOFC and PEMFC	7
2.2	Illustration of direct ethanol fuel cell (DEFC)	9
2.3	Schematic of fuel cell I-V curve.[10]	11
2.4	A unit cell of BaZrO ₃ : the perovskite structure.	13
2.5	Illustration on migration of proton in perovskite oxide.[17]	14
2.6	Phase diagram of BaZrO ₃ [20].	17
2.7	Schematic representation of the sputtering deposition system [25].	19
2.8	Schematic of the DC sputtering system [26].	20
2.9	Schematic of the RF sputtering system [26].	21
3.1	Experimental procedure of pellet sample preparation	26
3.2	Schematic of AJA the sputtering system	27
3.3	Top and side views of AJA sputtering system	28
3.4	Schematic of the M2 fabrication procedure and the modified Y- BaZrO ₃ target	31
3.5	Schematic of XRD measurement	36
3.6	Schematic of (a) Nyquist plot (b) Bode plot [35].	39
3.7	Idealized Nyquist plot of ceramic oxides and its equivalent circuit[35].	40
3.8	Factors for the proton conductivity calculation (a)pellets (b)thin films.	41
3.9	Schematic diagram of the AC-Impedance measurement	43
4.1	XRD patterns of the sintered BYZ pellet samples with x= 0.06-0.4 (a) micro-Y ₂ O ₃ -BYZ and (b) nano-Y ₂ O ₃ -BYZ	46

4.2	The lattice parameter of BYZ pellets after sintering at 1400°C . . .	47
4.3	The lattice parameters of $\text{BaZr}_{1-x}\text{Y}_x\text{O}_{3-\delta}$ at $0.06 \leq x \leq 0.4$ obtained from this study compared to the values from the previously reported literatures; applied from Kreuer[15] and Iguchi[18]. . . .	48
4.4	Relative density of green and sintered bodies of (a) micro- Y_2O_3 -BYZ and (b) nano- Y_2O_3 -BYZ	49
4.5	SEM images of (a) green body (b) sintered body (c) cross-section and (d) polished Nano- Y_2O_3 - $\text{BaZr}_{0.8}\text{Y}_{0.2}\text{O}_{3-\delta}$ pellet samples . . .	50
4.6	SEM images of micro- Y_2O_3 -BYZ and nano- Y_2O_3 -BYZ sintered bodies with 6-40 at.% Y contents	52
4.7	The impedance spectra of BYZ pellet sample in the different frequency.	53
4.8	The bulk, grain boundary and total conductivities of $\text{BaZr}_{0.8}\text{Y}_{0.2}\text{O}_{3-\delta}$ in air	54
4.9	Bulk conductivities of BYZ pellet samples in air	56
4.10	Grain boundary conductivities of BYZ pellet samples in air . . .	56
4.11	Total conductivities of BYZ pellet samples in air	57
4.12	Bulk, grain boundary and total conductivities of BYZ pellet samples with different Y contents at 350°C in air	57
4.13	Total conductivities of BYZ pellet samples (a) 6 at.% (b) 10 at.% (c) 20 at.% (d) 30 at.% and (e) 40 at.% in different atmospheres	60
4.14	Total conductivities of BYZ pellet samples (a) 6 at.% (b) 10 at.% (c) 20 at.% (d) 30 at.% and (e) 40 at.% sintered in different atmospheres.	62

4.15	The comparison of our proton conductivities (a) bulk conductivity (b) grain boundary conductivity of $\text{BaZr}_{0.8}\text{Y}_{0.2}\text{O}_{3-\delta}$ to the previously reported literatures[15, 22, 23, 38]	64
5.1	XRD patterns of BaZrO_3 films at the substrate temperatures of room temperature to 500°C	66
5.2	XRD patterns of Y-doped BaZrO_3 (BYZ) thin films (a) Deposited by the co-sputtering technique at DC powers of 3-15W. (b) Deposited by the 2-step sputtering technique at different Y-window angles of $20\text{-}40^\circ$	67
5.3	The lattice parameters of BYZ thin films deposited by co-sputtering (M1) and 2-step sputtering (M2) compared to those of pellets. . .	68
5.4	SEM images of (a) surface (b) the cross-sectional BYZ thin films fabricated by co-sputtering technique (M1)	69
5.5	SEM images of BYZ thin films fabricated by the 2-step sputtering technique (M2) after annealing at 800°C : (a) surface (b) cross-section at an Y-window angle of 20° (c) cross-section at an Y-window angle of 30° (d)cross-section at an Y-window angle of 40°	70
5.6	The XPS depth profile of M1-BYZ thin film with DC power 20 Watt	71
5.7	The plot of the intensity with respect to the binding energy of M1-BYZ thin films with different DC sputtering power on the Y target (a) Y3d:3W (b) Zr3p ³ :3W (C) Y3d:10W and (d) Zr3p ³ :10W	72
5.8	Conductivities of M1-BYZ thin films in air	73
5.9	Conductivities of M2-BYZ thin films in air	74
5.10	Conductivities of M2-BYZ thin film with 20 open angle in wet H_2	76
5.11	Total conductivities of M2-BYZ thin film in air and wet H_2 . . .	76

5.12	The impedance spectra of (a) pellet (b) thin film	77
5.13	Conductivities of BYZ thin film compared to those of BYZ pellets	78
5.14	The comparison of the proton conductivities of M1-BYZ and M2-BYZ thin films to the results from the previously reported literatures and BYZ pellets from this study.	79
A.1	The particle sizes distribution of raw materials (a) BaCO ₃ (b) 3 mol% Yttria Stabilized Zirconia (c) micro-Y ₂ O ₃ (d) nano-Y ₂ O ₃ powders	88
A.2	The particle size distribution of micro-Y ₂ O ₃ -BYZ (a) 6 at.% (b) 10 at.% (c) 20 at.% (d) 30 at.% (e) 40 at.%	89
A.3	The particle size distribution of nano-Y ₂ O ₃ -BYZ (a) 6 at.% (b) 10 at.% (c) 20 at.% (d) 30 at.% (e) 40 at.%	90
C.1	The JCPDS of Barium Zirconate	92
C.2	The JCPDS of Yttrium Oxide	93
C.3	The JCPDS of Yttrium Zirconium Oxide	94

CHAPTER I

INTRODUCTION

1.1 Introduction

At present, the increasing of energy demand all over the world is significantly attributed to the diminishing of fossil fuel reserves such as oil, coal and natural gas. Experts forecast that oil reserves will exhausted in approximately 30 or 40 years, while the demand of energy has been continually increasing. Alternative energy sources, such as solar, wind, hydrogen and biomass, may be one of the best approaches to decline the world energy crisis. Among them, hydrogen and biomass have gained attention as a clean and efficient source of power.

A fuel cell is an energy conversion device that converts the chemical reaction of an alternative energy source mentioned above and an oxidant into the electrical energy, which has an electrochemical mechanism similar to a battery. However, the main difference between fuel cell and battery is the fuel supply management. Fuel cells consume externally supplied fuels and continuous electricity as long as the fuels are supplied, whereas batteries use internal fuels and must be disposed after its chemicals are used up [1]. A number of progresses have been done on the development of fuel cell technology during the last several decades. However, the complicated system and high cost are the major constraint of this technology (for examples, fuel cells require proper materials for electrolytes and electrodes; as well as expensive metal catalysts). Therefore, there are still a lot of improvement needed to make fuel cell technology become reality.

1.2 Motivation for Direct Ethanol Fuel Cell

Pure hydrogen gas (H_2) is a typical fuel used in fuel cells; however, it is not a natural fuel. The production, storage and transportation of the hydrogen gas are still under development. As a result, all of these problems stimulate researchers to feed liquid fuel directly to fuel cells instead. One of the potential fuels, which has been investigated, is methanol due to its high electrochemical activity compared to other liquid fuels. Nevertheless, methanol (CH_3OH) is not only harmful for human but also exhibits carbon monoxide as a by-product into the atmosphere. Almost all the methanol made today is produced from methane by the Syngas method, which is converted to carbon monoxide and hydrogen and then formed into methanol.

Ethanol (C_2H_5OH) is another promising alternative fuel due to its non-toxicity, natural availability, high power density and feasibility in storage and transportation. As a result, direct ethanol fuel cells (DEFC) have become an alternative energy converter to convert ethanol and oxygen into the electricity. Performance of DEFCs have been explored extensively; however, the main challenges of DEFC on the kinetic and ethanol cross over are still under consideration [2, 3].

1.3 Motivation for Proton Conducting Oxide

Acceptor-doped perovskite types $AB_{1-x}M_xO_{3-\delta}$ with $A = Ca, Sr, Ba$; $M = Ce, Zr$; $M = Y, Sc, Ln$, etc. exhibit a proton conduction ability over an intermediate temperature range of 250-600°C. Among these oxides, researchers found that materials based on $SrCeO_3$ [4] and $BaCeO_3$ [5] show a high proton conductivity. However, these materials are unstable at high temperatures which in turn could cause a severe problem for fuel cell applications. Therefore, the proton conductor

based on Y-doped BaZrO₃ (BYZ) is chosen for this study due to its high bulk proton conductivity compared with other oxides and high chemical stability in the fuel cell environment. The comparison of proton conductivities of perovskite oxides calculated from their proton concentrations and mobilities is shown in Fig 1.1.

According to the calculation in Fig 1.1, Y-doped BaZrO₃ (BYZ) shows slightly higher proton conductivity than that of BaCeO₃. The chemical stability of BYZ is also higher than BaCeO₃ because of the higher electronegativity of Zr than Ce and the stronger of the Zr-O covalent bonds [6].

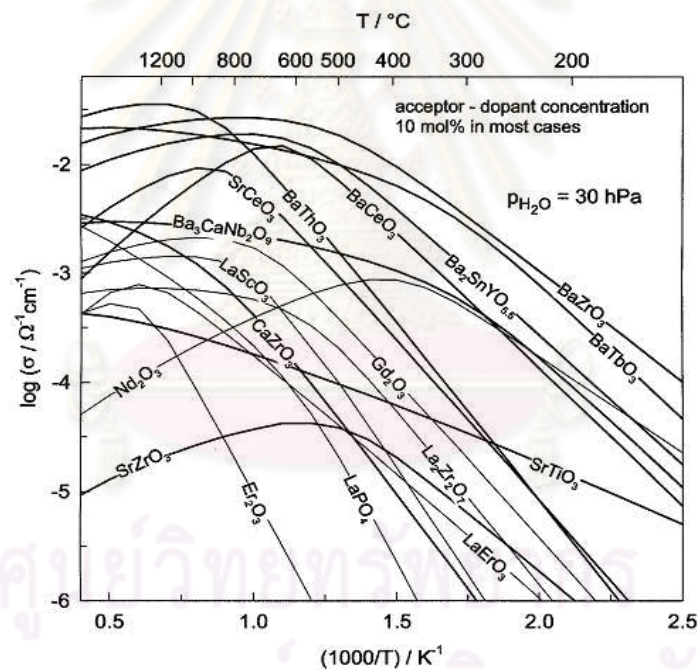


Figure 1.1: The calculation of proton conductivity in various oxides.[6]

1.4 Research Objectives

The main objectives of this study are to fabricate and measure the proton conductivities of BYZ pellets and thin films electrolytes at different doping concentrations for intermediate temperature DEFC electrolytes. The correlation between dopant concentration, microstructure and proton conductivity are subsequently studied. The scope of this study is divided into three objectives as followed:

1. To prepare $\text{BaZr}_{1-x}\text{Y}_x\text{O}_{3-\delta}$ pellet samples with $x = 0.06, 0.1, 0.2, 0.3$ and 0.4 by solid state reaction method. The influence of Y_2O_3 particle size and Y content to the physical properties of BYZ pellets are subsequently analyzed.

2. To fabricate BYZ thin films by two sputtering methods: (i) co-sputtering, (ii) 2-step of sputtering. The influence of the fabrication processes on the physical properties are inspected.

The physical properties investigated are comprised of the particle size (Light scattering technique), phase (X-ray diffraction), density (Archimedes method) and microstructure (Scanning electron microscopy and Field emission scanning electron microscopy).

3. To determine proton conductivities of BYZ pellets and thin films by the electrochemical impedance spectroscopy (EIS) technique. The effect of sintering and fabrication process are investigated on the proton conductivities of BYZ pellets and thin films, respectively. In this study, the proton conductivity is measured at a temperature range of $250\text{-}600^\circ\text{C}$ in various atmospheres (air, dry H_2 :7% H_2 in Ar and wet H_2 : 7% H_2 in Ar).

1.5 Thesis Organization

This work entitled Proton Conductivity on Y-doped BaZrO₃ for Intermediate Temperature Direct Ethanol Fuel Cell is divided into 6 chapters.

Chapter 1 is the introduction and motivations.

Chapter 2 provides backgrounds and literature reviews which are necessary for this study. The overviews of fuel cells, proton conducting electrolytes, thin film deposition processes etc. are elaborated and summarized.

The pellets and thin films fabrication processes are illustrated, and the characterization methods and instruments for both pellet and thin film samples are also introduced in Chapter 3.

Chapter 4 presents the effect of Y doping concentrations, sintering processes and EIS measurement conditions on the proton conductivities of BYZ pellets. The proton conductivities are subsequently compared to the results from previous reported literatures.

Chapter 5 presents the physical properties of BYZ thin films deposited by the co-sputtering and 2-step sputtering techniques. The proton conductivities of the BYZ thin films are then discussed and compared to the results of BYZ pellets in Chapter 4.

Finally, Chapter 6 includes the conclusion of these studies and the suggestions for future works.

CHAPTER II

LITERATURE REVIEWS

This chapter includes the backgrounds and literature reviews of the proton conducting oxide electrolyte studies. An overview of fuel cells and proton conducting electrolytes, Y-doped BaZrO₃ (BYZ), are then elaborated. Finally, the thin film deposition processes and the deposition parameters which affect the thin film properties are introduced.

2.1 State-of-Art of Fuel Cell

2.1.1 What is a fuel cell ?

A fuel cell is an energy conversion device which converts the chemical energy of fuels and oxidants directly into the electrical energy. The main difference between a fuel cell and battery is that a fuel cell will continue to produce electricity as long as the fuel is supplied, while the battery use internal fuels and must be disposed after its chemicals are used up.

A fuel cell consists of three main components: the cathode, anode and electrolyte. The basic physical structure of fuel cell consists of an electrolyte layer in contact with a porous anode and cathode on each side. Fuels and oxidants are supplied to the anode and cathode, respectively. The conducting ions produced from the fuels/oxidant from one electrode migrate across the electrolyte to react with the oxidant/fuel on the other electrode. Electricity is then obtained as a product of redox reactions.

Five major types of fuel cells have been categorized. [7].

- (1) Alkaline fuel cell (AFC)
- (2) Molten carbonate fuel cell (MCFC)
- (3) Phosphoric acid fuel cell (PAFC)
- (4) Proton exchange membrane fuel cell (PEMFC)
- (5) Solid oxide fuel cell (SOFC)

The state-of-art of fuel cells is dominated by two main technologies as illustrated in Fig 2.1 : (i) solid oxide fuel cells (SOFCs) and (ii) proton exchange membrane fuel cells (PEMFCs).

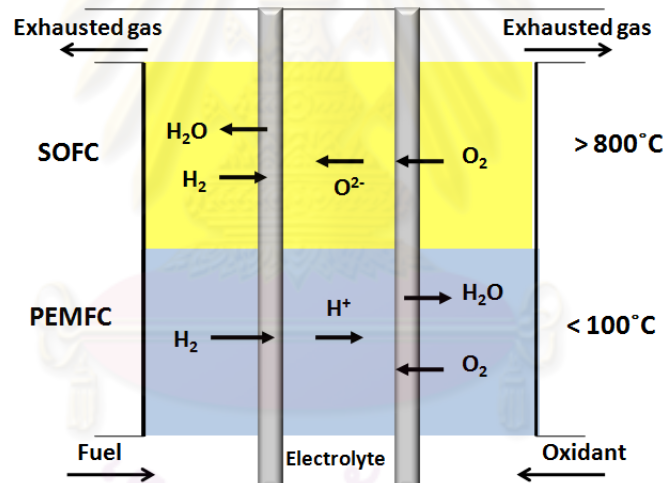
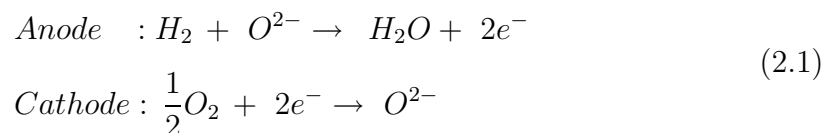
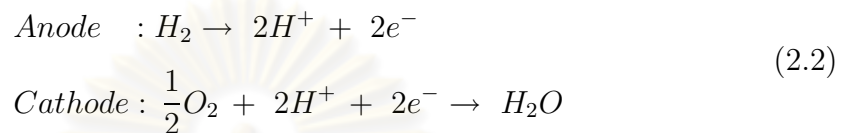


Figure 2.1: Comparison between operational mechanism of SOFC and PEMFC

◇ An SOFC is one type of fuel cell which operates at high temperatures ($> 800^{\circ}\text{C}$) and has oxygen ions (O^{2-}) as ionic charge carriers. The half reactions at the electrodes are shown below (Eq. 2.1):



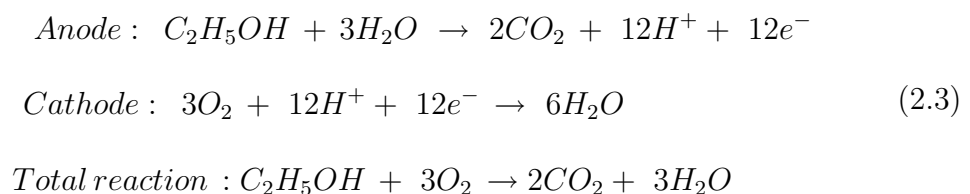
◇ An PEMFC is another type of fuel cells which operates at low temperatures (25-100°C) and uses a polymeric membrane (Nafion®) as an electrolyte. The electrolyte enables protons to transport to the other side of electrode. The half reactions in a H₂-O₂ PEMFC are given below (Eq. 2.2):



2.1.2 Direct ethanol fuel cell

Direct ethanol fuel cell (DEFC) (Fig 2.2) is another fuel cell technology, which works similarly to the PEMFC but use ethanol as a fuel instead of hydrogen. Ethanol, a liquid fuel, is an attractive alternative fuel because of the following reasons: (i) non-toxicity (ii) natural availability (iii) the feasibility in the production, storage and transportations and (iv) high power density.

Ethanol is fed directly through the anode. Protons (H⁺) which are created from the oxidation process of ethanol molecules on the anode, migrate across the electrolyte to react with oxygen molecules on the cathode. The free electrons transport from the anode to the cathode through an external circuit. The electrochemical reactions in the DEFCs are given below (Eq. 2.3):



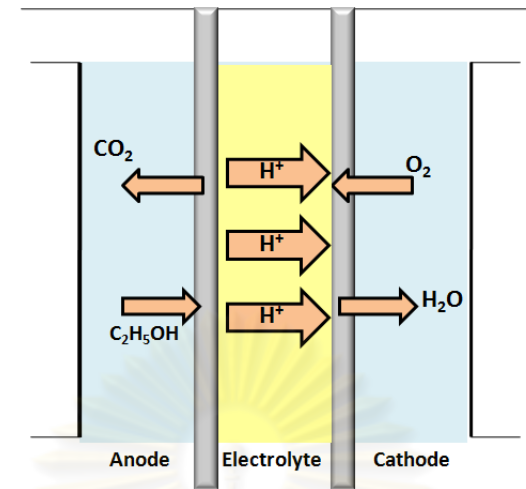


Figure 2.2: Illustration of direct ethanol fuel cell (DEFC)

This study mainly focuses on the fabrication and properties of electrolytes for the intermediate temperature DEFC. To achieve high performance and efficiency, the electrolytes must meet the following requirements [7]:

- ◇ High protonic conductivity
- ◇ Low electronic conductivity
- ◇ High stability (in both oxidizing and reducing environments)
- ◇ Low fuel cross over
- ◇ Reasonable mechanical strength

Nafion[®] membranes are commonly used as electrolytes in the DEFCs due to their high H^+ conductivity even at low temperatures. However, their proton conductivity is primarily dependent on the water content in the membrane. Thus, the working temperature of the DEFCs is usually less than $100^{\circ}C$. However, since Nafion[®] gives drawbacks on the water flooding and ethanol crossover problems, several attempts have been made to solve these problems and improve its performance.

In 2005, Mathuraiveeran et al. [8] pointed out the possibility of using the composite membranes based on sulphonated poly(etheretherketone) (sPEEK) as DEFC electrolyte instead of Nafion[®]. The sPEEK membranes were prepared by a normal casting and solvent evaporation process with different silane modifier: I-imidazole, P-phosphato, A-amino and G-glycidly. The results were revealed that the membrane modified with phosphatosilane showed the least ethanol crossover. On the other hand, the membrane which was modified with imidazole-silanes showed the highest proton conductivity. Moreover, they found out that the sPEEK membrane incorporated with HAp have the ethanol permeability lower than Nafion[®] 117.

Song et al. [9] compared the fuel cell performances by feeding ethanol into two fuel cell systems: SOFC and PEMFC. They found that the direct ethanol SOFC (800°C) exhibited ten times higher performance than PEMFC (90°C). Furthermore, the performance of PEMFCs with different types of fuel: ethanol, methanol and hydrogen were compared. The results showed that the single DEFC had the worst performance among all fuel cell types which resulted from the slower kinetic of ethanol oxidation compared to those of hydrogen and methanol.

The further study by Song et al. in 2007 [3] showed the conversion rate of the ethanol oxidation by thermodynamic calculations. They reported that when the temperature is less than 100°C, the maximum possible conversion for the reaction conversion of ethanol to CO₂ and H₂O in DEFC was less than 14%. As a consequence, the DEFC efficiency was inevitably decreased. Moreover, the low operating temperature gave some disadvantages on the low fuel conversion, slow electrode kinetic, CO poisoning of the electrocatalyst, which in turn cause the demand for high catalyst loading. Therefore, they suggested that DEFC should be operated at $T > 150^\circ\text{C}$, at which the complete oxidation conversion was observed.

2.1.3 Fuel cell performance

The performance of a fuel cell can be analyzed from the current-voltage (I-V) curve, which shows the voltage output of the fuel cell at a given current. An ideal fuel cell can always maintain at a reversible voltage no matter how much current is extracted. However, because of several irreversible losses, a typical fuel cell cannot maintain its reversible voltage during its operation. There are three main types of fuel cell losses [7].

- ◇ Activation losses—(due to the electrochemical reactions on the electrodes)
- ◇ Ohmic loss—(due to ion movement across the electrolyte and electronic carrier movement at the electrodes)
- ◇ Concentration loss—(due to the supply of reactant and the removal of products of the fuel cell)

The typical I-V curve of the fuel cell is shown in Fig 2.3. The actual voltage output of the fuel cell at a given current output can be calculated as given in Eq.2.4 [7] .

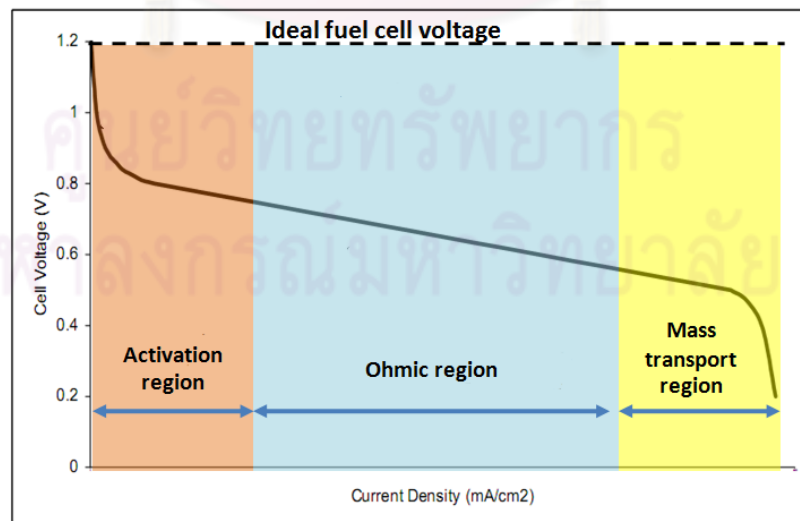


Figure 2.3: Schematic of fuel cell I-V curve.[10]

$$V = E_{thermo} - \eta_{act} - \eta_{ohmic} - \eta_{conc} \quad (2.4)$$

where V = actual output voltage of fuel cell

E_{thermo} = thermodynamically predicted fuel cell voltage output

η_{act} = activation losses due to reaction kinetics

η_{ohmic} = ohmic losses from ionic and electronic conduction

η_{conc} = concentration losses due to mass transport of reactants
and products



ศูนย์วิทยทรัพยากร
จุฬาลงกรณ์มหาวิทยาลัย

2.2 Proton Conducting Solid Electrolyte

Among the proton conductors, acceptor-doped BaZrO_3 have drawn much attention since its high proton conductivity was first reported by H.Iwahara et.al [11]. Yttrium-doped BaZrO_3 (BYZ) is one of the promising proton conductor for fuel cell application because of its high bulk proton conductivity and high chemical stability in CO_2 atmosphere [12].

2.2.1 BaZrO_3 structure

Barium zirconate (BaZrO_3) has a perovskite crystal structure of ABO_3 chemical formula. The Ba^{2+} and O^{2-} form an FCC lattice while Zr^{4+} occupies the octahedral interstitial sites in the FCC unit cell. At temperature above 120°C , the crystal structure is cubic with a lattice parameter of 4.193 \AA [13]. A unit cell of BaZrO_3 structure is shown in Fig 2.4.

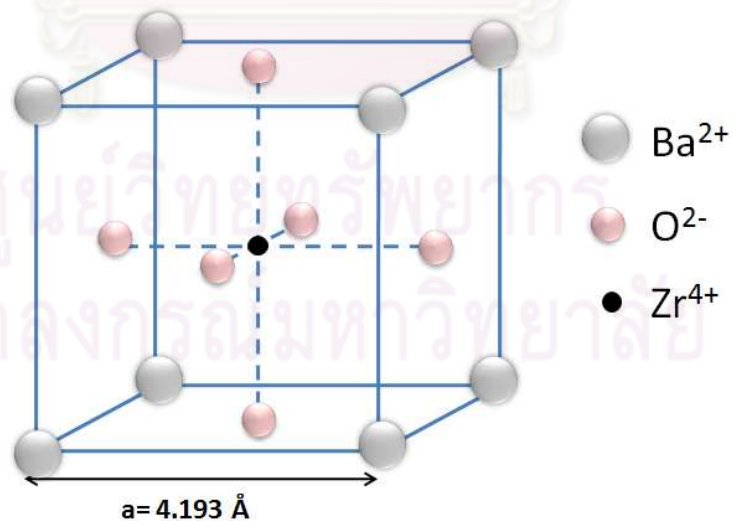
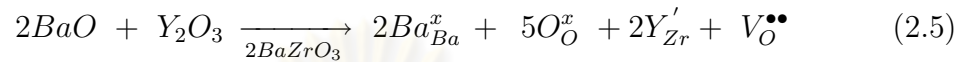


Figure 2.4: A unit cell of BaZrO_3 : the perovskite structure.

2.2.2 Protonic defect formation in Y-doped BaZrO₃

The defect reaction in Eq.2.5, as Y is doped into BaZrO₃, yttrium atoms will substitute in the Zr sites which cause the formation of oxygen vacancies [14].



Y-doped BaZrO₃ first attains the protons from water vapor [15, 16]. When a water molecule dissociates into a hydroxide ion (OH⁻) and proton (H⁺) (Eq. 2.6). The oxygen atom in an hydroxide ion fills an oxygen vacancy in the BYZ structure. while the proton forms a covalent bond with the nearby oxygen lattices. H⁺ atom can then hops to the next oxygen ion throughout the BYZ structure (Fig 2.5).

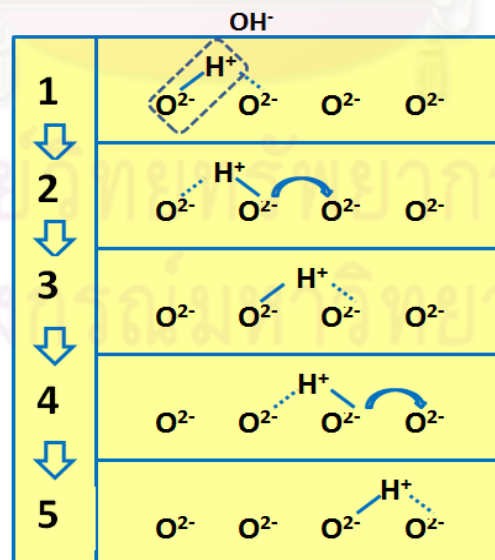
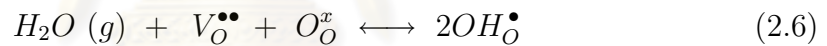


Figure 2.5: Illustration on migration of proton in perovskite oxide.[17]

2.2.3 Proton conductivity of Y-doped BaZrO₃

A number of researchers have studied the proton conductivity of yttrium-doped BaZrO₃ (BYZ). The proton conductivity data of BaZr_{1-x}Y_xO_{3-δ} has been reported on various synthesis methods and measurement conditions.

In 1993, Iwahara et al. [17] studied the proton conductivity of sintered oxides based on calcium, strontium and barium zirconate doped by Ga, In, Nd, Y or Dy. The proton conductivity was measured in the hydrogen atmosphere. The results revealed that the BaZrO₃-based ceramics showed higher conductivity than calcium and strontium based-oxides. Moreover, the doped specimens BaZr_{0.95}Y_{0.05}O_{3-δ} (M=Ga, In, Y, Nd, Dy) showed higher conductivities than that of pure BaZrO₃.

In 2001, Kreuer et al. [15] studied the mobility and stability of protonic defect in acceptor-doped perovskite type oxides (ABO₃) (i.e. SrTiO₃, SrZrO₃, BaZrO₃ and BaTiO₃ systems). They found that the the formation and mobility of protonic defects were sensitive to the type of acceptor dopants. The highest proton conductivity was observed in Y-doped BaZrO₃ in spite of its significantly bigger ionic radius of Y³⁺ compared to Zr⁴⁺. At 250-700°C, the observed proton conductivities were in range $1.9 \times 10^{-3} \text{ Scm}^{-1}$ - $3.2 \times 10^{-2} \text{ Scm}^{-1}$, which clearly exceeded the oxide ion conductivities.

In 2004, Snijkers et al. [14] investigated the proton conductivity of sintered BaZr_{0.9}Y_{0.1}O_{3-δ} samples by electrochemical impedance spectroscopy. The samples were prepared by solid state reaction method with varying Ba-content (stoichiometry and excess BaCO₃). The group tested the conductivity in the temperature range of 25-900°C with 50% relative humidity. They found that conductivity of samples produced with excess BaCO₃ was increased by 1 order magnitude with respect to that of stoichiometric samples. At 25-300°C, the conductivity was dominated by proton conduction. Proton conductivity obtained in their study

was varied from $1.5 \times 10^{-7} \text{ Scm}^{-1}$ at 100°C to $1 \times 10^{-3} \text{ Scm}^{-1}$ at 500°C .

In 2007, Iguchi et al. [18] fabricated Y-doped BaZrO_3 samples with the doping concentrations ranging from 5 mol% to 15 mol% at various annealing temperatures. The correlations between the doping concentration of Y-doped BaZrO_3 , microstructure and grain boundary conductivity were subsequently investigated. The results showed that by increasing the Y concentration to 15 mol%, the average grain diameter was increased by four times, and the grain boundary conductivity was increased by three orders of magnitude. The total conductivities of the samples were varied from $1 \times 10^{-6} \text{ Scm}^{-1}$ at 350°C to $4 \times 10^{-4} \text{ Scm}^{-1}$ at 550°C .

In 2008, Cervara et al. [19] studied the effect of morphological and structural changes upon annealing on the proton conductivity of 20 mol% Y-doped BaZrO_3 nanograined samples. The proton conductivity of the sample annealed at 800°C with 10 nm grain size was about $8.7 \times 10^{-6} \text{ Scm}^{-1}$. The higher conductivity was observed with increasing annealing temperatures due to the higher grain boundary contact and better yttrium distribution from the grain interior to grain boundary. The total proton conductivity at 500°C of the sample annealed at 1250°C and 1500°C were 2×10^{-3} and $4 \times 10^{-3} \text{ Scm}^{-1}$ with grain sizes of about 50 nm and 200 nm, respectively.

2.2.4 Sintering property of Y-doped BaZrO₃

A dense Y-doped BaZrO₃ (BYZ) sample is usually achieved after sintering at temperatures higher than 1700°C [20]. The high sintering temperature of BYZ is primarily caused by the high melting point of BaZrO₃ (Fig 2.6). Several attempts have been done to lower the BYZ sintering temperature.

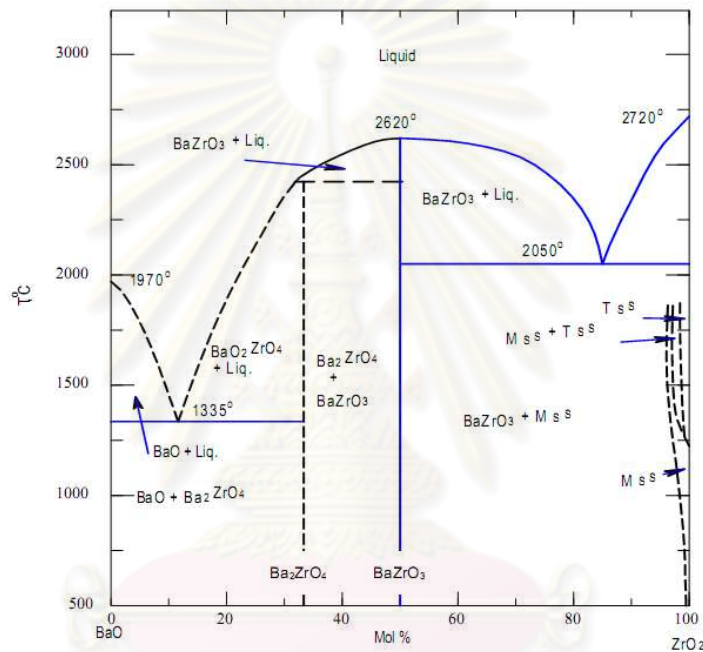


Figure 2.6: Phase diagram of BaZrO₃ [20].

As observed by Babilo et al. [21], the high sintering temperature can reduce the proton conductivity due to the loss of Ba from the BaO evaporation. Therefore, to improve the performance of BYZ, the sintering temperature should be lowered. Several researches have found that adding ZnO as a sintering aid could effectively enhance the sintering property of BaZrO₃ and lower the sintering temperature down to less than 1400°C.

Babilo and Haile investigated the influence of transition metal oxide as an additive on the densification and electrical properties of Y-doped BaZrO₃. They

found that 4 mol% NiO, CuO and ZnO effectively enhanced the densification of $\text{BaZr}_{0.85}\text{Y}_{0.15}\text{O}_{3-\delta}$ sintered at 1300°C , rising from 60% to $\sim 86\text{-}93\%$. In contrast, other additives such as V, Cr and Fe were substantially worsened the densification behavior.

Another attempt to lower the sintering temperature of $\text{BaZr}_{0.8}\text{Y}_{0.2}\text{O}_{2.9}$ was reported by Tao et al. [22]. By adding 0.02-0.12 wt% of ZnO, the sintering temperature can be reduced to 1325°C , and $\sim 95\%$ relative density was achieved. The proton conductivities were subsequently measured in various atmospheres (air, dry H_2 and wet H_2 /Ar). The results showed that the conductivities of the samples with 1 wt% ZnO addition were higher than those without ZnO. Furthermore, the conductivities of samples measured in wet 5% H_2 were higher than those measured in dry 5% H_2 , which in turn confirmed the proton conduction in $\text{BaZr}_{0.8}\text{Y}_{0.2}\text{O}_{2.9}$.

In 2009, Peng et al.[23] studied the sintering temperature of $\text{BaZr}_{0.85}\text{Y}_{0.15}\text{O}_{3-\delta}$ with the addition of 1 wt% ZnO. The samples were sintered in air at temperatures in a range of $1350\text{-}1500^\circ\text{C}$. They observed that the grain size increased from $1\ \mu\text{m}$ to $4\ \mu\text{m}$ with increasing sintering temperature from 1350°C to 1500°C , respectively. Moreover, $\text{BaZr}_{0.85}\text{Y}_{0.15}\text{O}_{3-\delta}$ sintered at 1500°C and 1650°C showed the similar activation energy of the bulk proton conductivity, and the sample sintered at 1650° exhibited the bulk proton conductivity in the order of $10^{-2}\ \text{Scm}^{-1}$.

2.3 Background on The Sputtering Techniques

The sputtering technique has many advantages in terms of the uniformity, low deposition temperature and low contamination. In this study, Y-doped BaZrO₃ (BYZ) thin films are deposited by: (i) co-sputtering and (ii) 2-step sputtering methods. The properties of thin film mostly depend on the processing parameters such as power, pressure, substrate temperature etc; therefore, the principle of the sputtering technique and the variable parameters must be understood.

The basic mechanism of the sputtering technique is given in Fig 2.7. A target and substrate are placed on the anode and the cathode, respectively. The process begins by bombarding the surface of the target by a noble gas (commonly Ar) passing through the anode and cathode under high electromagnetic field. The magnetic field induces ionization and plasma of positive ions and electrons. The positive ions are then accelerated and bombarded the target. The atoms ejected from the target are accelerated and subsequently deposited on the substrate [24].

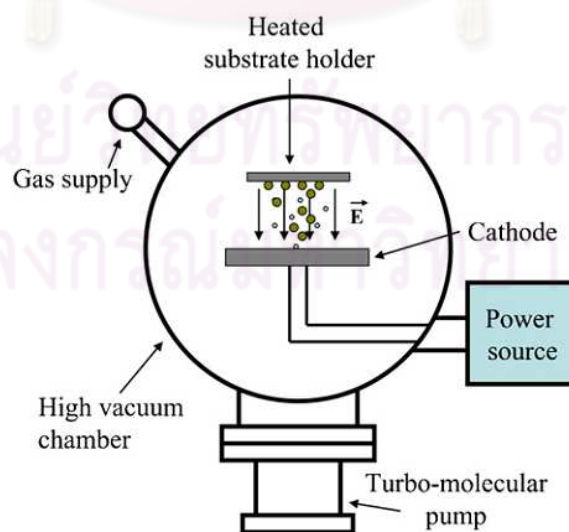


Figure 2.7: Schematic representation of the sputtering deposition system [25].

There are four major types of the basic sputtering systems: (i) DC sputtering, (ii) RF sputtering, (iii) Magnetron sputtering and (iv) Reactive sputtering. This Chapter includes the background of the first three methods.

2.3.1 Direct current (DC) sputtering

The dc sputtering is a basic sputtering technique using a DC power supply. This technique is only applicable to the deposition of conductive materials. The schematic of this DC sputtering system is shown in Fig 2.8.

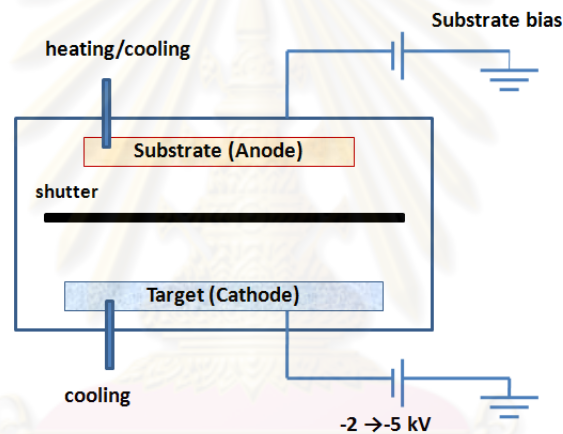


Figure 2.8: Schematic of the DC sputtering system [26].

The system is consisted of a pair of electrodes, a target (on the cathode), and a substrate (on the anode). After high bias is applied, secondary electrons from the target surface are accelerated. These high energy electrons collide with atoms, resulting in the ejection of target atoms in form of ions. The target atoms are then deposited on the substrate surface.

2.3.2 Radio frequency (RF) sputtering

RF sputtering technique can be used to deposit non-conductive films such as SiO_2 , Al_2O_3 , BaZrO_3 . The schematic of the RF sputtering is shown in Fig 2.9.

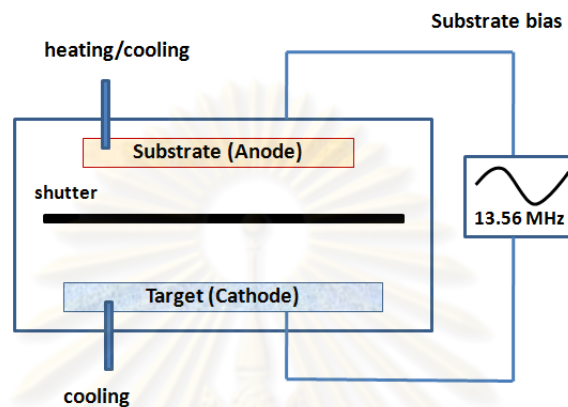


Figure 2.9: Schematic of the RF sputtering system [26].

By using an RF generator, the sinusoidally alternative voltage is applied between cathode and anode. In the alternative voltage cycles, the Ar ions are accelerated to the target surface with enough energy to cause sputtering. The alternative voltage frequency typically used for this sputtering technique is 13.56 MHz (which is in a radio frequency range).

2.3.3 Magnetron sputtering

The magnetron sputtering can be applied to both the DC and RF sputtering systems. The principle of magnetron sputtering is to add a magnet of 200 Gauss behind the target in order to trap the free electrons around the vicinity of the target, which can sequentially enhance the sputtering deposition rate by increasing the ionizing effect. This mechanism provides the advantage of trapping not only the free electrons, but also the charged species on the target surface, which in turn improve the film uniformity and homogeneity.

2.4 Parameters in The Sputtering Technique

A variety of parameters which significantly affect the film properties and deposition rates include substrate material, partial pressure and substrate temperature. The effect of each parameter is described below.

2.4.1 Substrate materials

The physical properties of substrate materials such as their melting point and thermal expansion coefficient are crucial factors on the film growth. Low melting point materials such as plastic or polymer are not suitable to be deposited on the substrate. The large amount of heat generated during sputtering process can cause these materials to melt. In additions, the large difference of the thermal expansion coefficients between the substrate and film can cause film cracks. Table 2.1 summarizes the melting point and thermal expansion coefficients of materials which are normally used as substrates in the sputtering process.

Table 2.1: The melting points and thermal expansion coefficients of some substrate materials [27, 28].

Substrate material	Melting point (°C)	Thermal expansion coefficient ($10^{-6}K^{-1}$)
Al (f.c.c.)	660	23.5
Au (f.c.c.)	1064	14.1
Fe (γ)	1534	>14.6
BaZrO ₃ (perovskite)	2600	7.8
Si	1412	7.6
Si ₃ N ₄ (β) (hexagonal)	2442	2.11

In this study, Y-doped BaZrO₃ thin films were deposited on Si wafers with 700-nm SiO₂ surface layers which have a high melting point and matching thermal expansion coefficient. Furthermore, to prevent the Si diffusion which could cause the drop of conductivity, 700 nm SiO₂ surface layer is used as a buffer layer between Si wafer and BYZ thin film.

2.4.2 Partial pressure of Ar

The partial pressure of ionized gas (or also known as the sputtering gas pressure) affects the mean free path of the atom which indicates the probability of collisions among gas molecules.

Argon is a common choice of the sputtering gas. At low partial pressure of Ar, fewer gas molecules collide with one another, therefore, gas molecules can directly transport to the surface of the film. On the other hand, at high pressure, due to higher number of gas molecules contained in the chamber, there is more probability of gas molecule collisions. These collisions can slow down the gas movement and also reduce the energy of the gas molecules, which in turn affect the deposition rate and properties of the deposited film.

2.4.3 Substrate Temperature

Substrate temperature mainly impacts on the composition, structure and morphology of the film. The density and uniformity of the deposited film can be improved by increasing the substrate temperature. Furthermore, the substrate temperature can substantially affect the atom mobility and the rate of chemical reaction on the the substrate.

CHAPTER III

EXPERIMENTAL METHODS AND CHARACTERIZATION TECHNIQUES

In this chapter, the fabrication technique of Y-doped BaZrO₃ (BYZ) dense pellet and thin film samples are discussed, and the characterization methods for the physical properties of both pellet and thin film samples are introduced. In this study, the physical properties of the starting powders and samples were examined by particle size distribution (PSD), archimedes method, X-ray diffraction (XRD), scanning electron microscope (SEM) and field emission scanning electron microscope (FE-SEM). Lastly, the proton conductivity was measured by electrochemical impedance spectroscopy technique (EIS).

3.1 Pellet Samples Preparation

BaZr_{1-x}Y_xO_{3-δ} pellet samples with x= 0.06, 0.1, 0.2, 0.3 and 0.4 were prepared by the solid state reaction [18, 22] (Fig 3.1). The starting raw materials were BaCO₃ (Baker, purity: 99.99%), 3 mol% Yttria Stabilized Zirconia (YSZ)(TOSOH : 99.9%), micro-Y₂O₃ (ALDRICH : 99.9%) and nano-Y₂O₃ (<50 nm ALDRICH : 99.99%). The experiments were consisted of two parts as follow:

(i) micro-Y₂O₃-BYZ pellets:

Micro-Y₂O₃, BaCO₃ and 3 mol% YSZ powders were used to prepare pellets.

(ii) nano-Y₂O₃-BYZ pellets:

Nano-Y₂O₃, BaCO₃ and 3 mol% YSZ powders were used to prepare pellets.

The raw powders were mixed and ball-milled in isopropanol using zirconia balls of 5 mm diameter. The mixed powder was then dried at 105°C and calcines at 1400°C for 10 h. Table 3.1 shows the mass loss occurs after calcination, corresponding to the removal of carbonates.

Table 3.1: Mass loss after calcination at different dopant concentrations

Y content (at%)	Mass loss(%)
6	15.3
10	15.1
20	21.6
30	13.1
40	13.4

Subsequently, 1 wt% ZnO were added to the calcined powder as an additive in order to lower the sintering temperature as suggested by S.Tao [22] and P.Babilo [30]. The calcined powder was again ball-milled for 24 h for homogeneity. The pellet with a diameter of 13 mm were formed by uniaxial pressing at 20 MPa, followed by the cold isostatic pressing at 220 MPa. The pellets were then sintered at 1400°C for 10 h in air. The influence of Y₂O₃ particle size on the physical properties of BYZ pellets was subsequently studied.

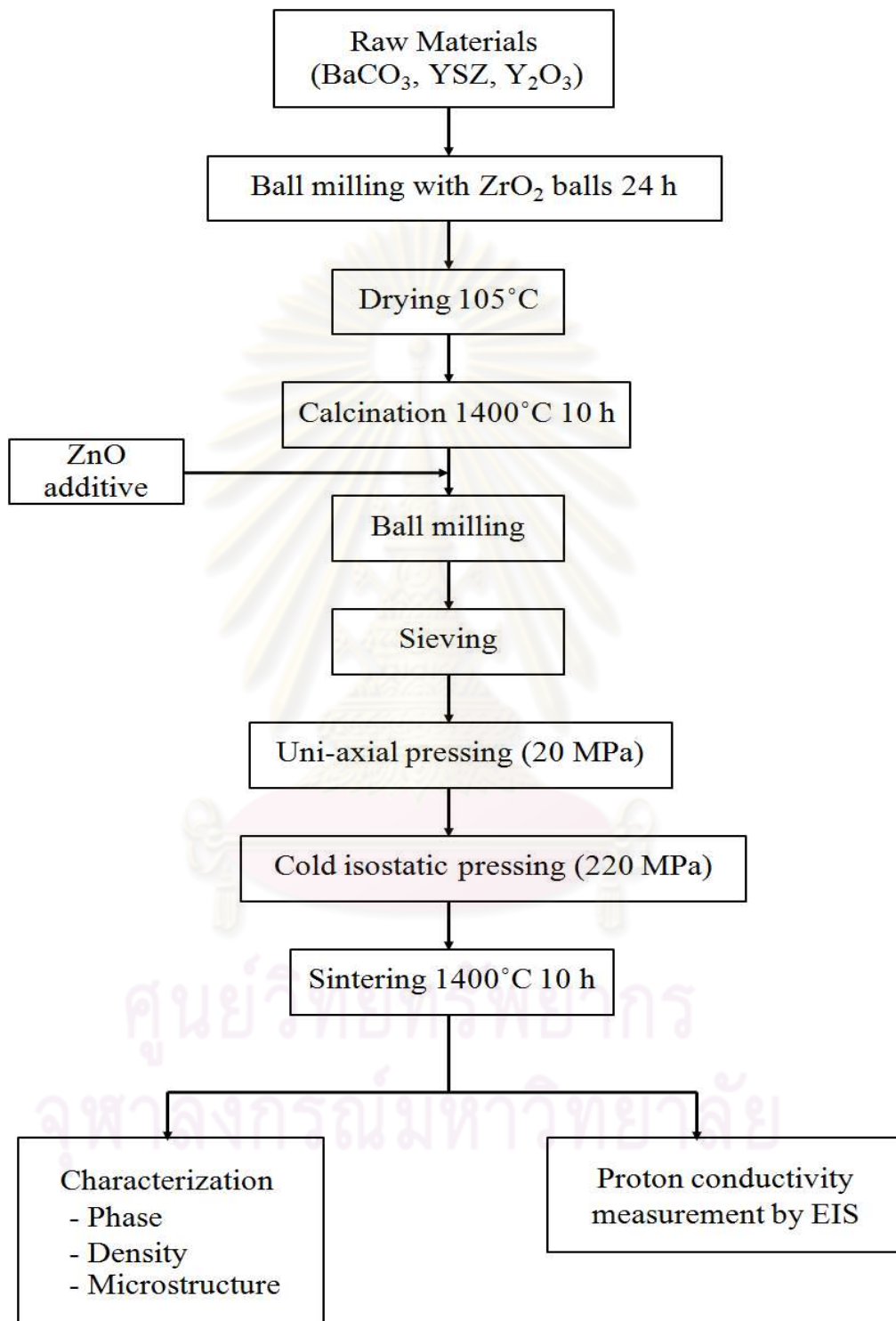


Figure 3.1: Experimental procedure of pellet sample preparation

3.2 Thin Film Fabrication

3.2.1 Sputter deposition

The sputtering equipment used in this work is ATC 2000-F sputtering system (AJA) located at the National Electronics and Computer Technology Center (NECTEC)(Fig 3.2). Top and side views of the system are displayed in Fig 3.3. The system consists of three sputtering guns, of which angles the desired Z-axis position of the substrate could be optimized. The substrate is placed on a rotating stage above the target in the center of the chamber and heated by quartz lamp from behind. The vacuum system is composed of a mechanical rotary pump (ALCATEL) and turbo-molecular pump (Shimazu, TMP-803-LM). The vacuum process is monitored and controlled by Pirani gauge($1 \text{ atm}-10^{-2} \text{ mbar}$), Baraton gauge ($10^{-2}-10^{-6} \text{ mbar}$), and Ion gauge ($10^{-4}-10^{-10} \text{ mbar}$).



Figure 3.2: Schematic of AJA the sputtering system

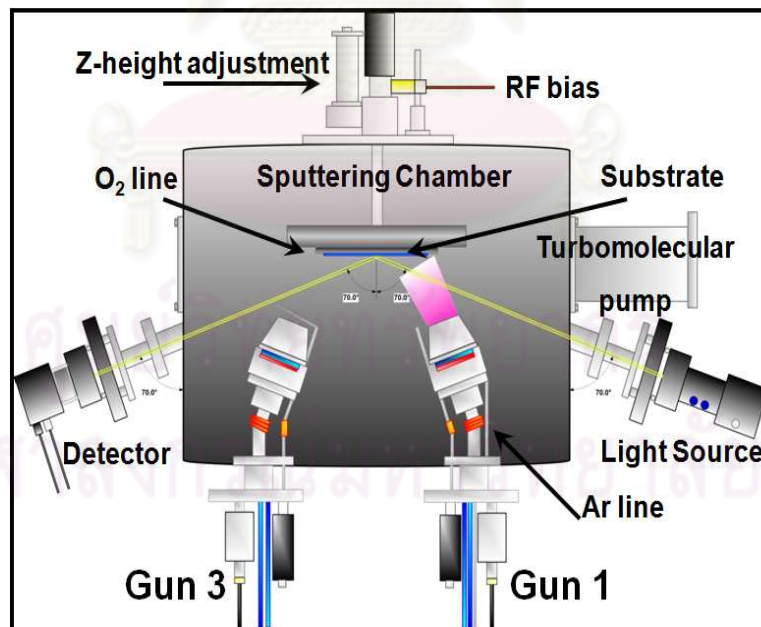


Figure 3.3: Top and side views of AJA sputtering system

3.2.2 BYZ sputtering methods

In this work, Y-doped BaZrO₃ (BYZ) thin films were fabricated by using two different sputtering methods.

- ◇ Method 1 (M1): Co-sputtering of Y and BaZrO₃ targets
- ◇ Method 2 (M2): 2-step sputtering of Y-BaZrO₃ target

Method 1 (M1)

The BYZ thin films were deposited by co-sputtering of Yttrium (Y) and BaZrO₃ targets. The Yttrium sputtering was carried out with the direct current (DC) power supply system, whereas the radio-frequency (RF) power supply was applied on the BaZrO₃ target.

BaZrO₃ thin films were first fabricated to find the optimum sputtering conditions for dense and uniform films and to obtain the highest deposition rate. The optimum deposition parameters (RF power, Ar flow rate and pressure) were investigated. The RF powers and Ar flow rates were varied from 60-80 W and 35-65 sccm, respectively, whereas the Ar operating pressure were maintained 3-5 mTorr at all deposition times. Si wafers with 700-nm SiO₂ surface layer were used as a substrate for all thin film depositions. The optimum conditions for BaZrO₃ thin films deposition, which yields an average deposition rate of 0.185 Å/s are summarized in Table 3.2.

Table 3.2: Deposition parameters of BaZrO₃ thin film

RF Power	60 watt
Operating Pressure	3×10^{-3} Torr
Argon Flow	65 sccm
Z height	25

The co-sputtering of Y-doped BaZrO₃ was subsequently performed under the condition summarized in Table 3.3 . The DC power applied on the Yttrium target was varied from 3-15 W. The substrates were rotated and heated at 700°C during the deposition. After the sputtering process, all BYZ samples were annealed in air at 800°C for 3h.

Table 3.3: Deposition parameters of Y-doped BaZrO₃ (BYZ) thin film

RF Power	60 watt
DC Power	3-15 watt
Base Pressure	3.5×10^{-7} Torr
Operating Pressure	3×10^{-3} Torr
Argon Flow	65 sccm
Z height	25
Substrate Temperature	700°C
Deposition Time	2 hours

Method 2 (M2)

The BYZ thin films were achieved by sputtering the modified Y-BaZrO₃ target. The preparation procedures of the modified Y-BaZrO₃ target were shown in Fig 3.4. Yttrium(Y) was first deposited on the BaZrO₃ target at Y-window angle of 20 to 40 degrees. The conditions of Yttrium deposition were summarized in Table 3.4. About ~365 nm of Yttrium film were deposited on the BaZrO₃ target.

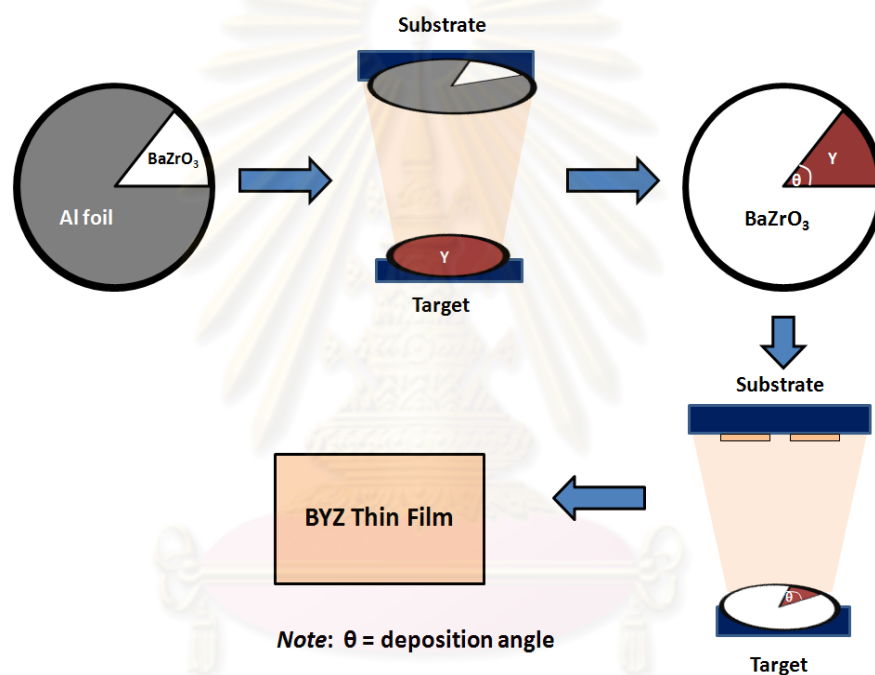


Figure 3.4: Schematic of the M2 fabrication procedure and the modified Y-BaZrO₃ target

Table 3.4: Deposition parameters of Yttrium film on the BaZrO₃ target

RF Power	100 watt
Base Pressure	5×10^{-7} Torr
Operating Pressure	5×10^{-3} Torr
Argon Flow	35 sccm
Z height	25
Deposition Time	45 min
Deposition Angle	20,30,40

Subsequently, the modified Y-BaZrO₃ target was sputtered using the RF power supply to deposit BYZ thin films. The deposition conditions were summarized in Table 3.5. Subsequently, the samples were annealed in air at 800°C for 3h.

Table 3.5: Deposition parameters of BYZ thin films fabricated by the M2 method

RF Power	60 watt
Base Pressure	3.5×10^{-7} Torr
Operating Pressure	3×10^{-3} Torr
Argon Flow	65 sccm
Z height	25
Substrate Temperature	-
Deposition Time	2 hours

3.3 Characterization Techniques

3.3.1 Particle size by Light scattering method

Particle size and particle size distribution were analyzed by the laser light scattering method using Mastersizer instrument. Distilled water was used as the dispersing medium. This method utilized the interaction between the laser beam and the suspended particles. As the laser beam strikes an assembly of particles, some part of the beam is diffracted, absorbed and transmitted. The diffracted laser beam passes through the condenser lens creating images on the detector. The diffraction pattern of the diffracted laser beam corresponds to the mean particle size distribution, whereas the intensity values is converted to the particle size of the powders.

3.3.2 Density by Archimedes method

The bulk density of green body and sintered pellet samples were determined by Archimedes' method using water as the immersion medium. At the beginning, the pellet samples were dried at 105°C and weighted which was referred to as dry weight (W_d). The specimens were then placed in vacuum for 30 minutes. After that, the specimen was kept under water for 15 minutes. The saturated weight and suspended weight were then measured. The bulk density was then calculated using Eq. 3.1.

$$\text{Bulk density} = \left(\frac{W_d}{W_{sat} - W_{sus}} \right) \times \rho_{water} \quad (3.1)$$

where W_d = the dry weight

W_{sat} = the saturated weight

W_{sus} = the suspended weight.

ρ_{water} = density of water (1 g/cm³)

The theoretical density (ρ) was determined from the unit cell data as followed:

$$\rho = \frac{n(\sum A_C + \sum A_A)}{V_C N_A} \quad (3.2)$$

where n = the number of formula units within the unit cell

ΣA_C = the sum of the atomic weight of all cations in the formula unit

ΣA_A = the sum of the atomic weight of all anions in the formula units

V_C = the unit cell volume

N_A = Avogadro's number, 6.023×10^{23} formula units/mol

By comparing the bulk density to the theoretical density, the relative density of specimens were obtained as shown in Eq. 3.3.

$$\text{The relative density} = \frac{\text{Bulk density}}{\text{Theoretical density}} \times 100 \quad (3.3)$$

3.3.3 Microstructures by Scanning electron microscopy (SEM)

Scanning electron microscope (SEM) is a type of electron microscopes which is used to examine the morphology of BYZ pellet samples. High-energy electron beam generated by a heated tungsten filament is scanned across the sample surface. The electron beam interacts with atoms in the sample producing several signals such as secondary electrons, back scatter electrons and characteristic x-ray etc. The secondary electrons are the signal used to create an SEM image. The intensity of this signal is converted into an image on a Cathode-Ray tube (CRT). The CRT display represents the morphology and surface of sample [32].

In this study, microstructures of the sintered pellet samples were examined by SEM (JEOL, JSM 6400). The sintered pellets were polished, and thin gold layer was deposited on the surface to reduce the electrical charging.

3.3.4 Microstructure by Field emission scanning electron microscopy (FE-SEM)

The field-emission scanning electron microscope (FE-SEM; Hitachi model S-4700) was used to examine surface and cross-section microstructures of BYZ thin film samples. The equipment was located at Thai Micro Electronic Technology Center Thailand (TMEC). FE-SEM used a highly focused electron beam to strike and interact with the surface of sample under in an ultrahigh vacuum environment creating a high resolution image.

FE-SEM is able to deliver ultra-high resolutions down to 1 nm. Moreover, the ultra-high resolution operate over the complete voltage range with probe currents up to 20 nA and are available with variable thin film technology. The signals gathered from an FE-SEM may include secondary electrons, back scattered electrons, characteristic x-rays and Auger electrons. These signals are not only generated from the primary beam impinging upon the sample, but also from other interactions of atoms near the surface. BYZ films thickness and surface morphology were observed at 50,000-100,000 magnification using the voltage of 10 kV.

3.3.5 Crystallography by X-Ray diffraction

X-ray diffraction is an analytical technique which is used to determine the crystal structure of materials. When X-ray radiations are collimated toward a crystal, the electron of crystal will scatter the beam through a wide range of angles. According to Bragg's law (Eq. 3.4), the scattered X-ray beam creates the constructive interfere when the path difference is equal to the wavelengths [31] as shown in Fig 3.5.

$$2d \sin \theta = n\lambda \quad (3.4)$$

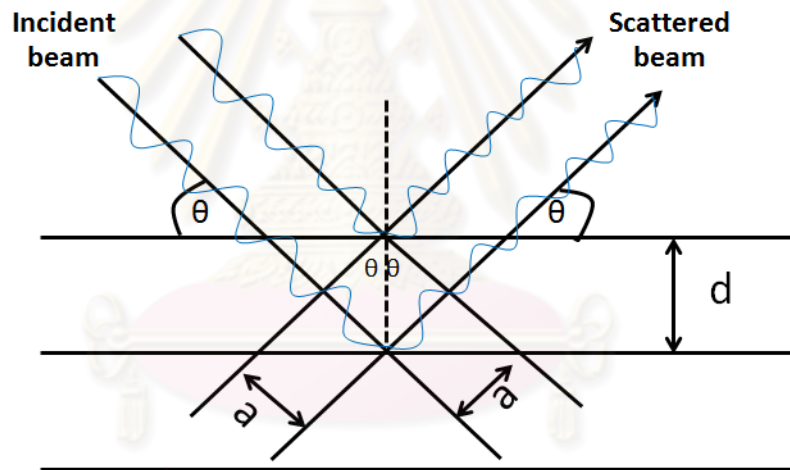


Figure 3.5: Schematic of XRD measurement

The lattice parameter of the cubic system can be calculated from Eq. 3.5-3.6.

$$d = \frac{a}{(h^2 + k^2 + l^2)^{\frac{1}{2}}} \quad (3.5)$$

$$a = \frac{\lambda}{2 \sin \theta} (h^2 + k^2 + l^2)^{\frac{1}{2}} \quad (3.6)$$

where $n =$ an integer.

$d =$ a spacing between surface.

$\Theta =$ the angle of the radiation on the crystal surface.

$\lambda =$ the wavelength of the radiation.

$a =$ the lattice parameter.

$(hkl) =$ lattice plane identified by Miller indices.

Phase analysis of pellet samples were investigated by X-ray diffractometer (Bruker AXS), using Cu $K\alpha$ radiation ($\lambda = 1.5418 \text{ \AA}$) and operating at 40 kV and 30 mA. The data were obtained in the 2Θ range of $10\text{-}90^\circ$ with a step scan of 0.05 degree.

Thin film phase identifications were inspected using Rigaku X-Ray diffractometer, TTRAXIII theta-theta rotating anode. The measurement was operated at 40 kV and 30 mA. The data were obtained in the 2Θ range of $10\text{-}80^\circ$ with a step scan of 0.05 degree.

ศูนย์วิทยทรัพยากร
จุฬาลงกรณ์มหาวิทยาลัย

3.3.6 Proton conductivity by electrochemical impedance spectroscopy

Four main techniques are usually applied to measure the conductivity of oxide samples: two-probe DC, four probe DC, fixed frequency AC and impedance spectroscopy. The impedance spectroscopy has been widely used at the present because it can distinguish the different ionic conduction mechanism in polycrystalline materials.

Impedance Definition

Electrochemical impedance spectroscopy is a technique used for measuring the proton conductivity of the sample by applying an alternating potential over a range of frequencies. When an alternating potential (voltage) is applied across an electrochemical cell, a current responds accordingly through the electrodes and movement of ion through the electrolyte. This movement causes the different responses between the potential and the flow of electrical current on the conduction mechanism [33]. Impedance (Z) is given by the ratio between a time-dependent potential and the corresponding time-dependent current at each applied frequency as shown in Eq. 3.7 .

$$Z = \frac{V(t)}{I(t)}; \quad (3.7)$$

where $V(t) = V_o \cos(\omega t)$, $I(t) = I_o \cos(\omega t - \phi)$. $V(t)$ and $I(t)$ are the potential and current at time t . V_o and I_o are the amplitude of the voltage and current signal, ω is the radial frequency, and ϕ is the phase shift. The impedance (Z) of the system can then be written as

$$Z = \frac{V_0 \cos(\omega t)}{I_0 \cos(\omega t - \phi)} = Z_0 \frac{\cos(\omega t)}{\cos(\omega t - \phi)} \quad (3.8)$$

Using Euler relationship (Eq. 3.9), the impedance can be expressed as a complex function as given in Eq. 3.10-3.11.

$$\exp(j\phi) = \cos \phi + j \sin \phi \quad (3.9)$$

$$Z = \frac{V_0 \exp(j\omega t)}{I_0 \exp(j\omega t - j\phi)} \quad (3.10)$$

$$Z = Z_0 \exp(j\phi) = Z_0 (\cos \phi + j \sin \phi) \quad (3.11)$$

The resulting impedance is usually summarized in a Bode plot and Nyquist plot as shown in Fig 3.6. The Nyquist plot represents a real (Z') part and an imaginary part of the impedance (Z'') on the x-axis and y-axis respectively (Fig 3.6(a)). In a Bode plot, the absolute impedance ($|Z|$) and the phase shift (ϕ) are plotted with respect to the radial frequency (Fig 3.6(b)).

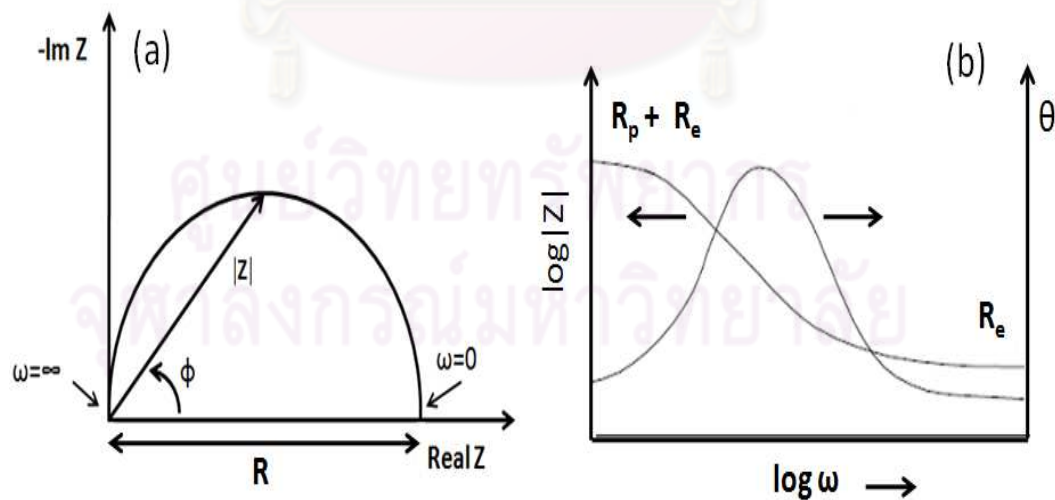


Figure 3.6: Schematic of (a) Nyquist plot (b) Bode plot [35].

Impedance spectra analysis

The Nyquist plot of ionic conducting polycrystalline oxides consist of three main semicircles, which are usually described by the equivalent circuit of R-C element connected in series (Fig 3.7). Bauerel et al.[34] performed an analysis to elucidate the physical meaning of each semicircle and reported that the highest frequency semicircle corresponded to the bulk impedance, while the intermediate and the lowest frequency ones corresponded to the grain boundary and the electrode responses, respectively.

In the Nyquist plot, the applied frequency increases from the right to the left. The diameter of the highest frequency arc represents the bulk resistance (R_b), whereas the one at the intermediate frequency indicates the grain boundary resistance ($R_{G.B.}$). In addition to resistance, the typical capacitance values of bulk and grain boundary of BYZ can be extracted. The typical capacitance were in the order of 10^{-11} F and 10^{-9} F for the bulk and grain boundary, respectively [14, 36]. The low-frequency arc corresponds to the electrode response (R_E), which is based on the electrochemical reactions at the interfere.

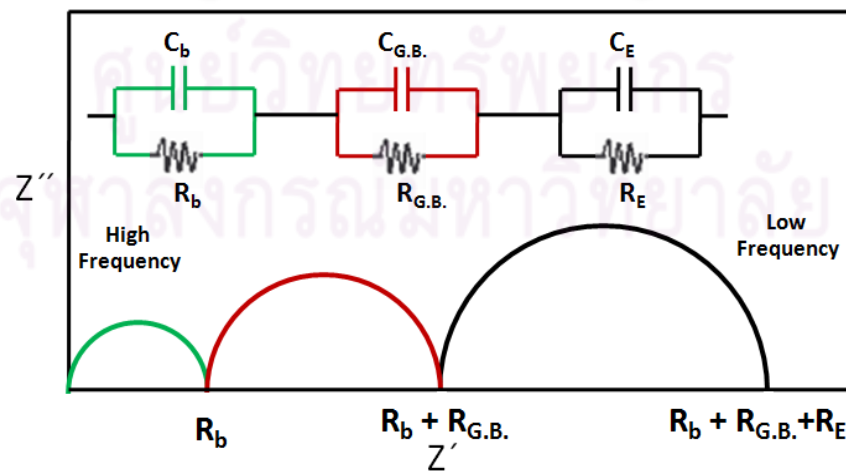


Figure 3.7: Idealized Nyquist plot of ceramic oxides and its equivalent circuit[35].

The calculation of the proton conductivity is based on the Ohm's law (Eq. 3.12-3.15). The thickness and surface area used to calculate the proton conductivity of pellet and thin film are illustrated in Fig 3.8(a) and Fig 3.8(b), respectively.

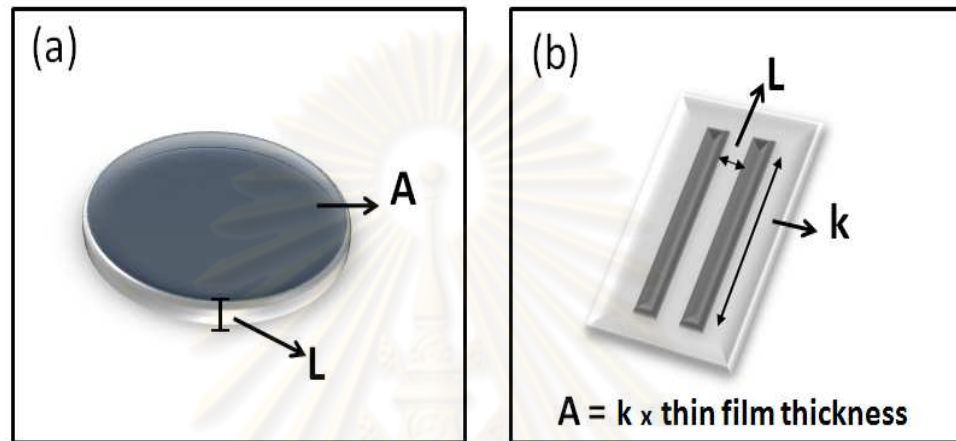


Figure 3.8: Factors for the proton conductivity calculation (a) pellets (b) thin films.

$$V = IR, R = \frac{V}{I} \quad (3.12)$$

$$R = \rho \frac{L}{A} \quad (3.13)$$

$$\rho = R \frac{A}{L} \quad (3.14)$$

$$\sigma = \frac{1}{\rho} = \frac{L}{RA} \quad (3.15)$$

where

V = applied voltage (V)

I = Current (A)

R = Resistance (Ω)

ρ = Resistivity ($\Omega \cdot \text{cm}$)

σ = Conductivity (S/cm)

L = Sample thickness (cm)

A = Cross-sectional area (cm^2)

By using the Arrhenius's equation (Eq. 3.16), the conductivity can be expressed as following:

$$\sigma_T = \frac{A}{T} \exp\left(\frac{-E_a}{RT}\right) \quad (3.16)$$

$$\ln \sigma_T T = \frac{-E_a}{RT} + \ln\left(\frac{A}{T}\right) \quad (3.17)$$

where

E_a = Activation energy (J/mol)

T = Temperature (K)

R = Universal gas constant (8.314 J/K.mol)

A = The pre-exponential factor

From Eq. 3.17, the slope of the Arrhenius plot of $\ln \sigma T$ can determine the activation energy of the conductivity.

The impedance measurement system

The set-up of the AC-impedance measurement for this study is shown in Fig 3.9. The system consists of a tube furnace, sample holder, Solartron 1260 Impedance and data analyzer.

The BYZ pellets were coated with gold paste on both sides as electrodes and then fired at 800°C for 3 h, while the thin film conductivity was measured across the BYZ thin film surfaces by using silver paste as electrodes. The samples were then loaded in a sample holder. The impedance spectra was measured in the frequency range of 10^{-1} - 10^7 Hz at 250-600°C in air, dry H₂ (7% H₂ in Ar) and wet H₂ (7% H₂ in Ar) atmospheres. The impedance spectra was measured at a 50°C interval with the ramping rate of 5°C/min.

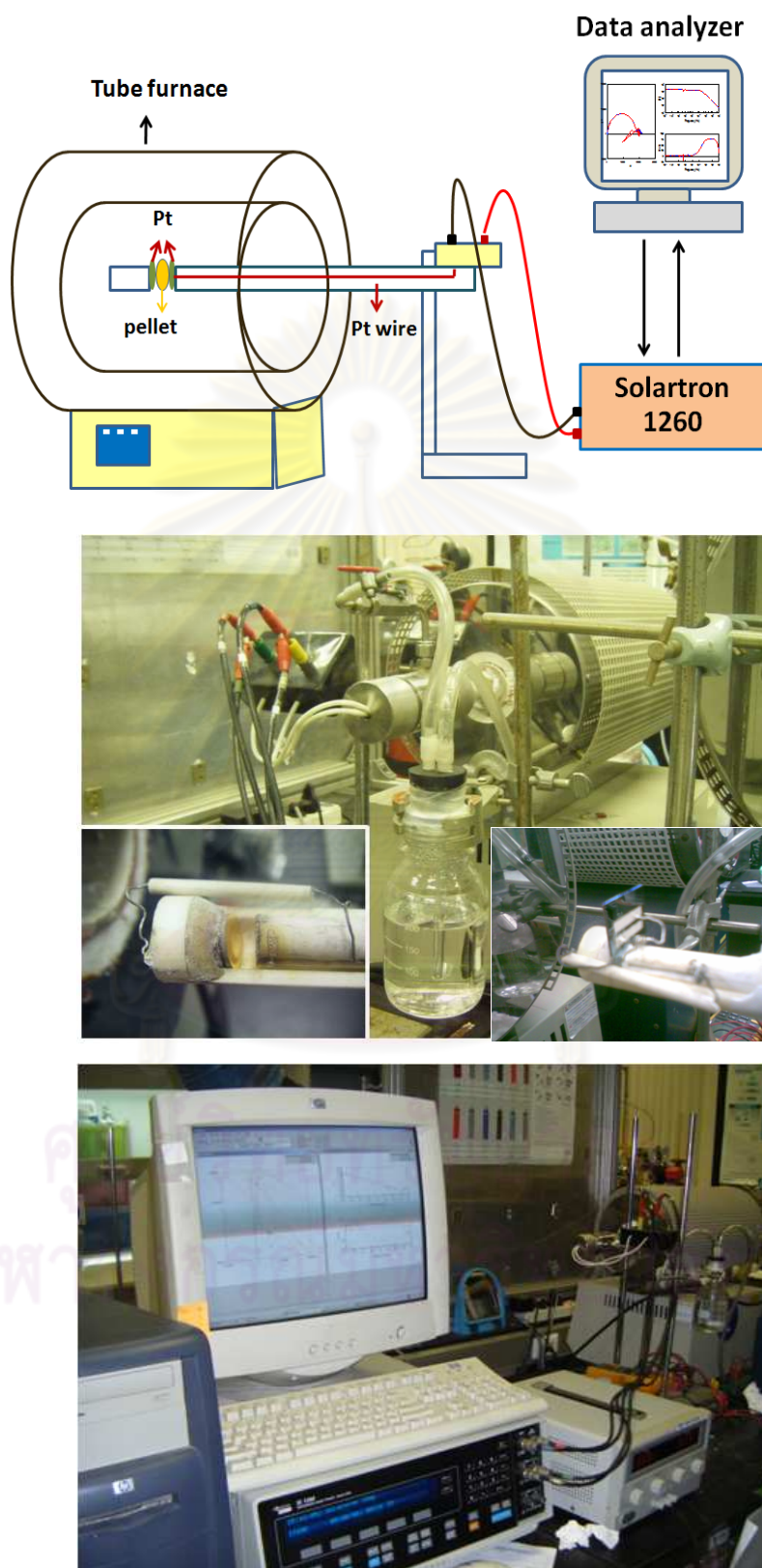


Figure 3.9: Schematic diagram of the AC-Impedance measurement

CHAPTER IV

RESULTS AND DISCUSSIONS: $\text{BaZr}_{1-x}\text{Y}_x\text{O}_{3-\delta}$ PELLETS

Several studies have been done on the proton conductivity of $\text{BaZr}_{1-x}\text{Y}_x\text{O}_{3-\delta}$ (BYZ) at different Y concentration. The discrepancy of the proton conductivity results from different studies could arise from the difference in the starting powders, fabrication procedures and EIS measurement conditions.

Therefore, the aim of this chapter is to study the influence of Y_2O_3 particle size and the Y doping concentration on the physical properties (phase, density and microstructure) $\text{BaZr}_{1-x}\text{Y}_x\text{O}_{3-\delta}$ pellet samples. Furthermore, the effects of the sintering process and EIS atmosphere on the proton conductivity of BYZ pellet samples are further analyzed and discussed. The proton conductivity results obtained from this study will be later compared with the BYZ thin film proton conductivities in the following chapter.

4.1 Particle Size of Raw Materials

The average particle sizes and particle distribution of raw materials (BaCO_3 , 3 mol% yttria stabilized zirconia (YSZ), micro- Y_2O_3 powder and nano- Y_2O_3 powder), used to prepare the BYZ pellet samples are summarized in Table 4.1 and Appendix A, respectively. The particle sizes were analyzed by the light scattering technique.

Table 4.1: Particle size of raw materials

Raw materials	Average particle size(μm)
3 mol% Yttria Stabilized Zirconia (YSZ)	36.08
Barium carbonate (BaCO_3)	13.53
Yttrium oxide (Y_2O_3)–micro particle	41.06
Yttrium oxide (Y_2O_3)–nano particle	7.91

After the calcination process, the particle size of calcined powders were re-analyzed as shown in Table 4.2. The particle size increases with increasing Y concentration in both micro- Y_2O_3 -BYZ and nano- Y_2O_3 -BYZ. The results show that the particle sizes of nano- Y_2O_3 -BYZ are smaller than those of micro- Y_2O_3 -BYZ. The particle sizes of the calcined powders are larger than those of the raw materials, which are likely caused by the agglomeration of the powder after the calcination process.

Table 4.2: Particle size of calcined powders

$\text{BaZr}_{1-x}\text{Y}_x\text{O}_{3-\delta}$	Micro- Y_2O_3 -BYZ (μm)	Nano- Y_2O_3 -BYZ (μm)
x= 0.06	35.25	5.44
x= 0.10	35.69	5.95
x= 0.20	37.77	6.87
x= 0.30	37.17	6.25
x= 0.40	45.13	7.56

4.2 XRD Patterns of BYZ Pellet Samples

The XRD patterns of the sintered BYZ pellets prepared from the micro- Y_2O_3 and nano- Y_2O_3 powders are presented in Fig 4.1(a) and (b), respectively. Most of the XRD peaks of the sintered BYZ pellets match well with the perovskite crystal structure of BaZrO_3 (JCPDS no. 00-006-0399).

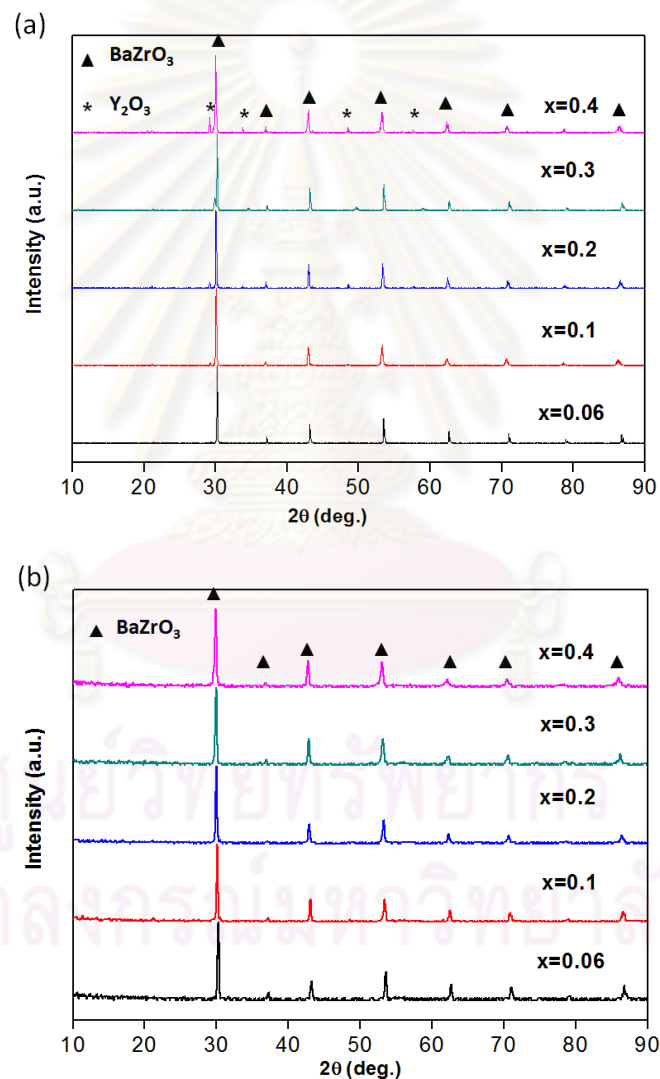


Figure 4.1: XRD patterns of the sintered BYZ pellet samples with $x= 0.06$ - 0.4
 (a) micro- Y_2O_3 -BYZ and (b) nano- Y_2O_3 -BYZ

As shown in Fig 4.1(a), when $x \geq 0.3$, the Y_2O_3 (JCPDS no. 00-043-1036) peak were observed within the micro- Y_2O_3 -BYZ samples. The Y_2O_3 secondary phase may be arise from the incomplete solid state reaction due to the large particle size of raw materials and the low sintering temperature. However, once Y_2O_3 micro-powder was replaced by Y_2O_3 nano-powder, the second phase was no longer observed (Fig 4.1(b)).

Lattice parameters of BYZ pellet were extracted from the XRD results and plotted with respect to Y content in Fig 4.2. The results reveal that the lattice parameters of $BaZr_{1-x}Y_xO_{3-\delta}$ increases with the increasing Y doping concentration due to the larger ionic radius of Y^{3+} (0.90 \AA) incorporated into the Zr^{4+} site (ionic radius of 0.72 \AA). In the nano- Y_2O_3 -BYZ samples, the lattice parameter is ranging from 4.179 to 4.226 \AA with increasing Y content from 6 to 40 at%, whereas that of the micro- Y_2O_3 -BYZ is increased from 4.160 - 4.188 \AA with increasing Y content from 6 to 30 at%. However, in the micro- Y_2O_3 -BYZ samples, as x reaches 0.4, the lattice parameter decrease to 4.172 \AA as a result of secondary phase.

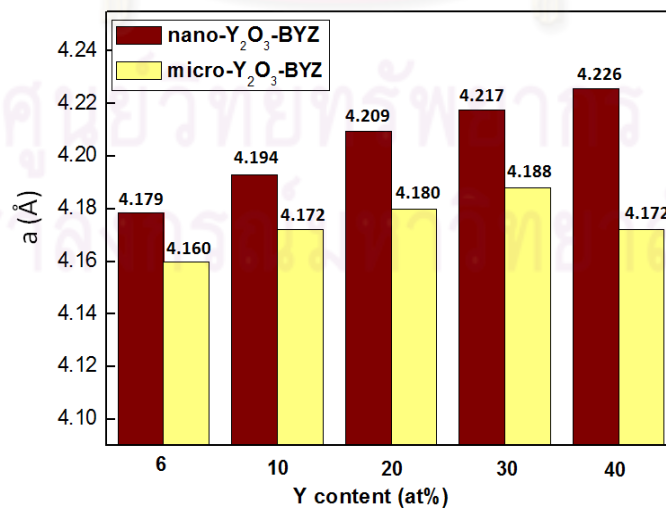


Figure 4.2: The lattice parameter of BYZ pellets after sintering at 1400°C

The lattice parameters obtained from $\text{BaZr}_{1-x}\text{Y}_x\text{O}_{3-\delta}$ pellets with $x= 0.06-0.4$ are compared to the results from the previous reported literatures [15, 18] in Fig 4.3. Kreuer et.al [15] and Iguchi et.al [18] reported the larger lattice parameter than the results from this work. Kreuer et al.[15] found an increasing tetragonal distortion above 10 at.%, whereas, in this study, the crystal structure of BYZ sample remained cubic. This discrepancy of the crystal structures between Kreuer et.al's and our works may cause the difference of the lattice parameters.

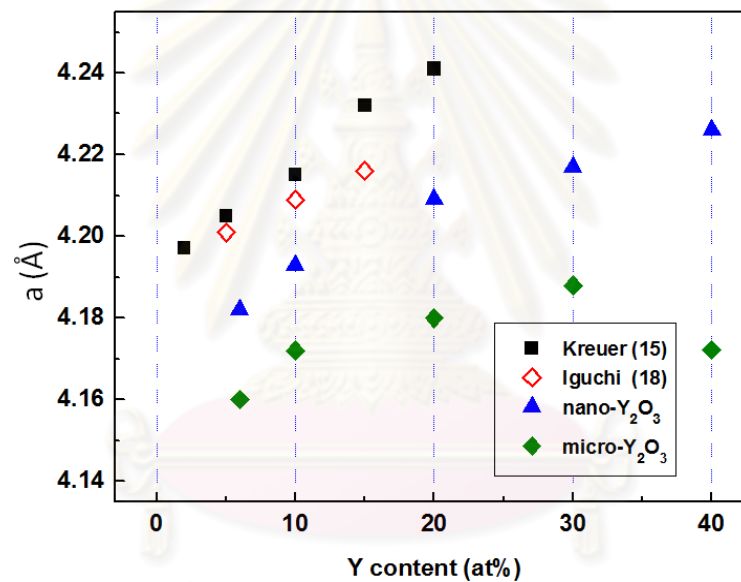


Figure 4.3: The lattice parameters of $\text{BaZr}_{1-x}\text{Y}_x\text{O}_{3-\delta}$ at $0.06 \leq x \leq 0.4$ obtained from this study compared to the values from the previously reported literatures; applied from Kreuer[15] and Iguchi[18].

4.3 Microstructure of BYZ Pellet Samples

4.3.1 Densification

Densities of the BYZ green and sintered bodies are summarized in Fig 4.4 and Appendix B. The relative BYZ green body densities of micro- Y_2O_3 -BYZ samples reach $\sim 55\%$, which are approximately the same as those of the nano- Y_2O_3 -BYZ. After sintering, the densities of both systems are close to the theoretical density. In micro- Y_2O_3 -BYZ, when $x < 0.4$, the densities of the pellet reach $\sim 95\%$. However, the density declines to 83% when $x = 0.4$ which is likely caused by the occurrence of the secondary phase (Y_2O_3) due to the incomplete solid state reaction of large Y_2O_3 particle in the starting powder. The density of nano- Y_2O_3 -BYZ reaches over 97% and no decline in the density of the sample with increasing Y content is observed.

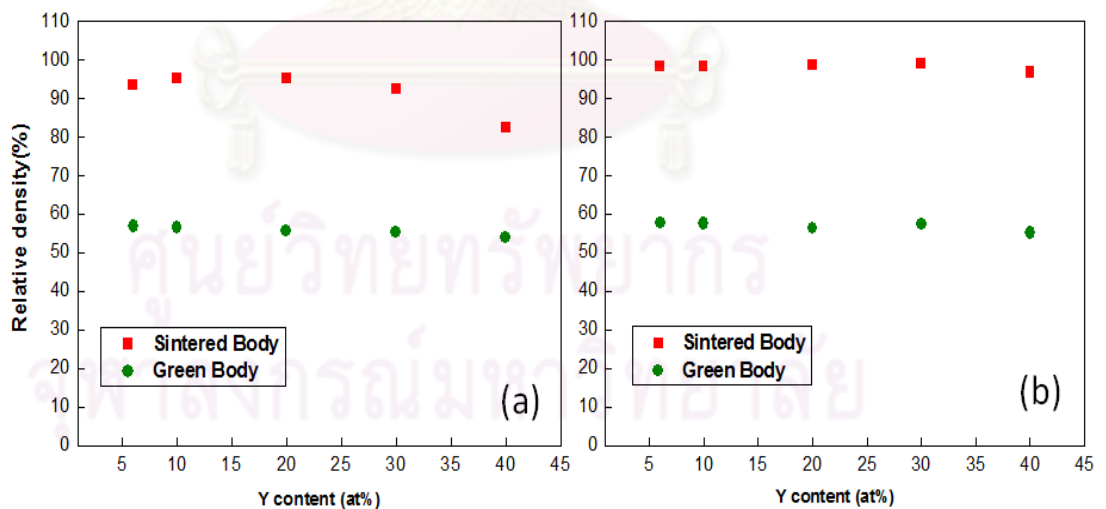


Figure 4.4: Relative density of green and sintered bodies of (a) micro- Y_2O_3 -BYZ and (b) nano- Y_2O_3 -BYZ

4.3.2 Microstructure

The SEM images of green bodies, sintered bodies, cross-sectioned and polished samples are displayed in Fig 4.5. The green bodies have porous microstructures with a small grain size of $0.32 \mu\text{m}$. After sintering at 1400°C with the addition of ZnO, the dense BYZ-pellet samples can be achieved. The grain diameter of the sintered bodies are about $1.2 \mu\text{m}$, which are larger than those of green bodies.

Fig 4.5(c) reveal the lower density of BYZ pellet surface than that of bulk BYZ, which could arise from the BaO evaporation during sintering process of BYZ as suggested by Snijker et.al [14] and Shima et.al [37]. The Ba loss, which mainly occurs at high temperature, causes the stoichiometric variation in the BYZ pellet sample.

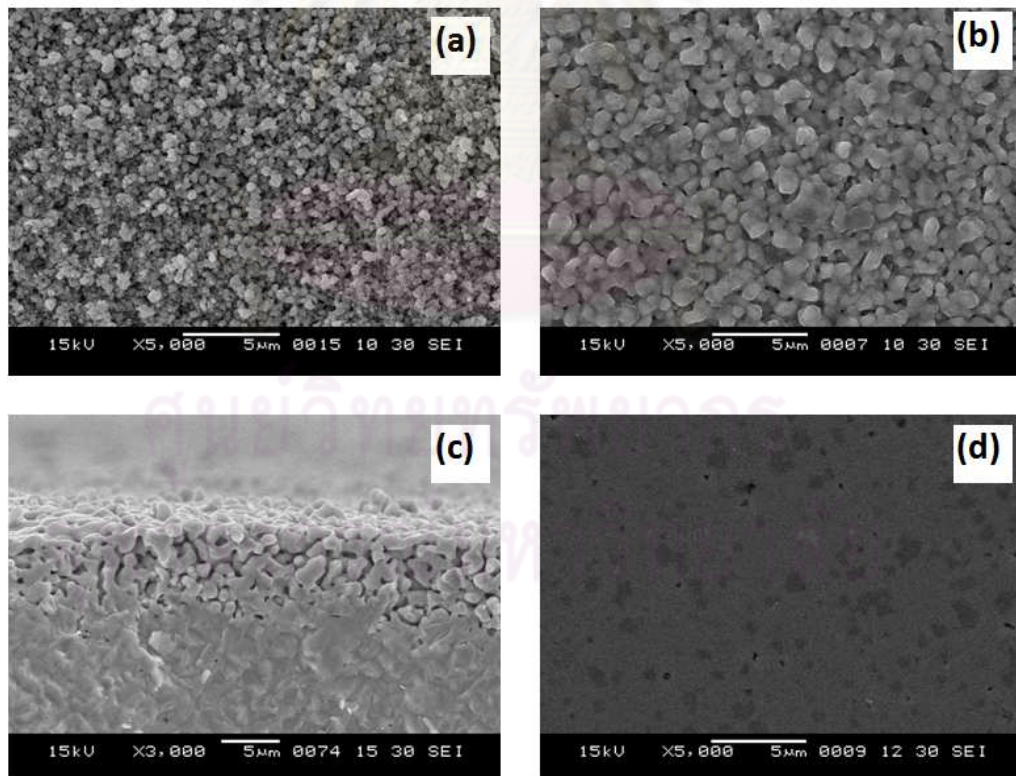


Figure 4.5: SEM images of (a) green body (b) sintered body (c) cross-section and (d) polished Nano- $\text{Y}_2\text{O}_3\text{-BaZr}_{0.8}\text{Y}_{0.2}\text{O}_{3-\delta}$ pellet samples

The comparison of the microstructural images of micro-Y₂O₃-BYZ and nano-Y₂O₃-BYZ at different Y contents are depicted in Fig 4.6. The grain size of micro-Y₂O₃-BYZ are about 0.65 μm, which are smaller than that of the nano-Y₂O₃-BYZ (~ 1.2 μm). Small pores could be detected in both systems, although the nano-Y₂O₃-BYZ samples show fewer and smaller pores than that of micro-Y₂O₃-BYZ.

The effect of excess porosity and secondary phase in micro-Y₂O₃-BYZ pellets could result in the lower total conductivity as reported by Kosasang et.al [39]. Therefore, only BYZ pellet samples with nano-Y₂O₃ starting powder were chosen for further proton conductivity measurements.



ศูนย์วิจัยทรัพยากร
จุฬาลงกรณ์มหาวิทยาลัย

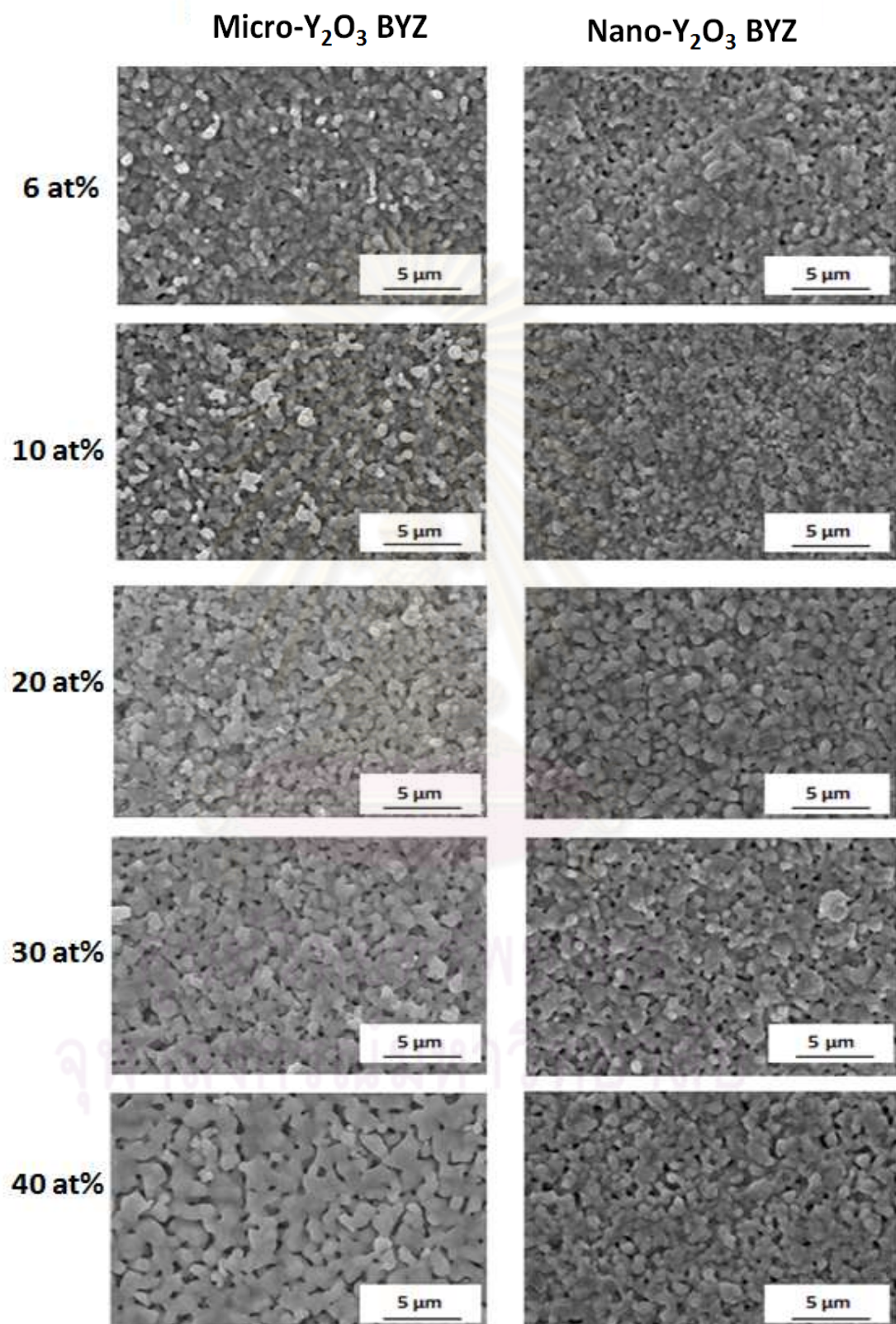


Figure 4.6: SEM images of micro-Y₂O₃-BYZ and nano-Y₂O₃-BYZ sintered bodies with 6-40 at.% Y contents

4.4 Proton Conductivity of BYZ Pellet Samples

4.4.1 Impedance spectra analysis

Bulk and grain boundary resistances of the $\text{BaZr}_{1-x}\text{Y}_x\text{O}_{3-\delta}$ pellet samples were obtained by least square fitting the equivalent circuit to the EIS results in the different frequency regimes as shown in Fig 4.7. The impedance spectra in the high frequency regime referred to the bulk response, those in the intermediate frequency corresponded to that of the grain boundary and the lowest frequency spectra were the result from the electrode response [38].

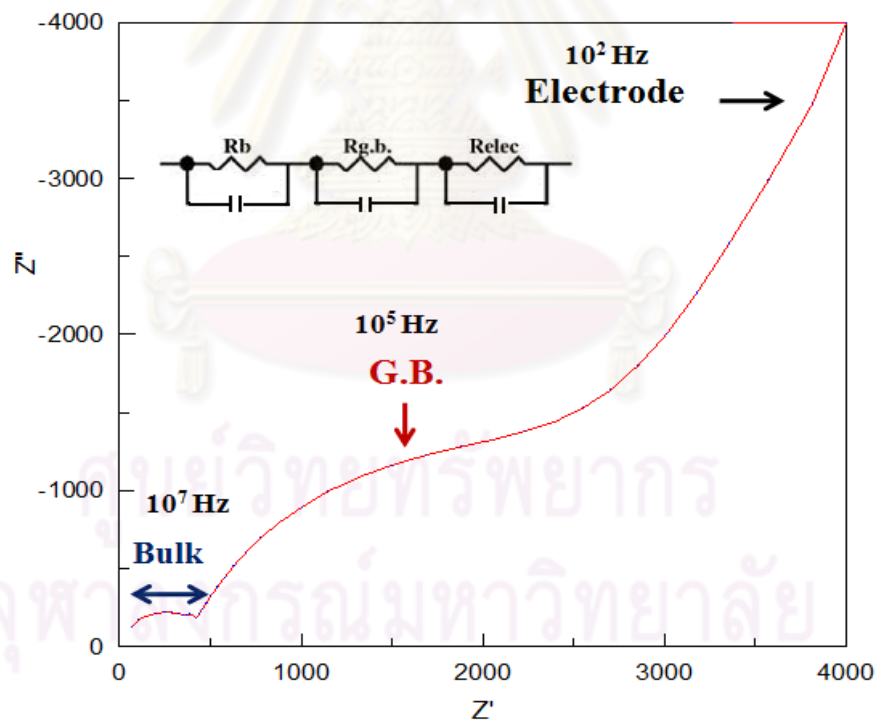


Figure 4.7: The impedance spectra of BYZ pellet sample in the different frequency.

4.4.2 Temperature dependence on the proton conduction mechanisms of BYZ pellets

The conductivities of BYZ pellet samples were measured over the temperature range of 250 - 600°C. The bulk, grain boundary and total conductivities of $\text{BaZr}_{0.8}\text{Y}_{0.2}\text{O}_{3-\delta}$ were calculated and summarized in Fig 4.8. Below 350°C, the grain boundary conductivity is about 1 orders of magnitude smaller than the bulk conductivity, indicating that the proton migration through the grain boundaries is the rate-limiting step at low temperatures. At $T > 400^\circ\text{C}$, the bulk and grain boundary conductivities become similar. Moreover, the total conductivities of $\text{BaZr}_{0.8}\text{Y}_{0.2}\text{O}_{3-\delta}$ are close to the grain boundary conductivities, meaning that the grain boundary is an important parameter affecting on the overall proton migration in the BYZ samples.

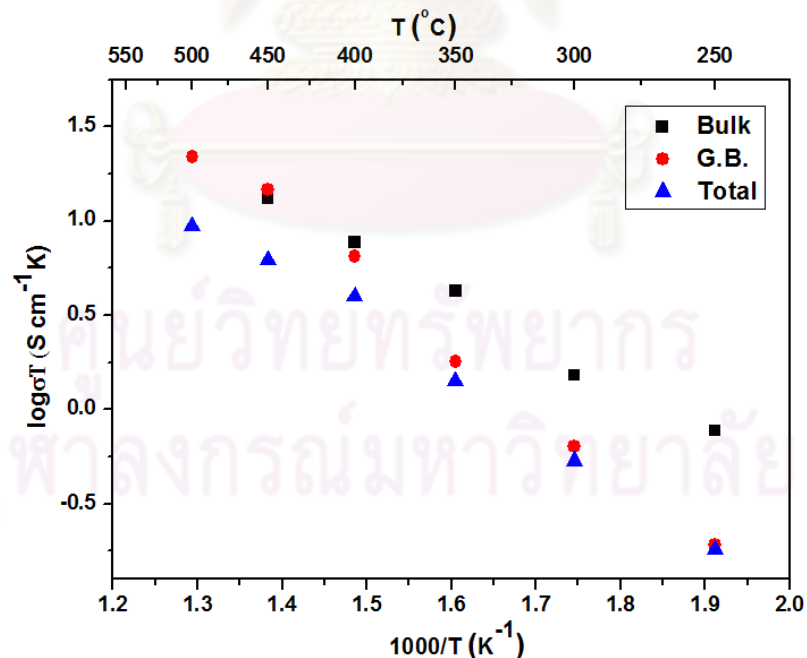


Figure 4.8: The bulk, grain boundary and total conductivities of $\text{BaZr}_{0.8}\text{Y}_{0.2}\text{O}_{3-\delta}$ in air

4.4.3 The Y content dependence on the proton conductivities of BYZ pellets

The bulk, grain boundary and total proton conductivities of $\text{BaZr}_{1-x}\text{Y}_x\text{O}_{3-\delta}$ (BYZ) pellet samples with $x = 0.06, 0.1, 0.2, 0.3$ and 0.4 are summarized in Fig 4.9-4.11 respectively. The results reveal the dependence of the proton conductivity on the Y doping concentration. The grain boundary conductivity is lower than that of bulk, which is in a good agreement with Iguchi et.al [38] and Tao [22]. The increase in the grain boundary proton conductivity is observed as x increases from 0.06 up to 0.2. The highest grain boundary proton conductivity is obtained at $x=0.2$, while the highest bulk conductivity exhibits at $x=0.1$. Several previously reported literatures ([18],[23]) showed the optimum doping concentration at 20 at.% BYZ for the bulk conductivity, which is higher than the result obtained in this study. The discrepancy could arise from the difference in the starting powders, fabrication procedures and EIS measurement conditions.

The grain boundary and total proton conductivity in this study of 20 at.% BYZ at 500°C are $2.84 \times 10^{-2} \text{ S/cm}$ and $1.22 \times 10^{-2} \text{ S/cm}$, respectively, whereas the bulk conductivity of 10 at.% exhibits $2.63 \times 10^{-2} \text{ S/cm}$ at 450°C .

Moreover, as x increases to 0.3, the bulk, grain boundary and total proton conductivities are substantially lowered. The decrease in the proton conductivity may arise primarily from the loss of BaO during the sintering process of BYZ. BaO evaporation could change the defect chemistry of the dopant substitution in BYZ. Fewer oxide ion vacancies may be created if Y substitutes a Ba site instead of a Zr site resulting in the lower number of incorporated water molecules and protons in BYZ samples as suggested by Zuo [40]. The bulk, grain boundary and total conductivities of all BYZ pellet samples at 350°C are compared and summarized in Fig 4.12.

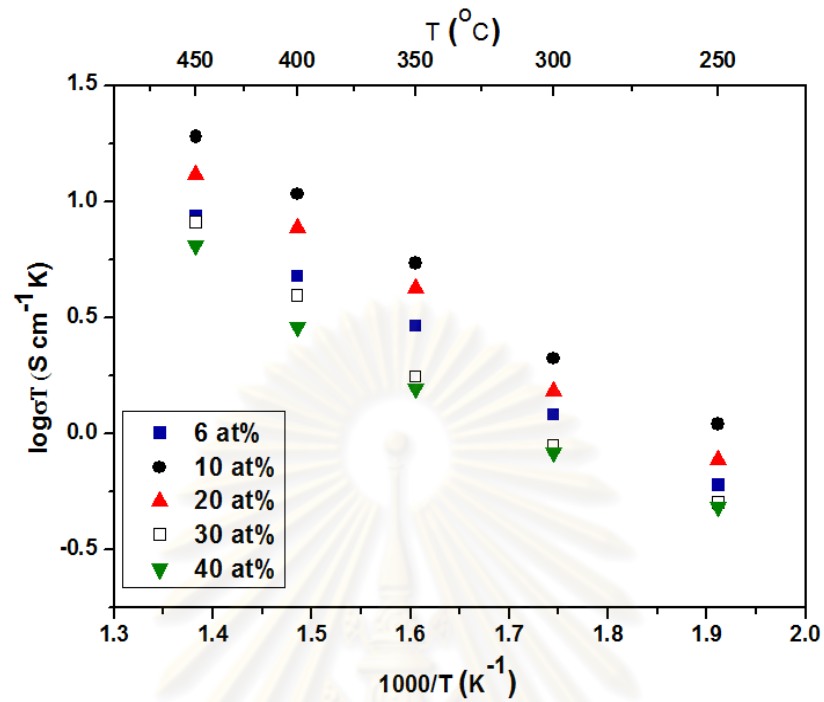


Figure 4.9: Bulk conductivities of BYZ pellet samples in air

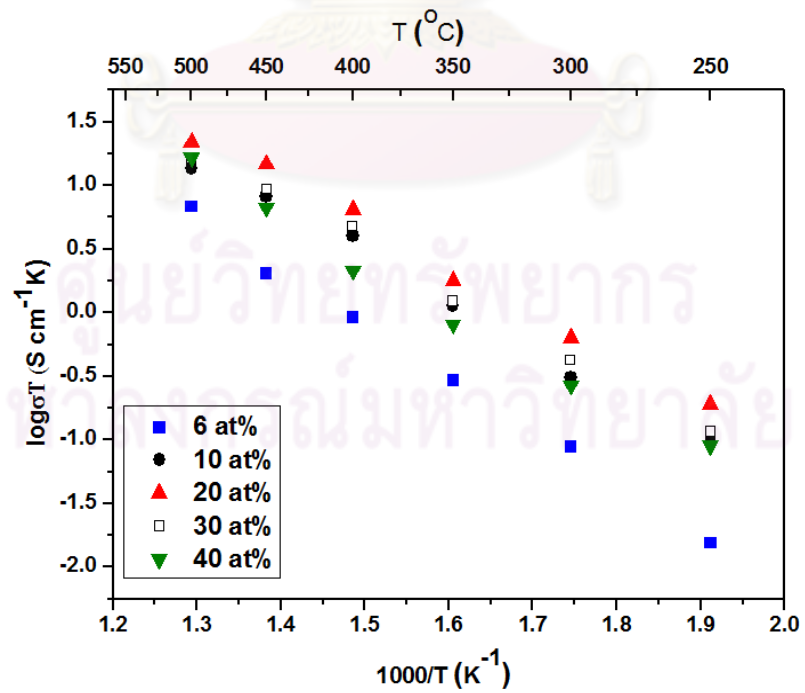


Figure 4.10: Grain boundary conductivities of BYZ pellet samples in air

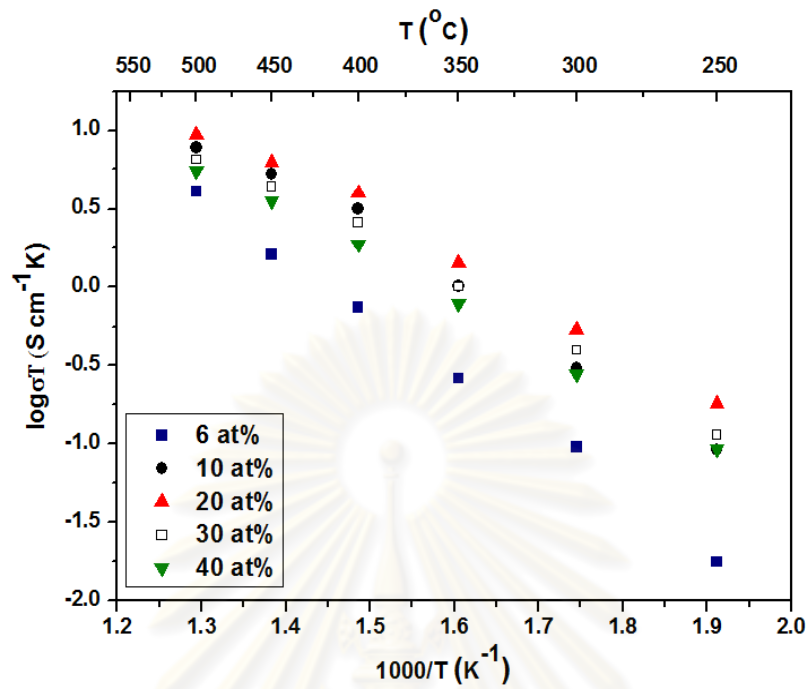


Figure 4.11: Total conductivities of BYZ pellet samples in air

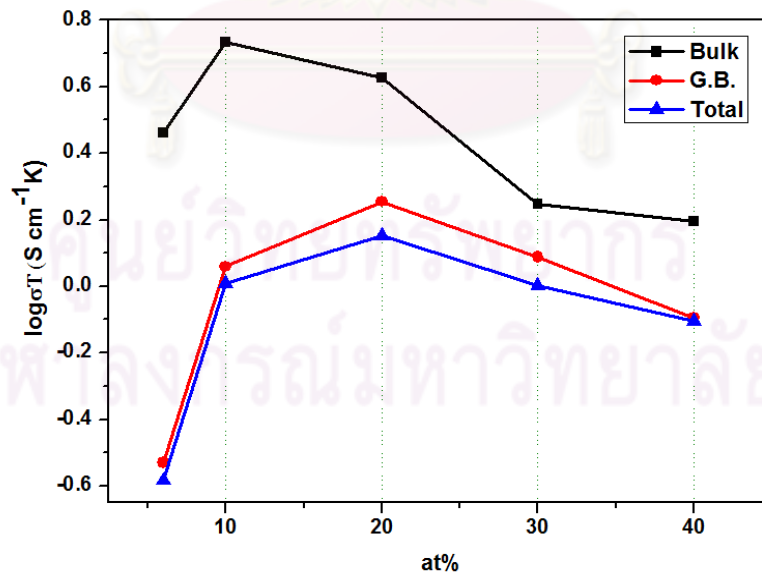


Figure 4.12: Bulk, grain boundary and total conductivities of BYZ pellet samples with different Y contents at 350°C in air .

The activation energies of the bulk proton conductivity at all Y doping concentrations are lower than that of grain boundary conductivity Table 4.3. The activation energy of the bulk proton conductivity is in the range of 0.42-0.47 eV, while that of the grain boundary proton conductivity is between 0.68-0.82 eV.

The lower values of grain boundary activation energies compared to those reported by Kosasang et al.[39] could arise from the reduction of secondary phase (Y_2O_3), the increase of grain size (Fig 4.6), and the higher density of BYZ pellet samples. Therefore, the use of nano- Y_2O_3 powder in the fabrication process could enhance the grain boundary conductivity and lower its activation energy.

Table 4.3: Bulk, grain boundary and total activation energies of nano- Y_2O_3 -BYZ pellets

Y content(at.%)	Bulk (eV)	G.B.(eV)	Total (eV)
6	0.44	0.82	0.69
10	0.47	0.72	0.64
20	0.47	0.68	0.59
30	0.45	0.71	0.56
40	0.42	0.72	0.58

4.4.4 The proton conductivities measured in different atmospheres

The EIS measurement on BYZ pellets were performed under the following atmospheres: air, dry H₂ (7% H₂ in Ar), and wet H₂ (7% H₂ in Ar). The results show that the conductivity of BYZ pellets increases in the following order: air, dry H₂ and wet H₂ (Fig 4.13). The proton conduction mechanism is highly dependent on the saturation of water in the structure and the amount of protons provided by the atmosphere [15]. In H₂ atmosphere, there are large amount of H atoms extracted from both H₂O and H₂, leading to higher number of protons available in the BYZ lattices. Therefore, the higher proton conductivity is observed in all samples measured in proton loading resource (H₂) than those measured in air.

The trend of the total proton conductivities of BYZ pellets measured in dry H₂ and wet H₂ are similar to those measured in air. The highest total proton conductivity was obtained at x=0.2, while the lowest was exhibits at x=0.06 throughout the temperature range of this study.

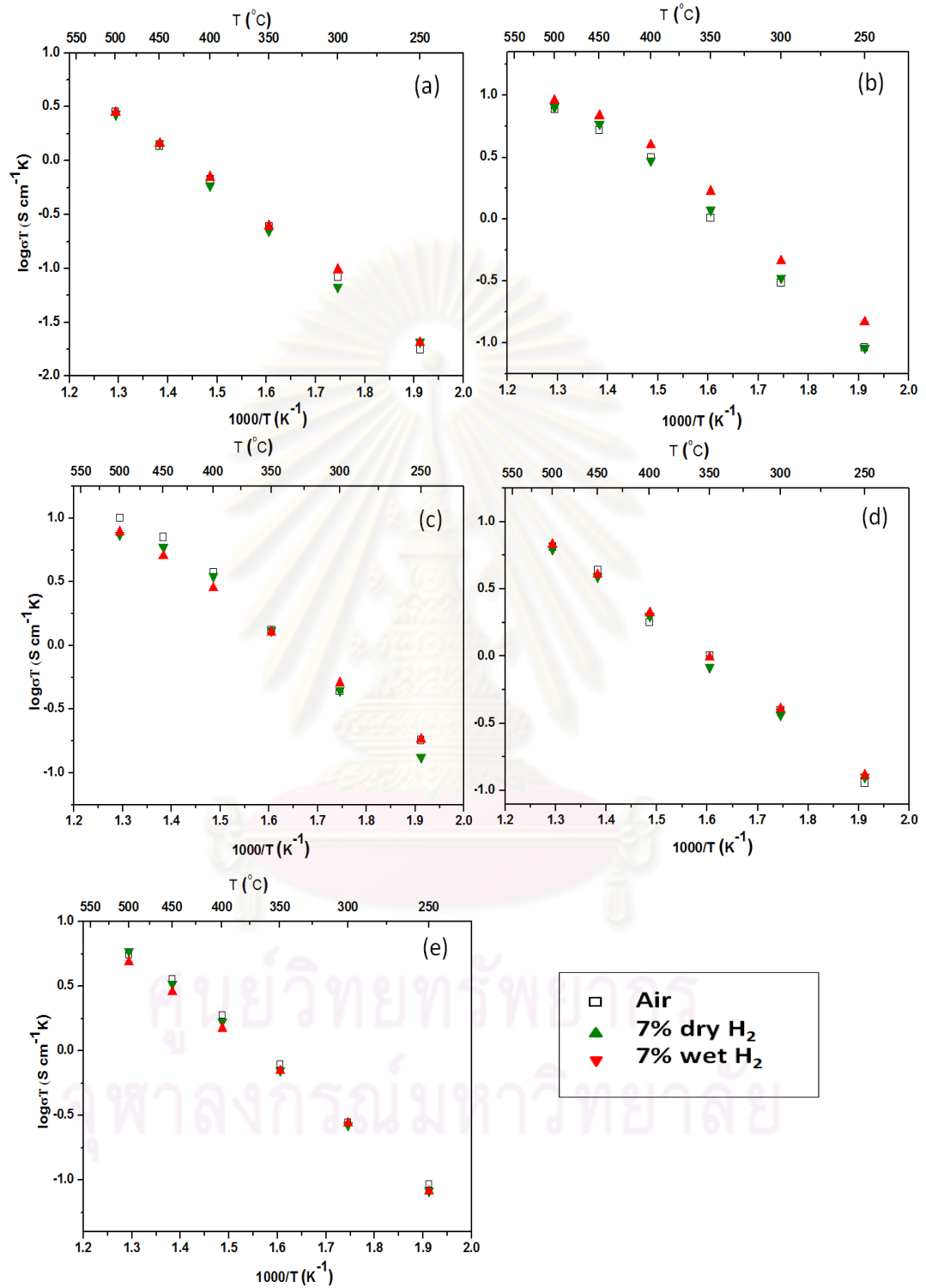


Figure 4.13: Total conductivities of BYZ pellet samples (a) 6 at.% (b) 10 at.% (c) 20 at.% (d) 30 at.% and (e) 40 at.% in different atmospheres

4.4.5 Dependence of BaO loss on the proton conductivities

The previously reported literatures [21]-[23] observed that the loss of BaO during sintering process had a significant impact on the reduction of proton conductivity of Y-doped BaZrO₃. Babilo et al. [21] showed that the barium deficiency lowered the conductivity of Y-doped BaZrO₃ by two orders of magnitude. Therefore, this work was performed to study the dependence of BaO loss on the proton conductivity of BYZ. The BYZ pellet sample were sintered in different conditions as followed:

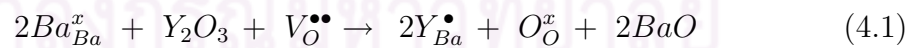
- ◇ (i) Covered-pellet:

The BYZ pellets were sintered in the BYZ-saturated system.

- ◇ (ii) Uncovered-pellet:

The BYZ pellets were sintered in air.

The comparison of total proton conductivity that was covered and uncovered during sintering are displayed in Fig 4.14. At x=0.06, the proton conductivities of covered pellets were obviously higher than that of uncovered. It was clear that Ba deficiency was show to lower the conductivity. The loss of BaO caused the incorporation of Y atoms into Ba sites. The possible defect reaction with Ba deficiency was shown in Eq. 4.1 [40].



However, when $x \geq 0.3$, the discrepancy between proton conductivities of covered and uncovered samples were reduced, which may arise from the BaO evaporation on surface.

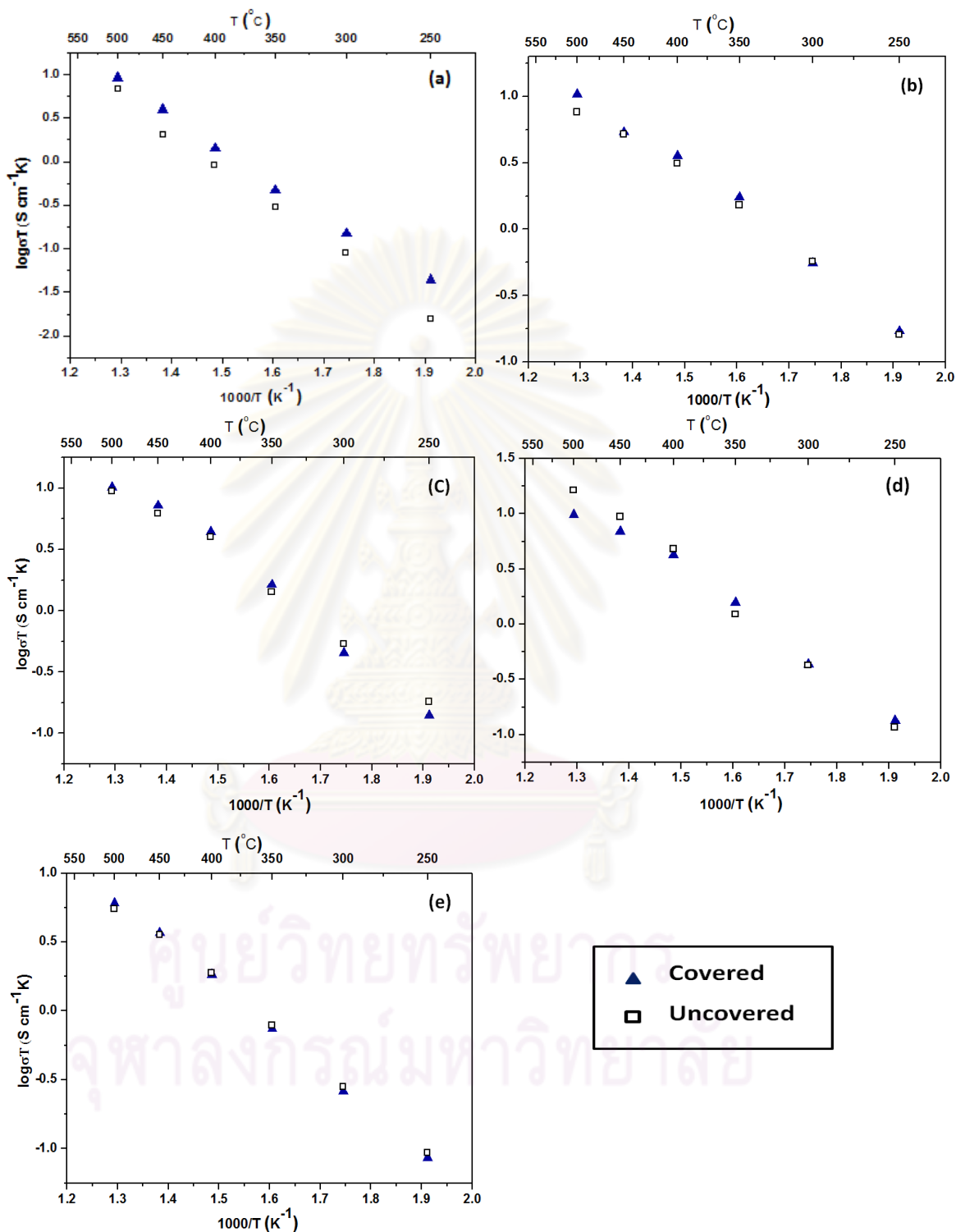


Figure 4.14: Total conductivities of BYZ pellet samples (a) 6 at.% (b) 10 at.% (c) 20 at.% (d) 30 at.% and (e) 40 at.% sintered in different atmospheres.

4.4.6 Comparison of the proton conductivity with the results from the previously reported literatures

The bulk and grain boundary conductivities of $\text{BaZr}_{0.8}\text{Y}_{0.2}\text{O}_{3-\delta}$ measured in air are summarized and plotted for a comparison with the results from the previously reported literatures [15, 22, 23, 38] in Fig 4.15.

The $\text{BaZr}_{0.8}\text{Y}_{0.2}\text{O}_{3-\delta}$ (BYZ20) bulk conductivity results from this study (Fig 4.15(a)) are in a very good agreement with Kreuer et al.'s [15]. The bulk conductivity are slightly lower than that of $\text{BaZr}_{0.85}\text{Y}_{0.15}\text{O}_{3-\delta}$ reported by Iguchi [38], whereas the grain boundary conductivity results are close to Iguchi et al.'s report as shown in Fig 4.15(b). Moreover, the bulk and grain boundary conductivities obtained in this study are much higher than $\text{BaZr}_{0.8}\text{Y}_{0.2}\text{O}_{3-\delta}$ and $\text{BaZr}_{0.85}\text{Y}_{0.15}\text{O}_{3-\delta}$ reported by Tao et al. [22] and Peng et al. [23]. The difference of the proton conductivities of each report could be related to the use of different starting powders, synthesis procedures, sintering parameters and EIS measurement conditions.

The bulk activation energies of $\text{BaZr}_{0.8}\text{Y}_{0.2}\text{O}_{3-\delta}$ (BYZ20) observed by Kreuer et al. [15] and $\text{BaZr}_{0.85}\text{Y}_{0.15}\text{O}_{3-\delta}$ (BYZ15) with 4 mol% ZnO addition by Babilo et al. [30] are 0.44 eV and 0.47 eV, respectively, which are in the same range as our results. Besides, our grain boundary activation energies of 0.68-0.82 eV also correspond very well to the report by Babilo et al. [30].

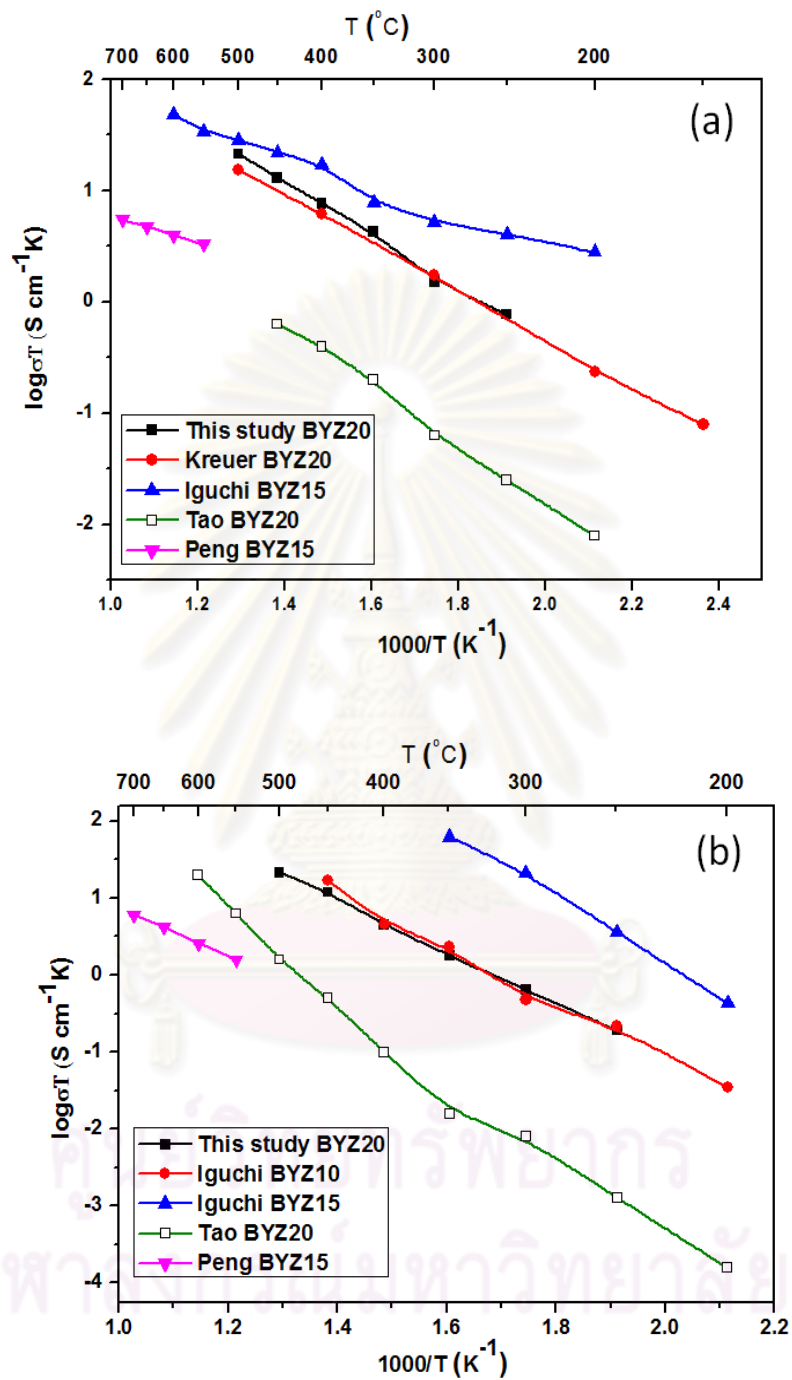


Figure 4.15: The comparison of our proton conductivities (a) bulk conductivity (b) grain boundary conductivity of $\text{BaZr}_{0.8}\text{Y}_{0.2}\text{O}_{3-\delta}$ to the previously reported literatures[15, 22, 23, 38]

CHAPTER V

RESULTS AND DISCUSSIONS: THIN FILMS

As discussed in Chapter 4, $\text{BaZr}_{0.8}\text{Y}_{0.2}\text{O}_{3-\delta}$ (BYZ20) pellet sample exhibits the highest total proton conductivity. The bulk proton conductivities of the pellet samples are higher than the grain boundary conductivity at all compositions. However, a large thickness of the electrolyte can reduce the fuel cell performance due to the ohmic loss discussed in Chapter 2. Therefore, to further decrease the overall electrolyte resistance to be comparable to that of Nafion[®], the thickness of the BYZ electrolyte must be reduced into thin film.

This chapter presents the physical properties and proton conductivities of BYZ thin films fabricated by (i) co-sputtering (M1) and (ii) 2-step sputtering (M2) methods. The proton conductivities of the BYZ thin films are then compared to the conductivities of the BYZ pellets.

5.1 XRD Patterns of BYZ Thin Films

5.1.1 BaZrO_3 thin films

The uniform BaZrO_3 thin films were deposited by the RF-sputtering technique at the substrate temperatures of room temperature up to 500°C. The XRD pattern of the as-deposited BaZrO_3 thin films with the substrate temperatures upto 400°C shows amorphous structures. However, as the substrate temperature reaches 500°C, the films become polycrystalline and exhibit the perovskite crystal structure of BaZrO_3 (JCPDS no. 00-006-0399) as shown in Fig 5.1.

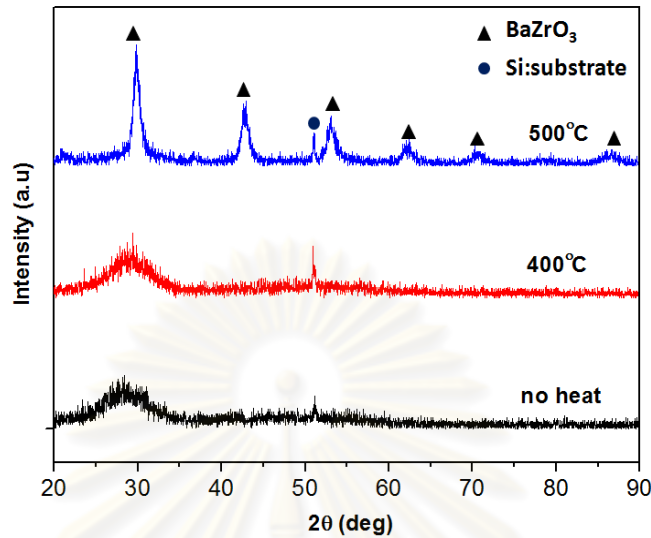


Figure 5.1: XRD patterns of BaZrO_3 films at the substrate temperatures of room temperature to 500°C .

5.1.2 Y-doped BaZrO_3 (BYZ) thin films

The XRD patterns of BYZ thin films fabricated by co-sputtering and 2-step sputtering techniques are presented in Fig 5.2(a) and Fig 5.2(b), respectively. As shown in Fig 5.2(a), the XRD patterns of the BYZ thin films obtained from the co-sputtering method (M1) of Y and BaZrO_3 targets correspond to the perovskite crystal structure of BaZrO_3 . The concentration of Y in the BYZ film is increased with the increasing DC power supplied to the Y target.

When the DC power applied on the Y target is greater than 5 W, yttria (Y_2O_3) segregation is observed, which suggests the saturation of Y and the depletion of Ba in the BYZ thin films. When the BYZ thin films are deposited by the 2-step sputtering (M2) method, the yttria stabilized zirconia (YSZ) phase appears as a secondary phase instead (Fig 5.2(b)), which could be caused by the Ba depletion during sputtering process as observed by Chen et al. [41].

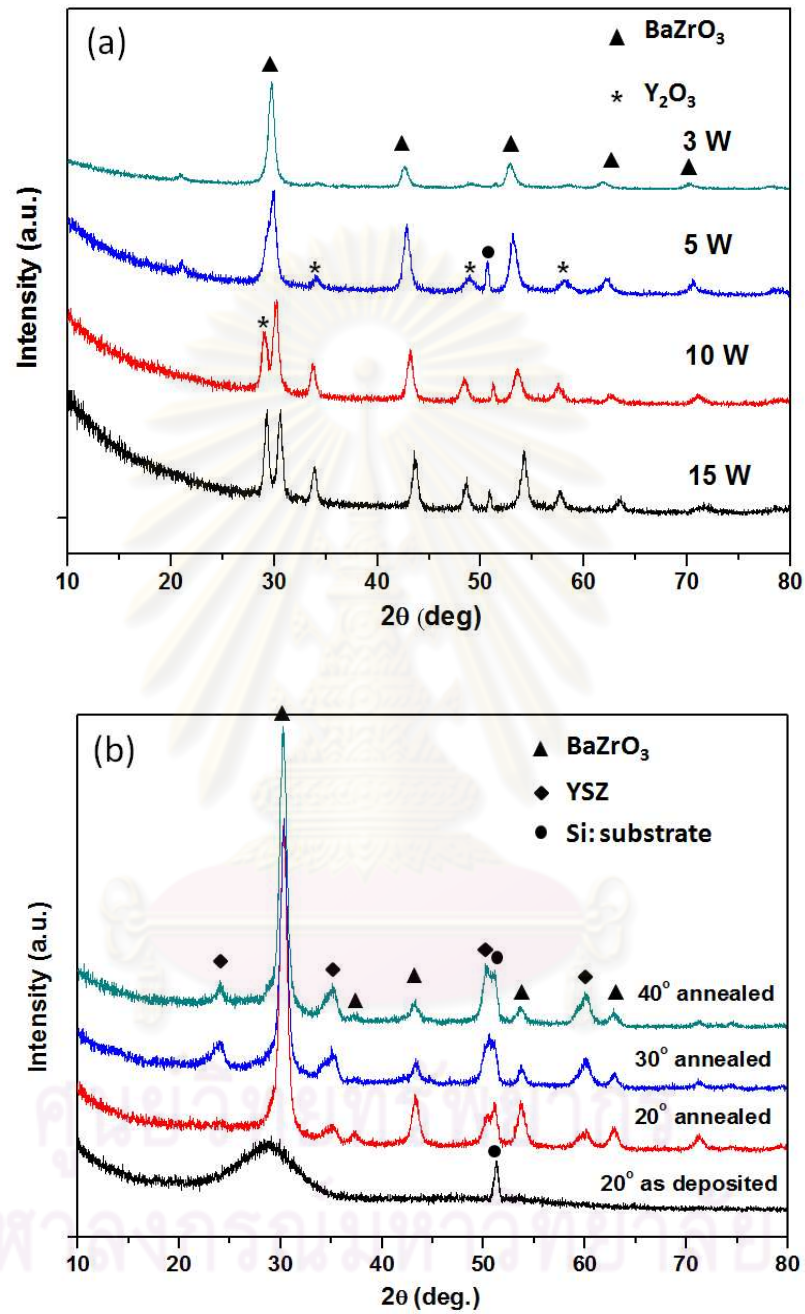


Figure 5.2: XRD patterns of Y-doped BaZrO₃ (BYZ) thin films

(a) Deposited by the co-sputtering technique at DC powers of 3-15W.

(b) Deposited by the 2-step sputtering technique at different Y-window angles of 20-40°.

The lattice parameter of the M1-BYZ thin films is expanded from 4.145 to 4.245 as the DC power reduces from 5W to 3W. However, the lattice parameters of the 10-Watt and 15-Watt BYZ thin films cannot be determined from the XRD result due to the overlay of the yttria and BYZ peaks. The lattice parameter of M2-BYZ thin films is expanded from 4.158 to 4.182 when the Y-window angle increased from 20° to 40°. As shown in Fig 5.3, the expansion of M2-BYZ thin film lattice parameter is similar to that of BYZ pellet samples, while that of M1-BYZ thin films are the highest among all samples.

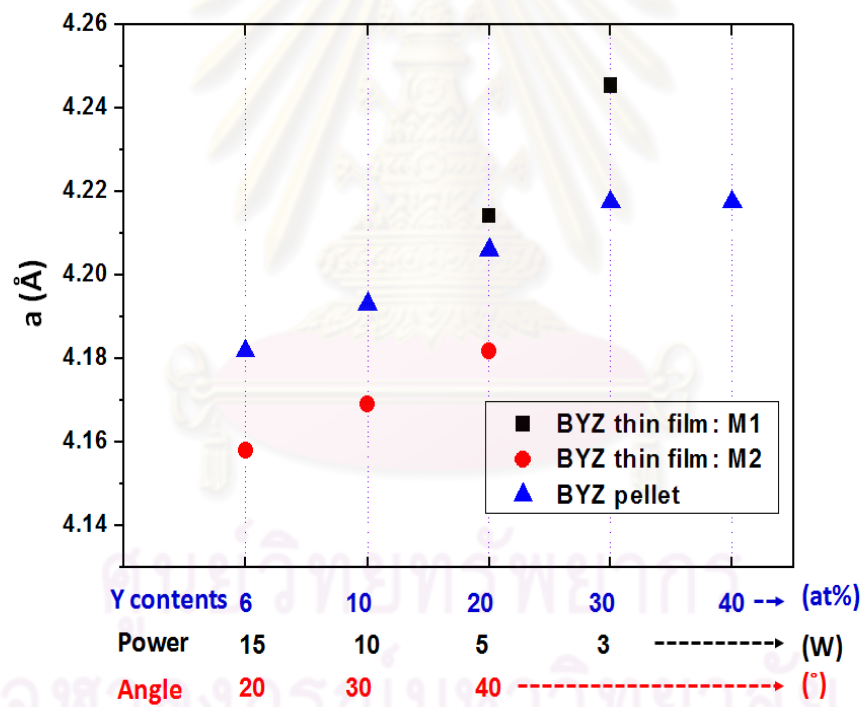


Figure 5.3: The lattice parameters of BYZ thin films deposited by co-sputtering (M1) and 2-step sputtering (M2) compared to those of pellets.

5.2 Microstructure of BYZ Thin Films

The microstructure of M1-BYZ and M2-BYZ thin films are presented in Fig 5.4 and Fig 5.5, respectively. The dense and uniform BYZ thin films consisting of nano-scale grain were obtained from both fabrication methods. However, the BYZ thin film surface deposited by the co-sputtering technique (Fig 5.4(a)) shows slightly larger grain size than that of the 2-step sputtering (Fig 5.5(a)), which may result from the higher substrate temperature during the deposition process.

The thickness of BYZ thin films by the co-sputtering technique are in a range of 130-140 nm, whereas those fabricated by the 2-step sputtering technique have the thickness varied from 163 to 214 nm as the Y-window angle increases from 20 to 40°.

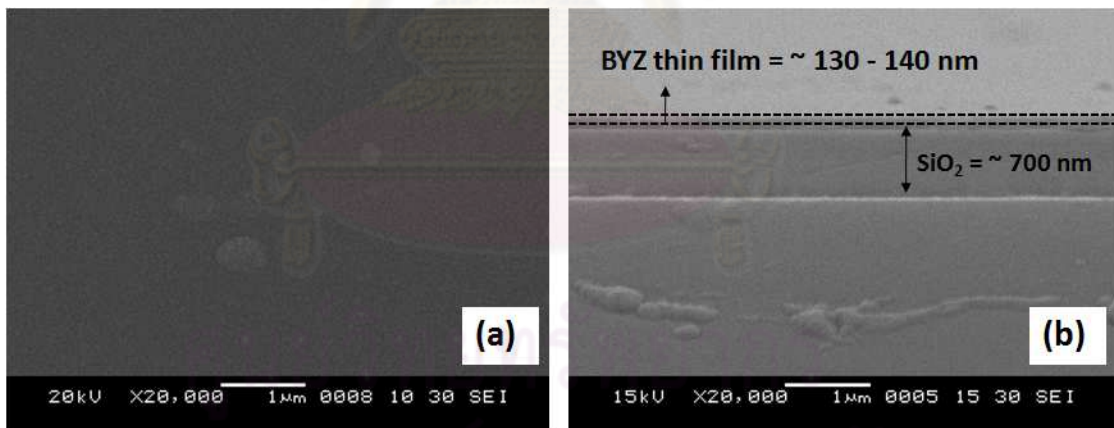


Figure 5.4: SEM images of (a) surface (b) the cross-sectional BYZ thin films fabricated by co-sputtering technique (M1)

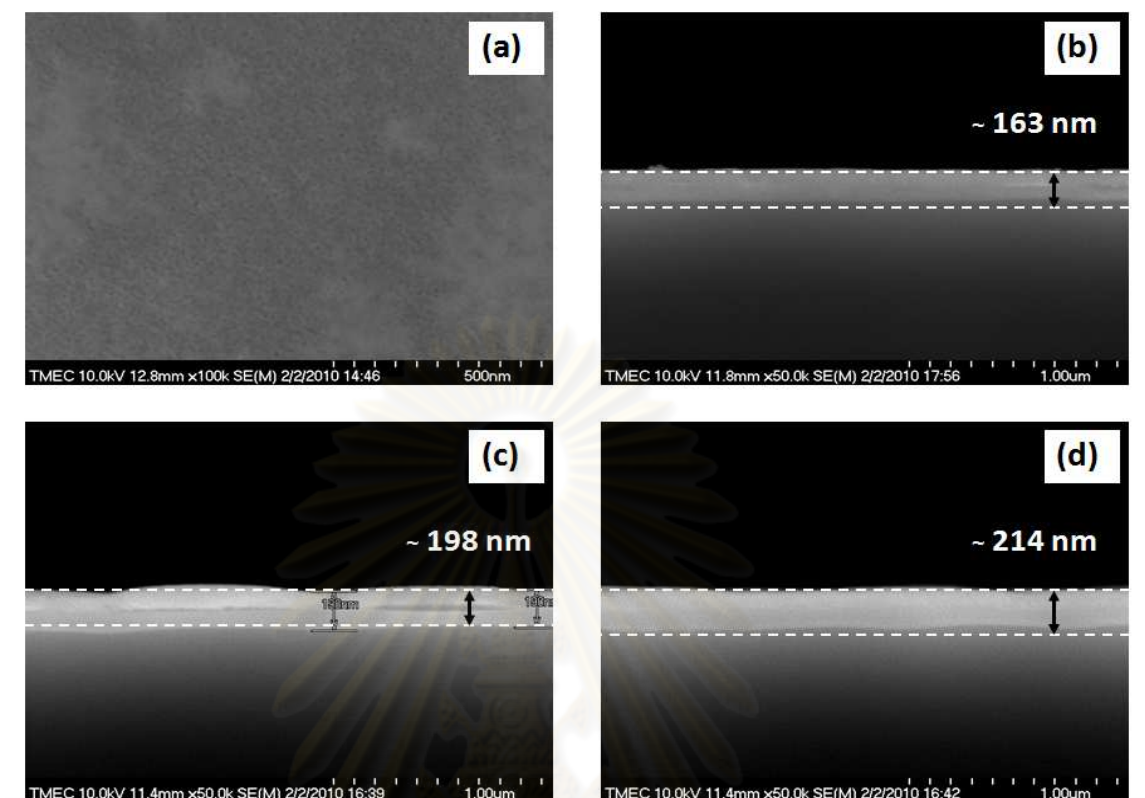


Figure 5.5: SEM images of BYZ thin films fabricated by the 2-step sputtering technique (M2) after annealing at 800°C: (a) surface (b) cross-section at an Y-window angle of 20° (c) cross-section at an Y-window angle of 30° (d) cross-section at an Y-window angle of 40°

ศูนย์วิทยทรัพยากร
จุฬาลงกรณ์มหาวิทยาลัย

5.3 Uniformity and Depth profiling of M1-BYZ Thin Films

The uniformity of the M1-BYZ thin films can be confirmed by the XPS depth profiles as shown in Fig 5.6. The XPS results reveal that the compositions of (Ba, Y, Zr and O) of the BYZ thin films remain constant throughout the entire thickness of the film. However, the XPS results also reveal that the M1-BYZ thin film compositions had very low Ba content which may be caused by several reasons: (i) the overlapping of Ba and Y binding energy peaks, which can extort Ba composition result (ii) the BaO loss at high temperature during the sputtering and annealing process as observed in the BYZ pellet and Babilo's report [30], (iii) the segregation of Y_2O_3 and YSZ phases and (iv) the resputtering on BYZ film during the sputtering process as suggested by Chen et al. [41].

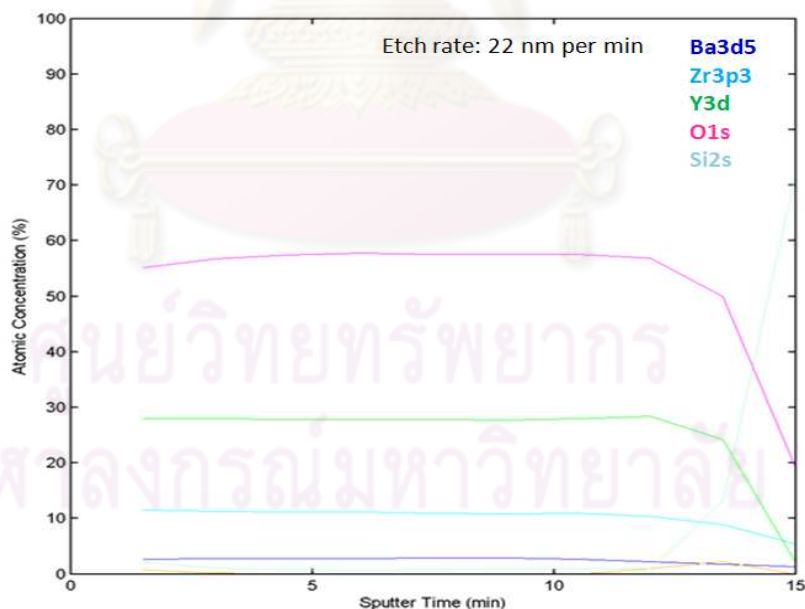


Figure 5.6: The XPS depth profile of M1-BYZ thin film with DC power 20 Watt

Moreover, as the DC power supplied on the Y target decreases, the shift of the Y3d and Zr3p³ binding energies are observed (Fig 5.7). When the DC power is less than 5W, the binding energy peaks of Y3d and Zr3p³ are increased, indicating that another oxidation state is formed in the M1-BYZ thin film. Contradict to the XPS results, XRD results show no secondary phase in 3W sample and the Y₂O₃ phase in 5W sample.

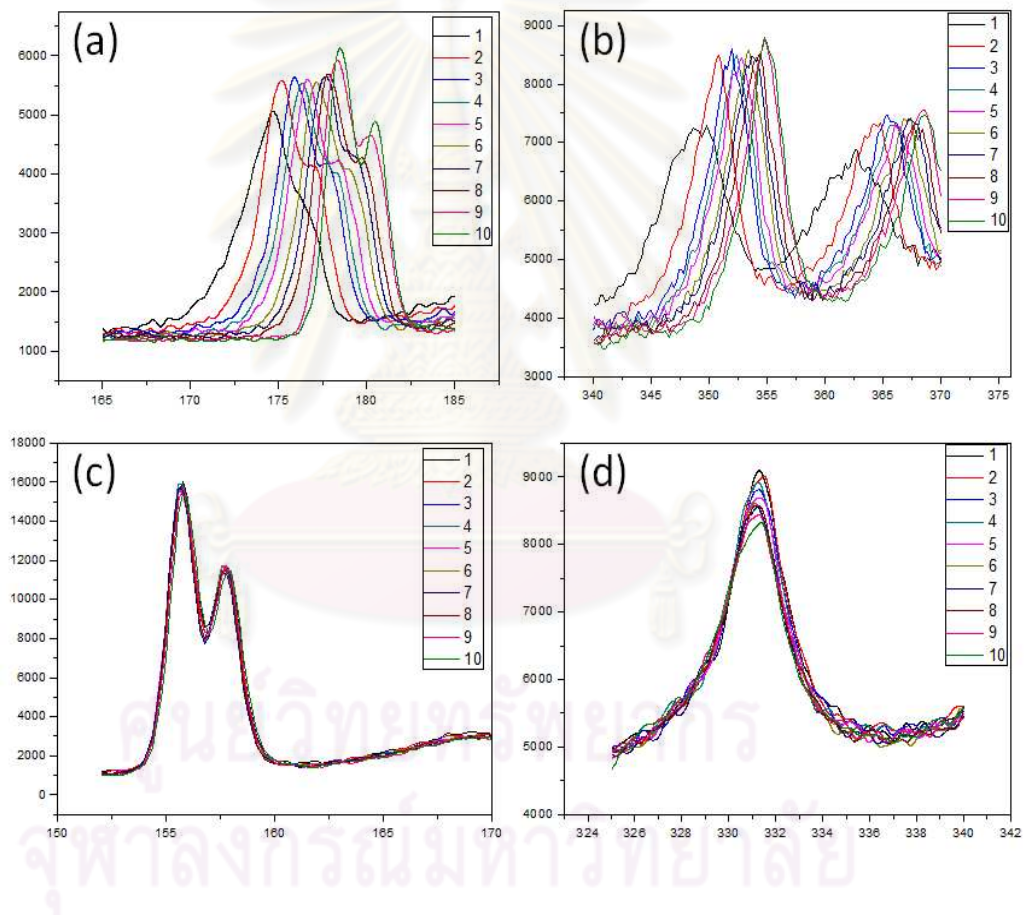


Figure 5.7: The plot of the intensity with respect to the binding energy of M1-BYZ thin films with different DC sputtering power on the Y target (a) Y3d:3W (b) Zr3p³:3W (c) Y3d:10W and (d) Zr3p³:10W

5.4 Proton Conductivity of BYZ Thin Films

5.4.1 The EIS result of M1-BYZ thin films in air

The conductivities of the M1-BYZ thin films with 3W, 5W and 10W DC sputtering power on the Y target are presented in Fig 5.8. The conductivities of the M1-BYZ thin films are divided into two distinct regions, which may be due to the two different ionic conduction mechanisms. At $T < 400^\circ\text{C}$, the activation energies of all M1-BYZ thin films are in a range of 0.46-0.52 eV, which is similar to the activation energy of the bulk proton conductivities in BYZ pellets (0.42-0.47 eV). Therefore, the conduction mechanism in this temperature range is likely the proton conduction mechanism. At $T > 400^\circ\text{C}$ the activation energies vary from 1.08 to 1.32 eV, which may correspond to the oxide ion conduction mechanism as suggested by Kreuer et al. [15] and Chen et al. [41].

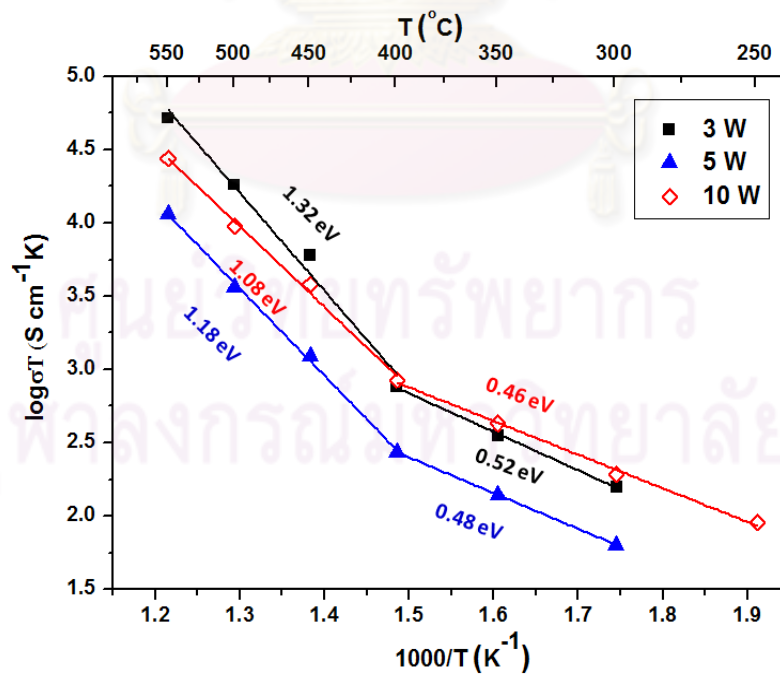


Figure 5.8: Conductivities of M1-BYZ thin films in air

5.4.2 The EIS result of M2-BYZ thin films in air

The conductivity of BYZ thin film deposited by the 2-step sputtering technique of 20,30 and 40° Y-window angles are shown in Fig 5.9. Similar to what observed in the M1-BYZ thin film results, the ionic conductivity are separated into two distinct regions. However, the transition temperature of the M2-BYZ thin films is at 450°C, which is higher than that of M1- BYZ thin films (400°C). At $T < 450^\circ\text{C}$, the activation energies of BYZ thin films are in a range of 0.48-0.59 eV, while At $>450^\circ\text{C}$, the activation energies are about 1.65-1.75 eV. The change in the activation energy are likely caused by the two ionic conduction mechanisms as mentioned in the previous section. The values of the total conductivity at all Y-window angles are very close to each other. The M2-BYZ thin film with 40° Y-window angle shows the highest proton conductivity at 400-550°C.

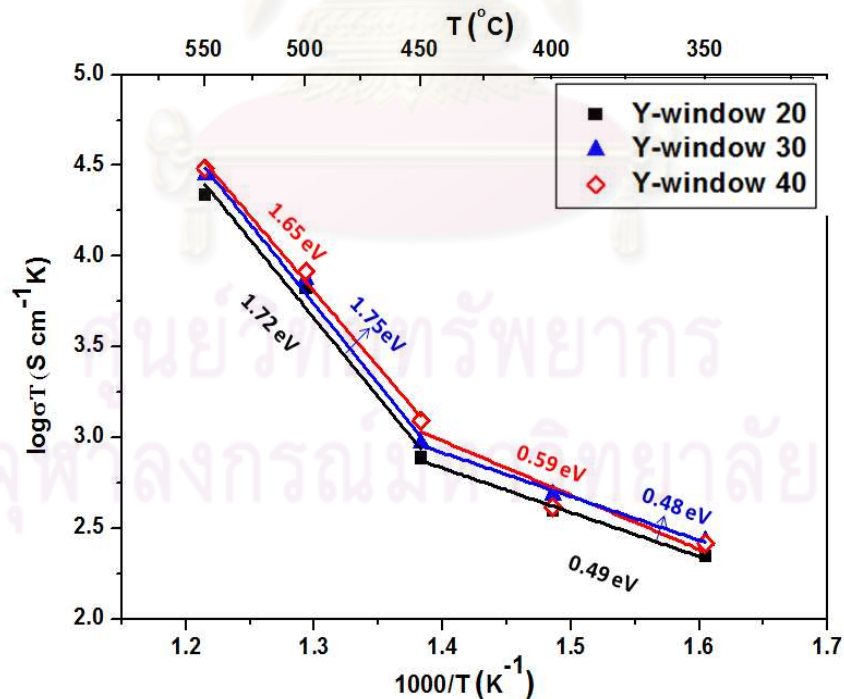


Figure 5.9: Conductivities of M2-BYZ thin films in air

5.4.3 Proton conductivities of M2-BYZ thin films in H₂

The EIS measurement on the M2-BYZ thin films were also performed under wet H₂ (7% H₂ in Ar) atmosphere. The results do not show the two separated regions of the conductivities as observed from the measurement in air (Fig 5.10). There is only one activation energy throughout the temperature range of this study.

The conductivities of M2-BYZ thin film with 20°, 30° and 40° Y-window angles in air and wet H₂ are compared in Fig 5.11. At T < 450°C, the conductivities of M2-BYZ thin films in wet H₂ are slightly higher than those measured in air. However, at T > 450°C, the proton conductivities of M2-BYZ thin film in wet H₂ are lower than the oxide ion conductivities in air.

The activation energies are in a range of 0.63-0.68 eV, which are close to the activation energy of BYZ pellet total proton conductivity (0.58 eV to 0.69 eV). As suggested by Kreure et al. [15], the proton conduction mechanism is highly dependent on the saturation of water and proton loading resource (H₂). There are large amount of H atoms extracted from both H₂O and H₂, leading to higher number of protons available in the BYZ lattices. Therefore, the higher proton conductivity is observed in all samples measured in wet H₂ than those measured in air. Furthermore, the proton conduction can overcome the oxide ion conduction at high temperature due to the higher number of protons and lower number of oxide ion vacancies from the water incorporation supplied by the wet H₂. As a result, only one activation energy of the conductivities, which is corresponding to the proton conduction, is observed.

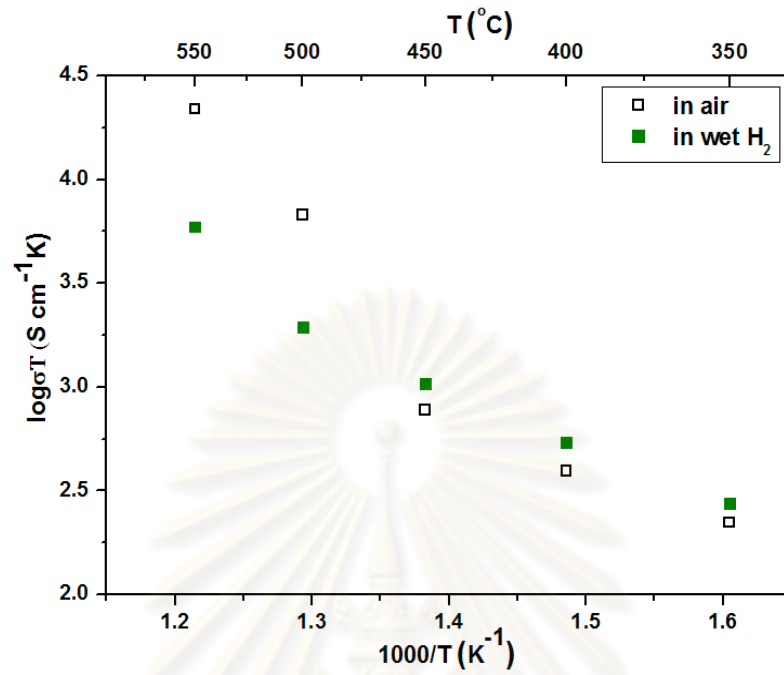


Figure 5.10: Conductivities of M2-BYZ thin film with 20 open angle in wet H₂

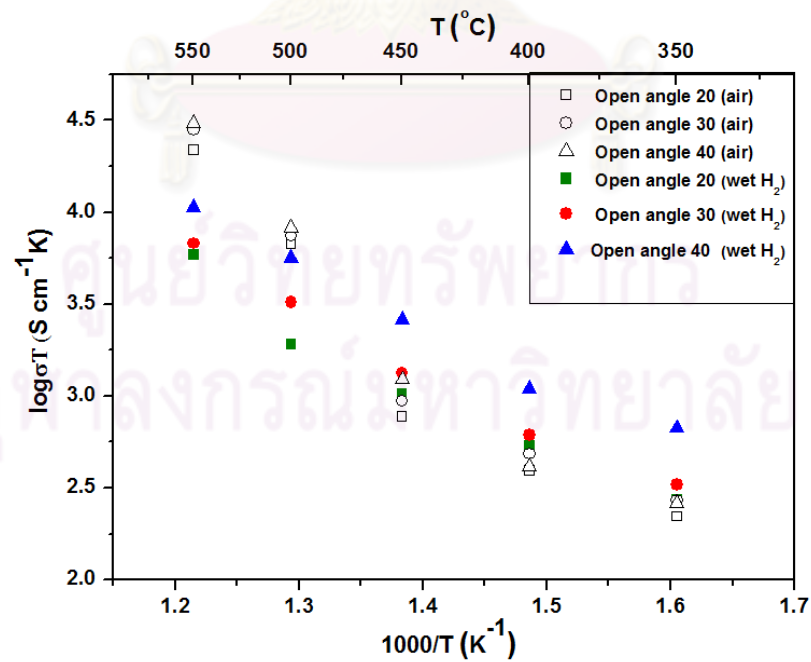


Figure 5.11: Total conductivities of M2-BYZ thin film in air and wet H₂

5.5 Comparison of the BYZ thin film conductivities to those of the BYZ pellets and the result from the previously reported literatures

As discussed in Chapter 4, the impedance spectra of BYZ pellets exhibit two semicircles, referred to the bulk and grain boundary resistance. The total resistance of the BYZ pellet was calculated using $R_{total} \doteq R_{bulk} + R_{G.B.}$. However, as shown in Fig 5.12, the impedance spectra of BYZ thin film shows only one elongated semicircle. The bulk and grain boundary resistance of the BYZ thin film cannot be clearly distinguished. Therefore, only total resistance of the BYZ thin film was extracted from the EIS results.

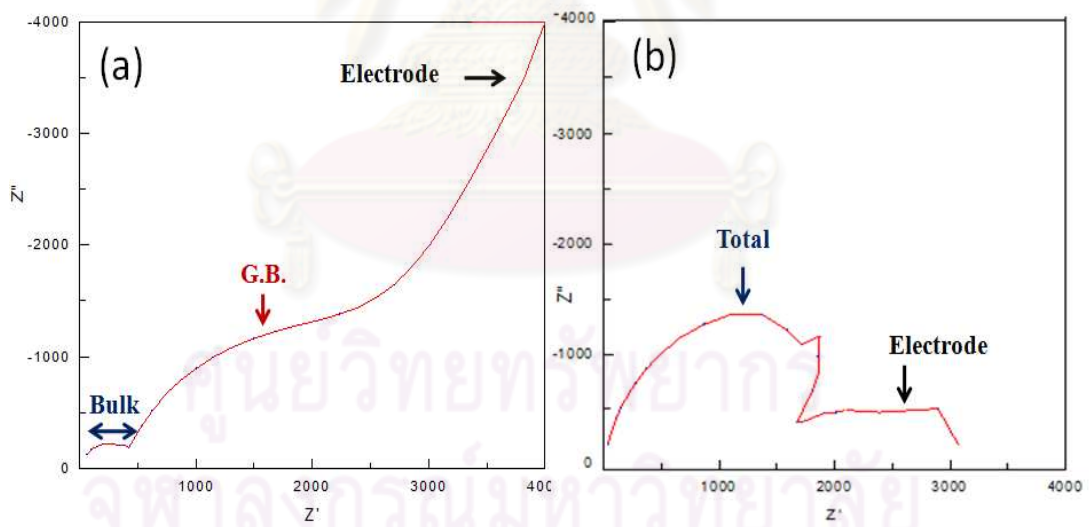


Figure 5.12: The impedance spectra of (a) pellet (b) thin film

The total conductivity of M1-BYZ, M2-BYZ thin films and BYZ pellets are compared in Fig 5.13. The total conductivities of M1-BYZ and M2-BYZ thin films are about 100 times higher than those of the BYZ pellets. The proton activation energies of both M1-BYZ and M2-BYZ thin films are in the same range as the bulk conductivities of the BYZ pellets.

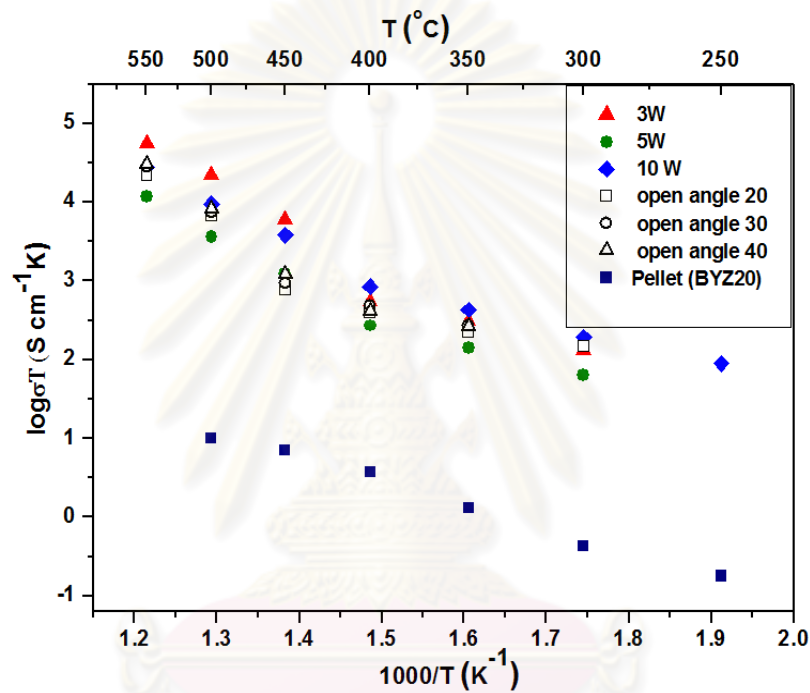


Figure 5.13: Conductivities of BYZ thin film compared to those of BYZ pellets

The BYZ thin film conductivities are plotted for comparison with those of BYZ pellets and the BYZ pellet results from previous reports [15, 38] in Fig 5.14. The conductivity of BYZ thin films are higher than those from the previous reports. The differences in microstructure, ionic conduction mechanisms and impurities could be possible contribution to the high conductivity observed in this study. Since BYZ thin film fabricated by sputtering technique has low impurities, the blocking resistance on the grain boundary is subsequently decreased. As a result,

the high conductivity on BYZ thin film is observed. A surface conduction of BYZ thin films could have a possible effect on the high conductivity in this study because there are higher number of proton available on the surfaces and the surface may be a faster diffusion pathways than bulks. However, the activation energy is higher than the bulk activation energy of Kreuer [15] and Iguchi [38] reports, which may caused by the reasons mentioned above.

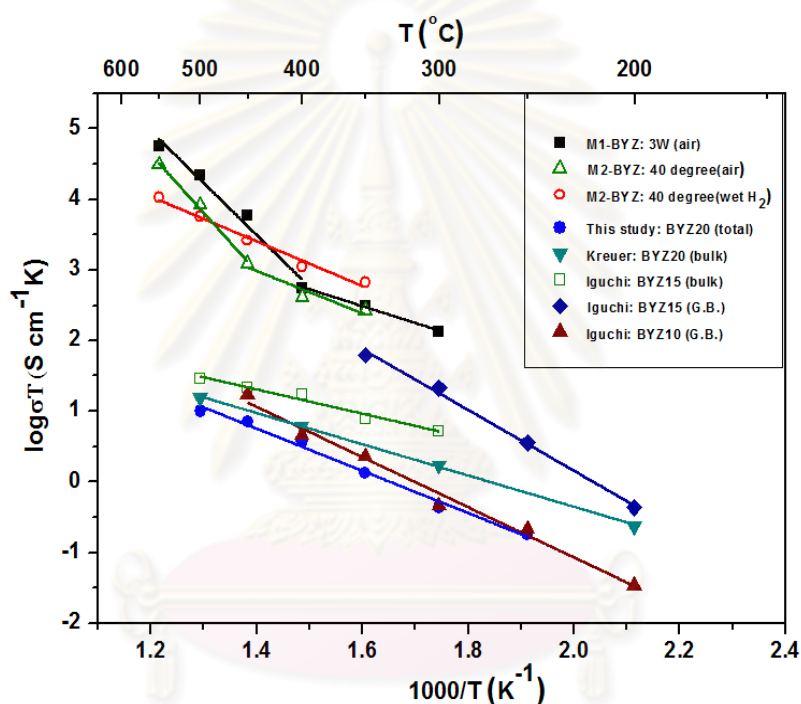


Figure 5.14: The comparison of the proton conductivities of M1-BYZ and M2-BYZ thin films to the results from the previously reported literatures and BYZ pellets from this study.

CHAPTER VI

CONCLUSIONS and FUTURE WORKS

6.1 Conclusions

$\text{BaZr}_{1-x}\text{Y}_x\text{O}_{3-\delta}$ (with 1wt% ZnO addition) pellet samples with $x = 0.06, 0.1, 0.2, 0.3$ and 0.4 were fabricated by mean of solid state reactions. The influence of micro- Y_2O_3 and nano- Y_2O_3 powders on the BYZ physical properties was studied. The XRD results reveal that the micro- Y_2O_3 -BYZ and nano- Y_2O_3 -BYZ pellet samples match with the perovskite structures. In micro- Y_2O_3 -BYZ, the secondary phase (Y_2O_3) was observed when $x \geq 0.3$, due to the incomplete solid state reaction. However, once Y_2O_3 micro-powder was replaced by Y_2O_3 nano-powder, the secondary phase was no longer observed. The density of micro- Y_2O_3 -BYZ samples, when $x < 0.4$ reached $\sim 95\%$. However, the density declined to 83% when $x = 0.4$ which was likely caused by the secondary phase due to large Y_2O_3 particle size in the starting powder. The density of nano- Y_2O_3 -BYZ samples reached over 97% and no declined in the density of the sample was observed with increasing Y content.

The conductivity of the pellet samples was measured by EIS under air, dry H_2 (7% H_2 in Ar) and wet H_2 (7% H_2 in Ar) atmospheres. The EIS measurements in air showed the optimum concentrations for bulk and grain boundary conductivities at 10 at.% and 20 at.%, respectively. The activation energy of the bulk proton conductivity was in the range of 0.42-0.47 eV, while the grain boundary proton conductivity was between 0.68-0.82 eV. The 20 at.% BYZ pellet sample

exhibited the highest total proton conductivity throughout the temperature range of 250-500°C in all atmospheres. By comparing the EIS results under the different atmospheres, the highest conductivity was observed in the wet H₂ environment, thus confirms the proton conduction mechanism.

The M1-BYZ thin films were obtained by the co-sputtering technique on the Y and BaZrO₃ targets under the DC and RF power supplies, respectively. During the co-sputtering, the substrate temperature was set to 700°C to obtain dense and polycrystalline BYZ thin films. The Y₂O₃ segregation was clearly observed as DC applied power on the Y target higher than 5W. The total conductivities of M1-BYZ thin films were divided into two distinct regions, which may be due to the two different ionic conduction mechanisms. The activation energies were in the range of 0.46-0.52 eV and 1.08-1.32 eV, which were corresponding to the proton conduction and oxide ion conduction mechanisms, respectively.

The M2-BYZ thin films were obtained by the 2-step sputtering technique. The process was modified by the DC sputtering of yttrium metal at Y-window angles of 20°, 30° and 40° on the surface of BaZrO₃ target to obtain the BYZ target. The thin films of BYZ were subsequently deposited by RF sputtering technique on the Si substrates. After the sputtering process, the M2-BYZ thin films were annealed at 800°C in air for 3h to form the polycrystalline films. The XRD analysis showed the YSZ and perovskite phase of BaZrO₃ in all samples. The amount of YSZ phase separation increased with the increasing Y-window angles. The conductivities of M2-BYZ thin films were higher than those of the pellet samples but were slightly less than that of M1-BYZ thin films. The proton conduction had the activation energies in range of 0.48-0.59 eV, while the activation energies of the oxide ion conduction were between 1.65-1.75 eV, close to that of the M1-BYZ thin films.

The EIS measurements on the M1-BYZ and M2-BYZ thin film surfaces revealed the high conductivity of 100 times those of the pellet samples. The discrepancy of the conductivity between BYZ pellet and thin films may be caused by the difference of the microstructure, ionic conduction mechanism and impurities.

6.2 Future Works

1. To ensure that no Y metal left in the BYZ thin films, the oxygen gas should be flown into the chamber during the co-sputtering process.
2. To eliminate the contribution of the surface conduction, the EIS measurement across the thin film thickness should be performed.
3. The complete DEFC single cell , consisting of the anode, cathode and electrolyte, should be fabricated using the thin film deposition technique, and the single cell will be test to investigate for the performance of the DEFC using BYZ thin film as the electrolyte.

ศูนย์วิทยทรัพยากร
จุฬาลงกรณ์มหาวิทยาลัย

REFERENCES

- [1] R. Pornprasertsuk. *Ionic conductivity studies of solid oxide fuel cell electrolytes and theoretical modeling of an entire solid oxide fuel cell*. Doctoral dissertation, Department of Materials Science and Engineering, Stanford University, 2007.
- [2] S. Douvartzides, F. Coutelieris and P. Tsiakaras. Exergy analysis of a solid oxide fuel cell power plant fed by either ethanol or methane. *Journal of Power Sources* 131 (2004): 224-230.
- [3] S. Song, W. Yi and S. peikang . Thermodynamic and kinetic considerations for ethanol electrooxidation in direct ethanol fuel cell. *Chinese Journal of Catalyst* 28,9 (2007): 752-754.
- [4] H. Iwahara, H. Uchida and N. Maeda. Studies on solid electrolyte gas cell with high-temperature-type proton conductor and oxide ion conductor. *Solid State Ionics* 11 (1983): 109-115
- [5] T. Yajima and H. Iwahara. Protonic and oxide ionic conduction in BaCeO₃-based-ceramics: effect of partial substitution for Ba in BaCeNd_{0.2}O_{3- α} with Ca. *Solid State Ionics* 47 (1991): 117-124.
- [6] K.D. Kruer. Proton-conducting oxides. *Annual Review of Material Research* 33 (2003): 333-359.
- [7] R. O'Hayre, S.W. Cha, W. Collella and F.B. Prinz. *Fuel Cell Fundamentals*. USA: John Wiley& Son, 2006.
- [8] T. Mathuveeran, K. Roelofs, D. Senftleben and T. Schiestel. Proton conducting composite membranes with low ethanol crossover of DEFC. *Desalination* 200 (2006): 662-663.
- [9] S. Song and P. Tsiakaras. Recent progress in direct ethanol proton exchange membrane fuel cell (DE-PEMECs). *Applied Catalysis: Environmental* **63** (2006): 187-193.
- [10] B. Todd. *Current voltage characteristics of SOFCs*. [online] 2003
Available from: http://www.fuelcellknowledge.org/research_and_analysis/cell_performance/iv_characteristics/iv_characteristic_of_softc.pdf [2009, June 20]
- [11] H. Iwahara, T. Esaka, H. Uchida and N. Maeda . Proton conduction in sintered oxides and its application to steam electrolysis for hydrogen production. *Solid State Ionics* 3,4 (1981): 359-363.
- [12] K.D. Kreuer . Aspect of the formation and mobility of protonic charge carrier and the stability of perovskite-type oxides. *Solid State Ionics* 125 (1999): 285-302.

- [13] D. William and J.R. Callister. *Materials Science and Engineering: An Introduction*. 5th edition, USA: John Wiley & Son, 2002.
- [14] F.M.M. Snijkers, A. Buekenhoudt, J. Coymans and J.J. Luyten. Proton conducting and phase composition in $\text{BaZr}_{0.9}\text{Y}_{0.1}\text{O}_{3-\delta}$. *Scripta Materialia* 50 (2004): 655-659
- [15] K.D. Kruer, St. Adam, W. Münch, A. Funchs, U. Klock and J. Maier . Proton conducting alkaline earth zirconates and titanates for high drain electrochemical applications. *Solid State Ionics* 145 (2001): 295-306.
- [16] Y. Yamazaki, P. Babilo and S.M. Haile. Defect chemistry of yttrium-doped barium zirconate: A thermodynamic analysis of water uptake. *American Chemical Society* 20 (2008): 6352-6357.
- [17] H. Iwahara, T. Yajima, T. Hibino, K. Ozaki and H. Suzuki. Proton conduction in calcium, strontium and barium zirconates. *Solid State Ionics* 61 (1993): 65-69.
- [18] F. Iguchi, N. Sata, T. Tsurui and H. Yugami. Microstructure and grain boundary of $\text{BaZr}_{1-x}\text{Y}_x\text{O}_{3-\delta}$ ($x = 0.05, 0.10, 0.15$) ceramics. *Solid State Ionics* 178 (2007): 691-695.
- [19] R.B. Cervara, Y. Oyama, S. Miyoshi and K. Kobayashi. Structural study and proton transport of bulk nanograined Y-doped BaZrO_3 oxide protonic materials. *Solid State Ionics* 179 (2008): 236-242.
- [20] C. Pascual, P. Duran. Subsolidus Phase Equilibria and Ordering in the System $\text{Zr}_2\text{-Y}_2\text{O}_3$. *Journal of the American Ceramic Society* 66,1 (1983): 23-27.
- [21] P. Babilo, T. Uda and S.M. Haile. Processing of yttrium-doped barium zirconate for high proton conductivity. *Journal of Materials Research* 22,5 (2007): 1322-1330.
- [22] S. Tao and J.T.S. Irvine. Conductivity studies of dense yttrium-doped BaZrO_3 sintered at 1325°C . *Journal of Solid State Chemistry* 180 (2007): 3493-3503.
- [23] C. Peng, J. Melnik, J. Li, J. Luo, A.R. Sanger and K.T. Chuang. ZnO-doped $\text{BaZr}_{0.85}\text{Y}_{0.15}\text{O}_{3-\delta}$ proton-conducting electrolytes: Characterization and fabrication of thin films. *Journal of Power Sources* 190 (2009): 447-452.
- [24] M. Ohring *Materials Science of Thin Films*. 2nd edition, USA: A Division of Harcourt, 2002.
- [25] D. Beckel, A.B.Hütter, A. Harvey, A. Infortuna, U.P. Muecke, M. Prestate, J.L.M. Rubb and L.J. Gaukler. Thin films for micro solid oxide fuel cells. *Journal of Power Sources* 173 (2007): 325-345.

- [26] T.M. Christensen. *Physics of thin films*. [online] 2000 Available from: www.uccs.edu/~tchrste/courses/PHYS549/549lectures/sputtertech.html. [2009 June 30]
- [27] H. Liu, and D.S. Dandy. Studies on nucleation process in diamond CVD: an overview of recent developments. *Diamond and Related Materials* 4 (1995): 1173-1188.
- [28] B. Robertz, A. Rulmont, B. Gilbert, R. Cloots, M. Ausloss and N. Leroy. Inhibition of macrocrack formation in zirconia substrate by barium zirconate formation. *Materials Letters* 41 (1999): 273-277.
- [29] D. Satas, A.A. Tracton. *Coating Technology Handbook*. 2nd edition, USA: Marcel- Dekker, 2001.
- [30] P. Babilo and S.M. Haile. Enhanced sintering of yttrium-doped barium zirconate by addition of ZnO. *Journal of the American Ceramic Society* 88,9 (2005): 2362-2368.
- [31] M.W. Barsoum. *Fundamental of Ceramics*. Singapore: The McGraw-Hill, 1997.
- [32] D.A. Skoog and J.J. Leary. *Principles of Instrumental Analysis*. 4th edition, USA: Perkin-Elmer, 1992.
- [33] N.D. Cogger and N.J. Evan. *Technical Report: An Introduction to Electrochemical Impedance Measurement*. USA: John Wiley & Son, 1999.
- [34] J. Bauerle. Study of solid electrolyte polarization by a complex admittance method. *Journal of Physics and Chemistry of Solids* 30 (1969): 2657-2670.
- [35] Gamry instrument. *Basic of electrochemical impedance spectroscopy* [online] 2007. Available from: www.gamry.com/App_Notes/Index.htm. [2009, July 13]
- [36] K. Nomura and H. Kogeyama. Transport properties of Ba(Zr_{0.8}Y_{0.2})O_{3-δ} perovskite. *Solid State Ionics* 178 (2007): 661-665.
- [37] D. Shima and S.M. Haile. The influence of cation non-stoichiometry on the properties of undoped and gadolinia- doped cerate. *Solid State Ionics* 97 (1997): 443-455.
- [38] F. Iguchi, T. Tsuru, N. Sata, Y. Nagao and H. Yugami. The relationship between chemical composition distribution and specific grain boundary conductivity in Y-doped BaZrO₃ proton conductor. *Solid State Ionics* 180 (2009): 563-568.
- [39] O. Kosasang, K. Somroop, P. Chindaudom and R. Pornprasertsuk. Effect of doping concentration on the proton conductivity of Y-doped BaZrO₃ thin films. *ECS Transactions* 19,27 (2009): 145-151.

- [40] C. Zuo. *Doping and defect structure of mixed-conducting ceramics for gas separation*. Doctoral dissertation, Department of Materials Science and Engineering, Georgia Institute of Technology, 2006.
- [41] X.X. Chen, L. Rieth, M.S. Miller and F. Solzbacher. High temperature humidity sensors based on sputtered Y-doped BaZrO₃ thin films. *Sensors and Actuators B: Chemical* 137 (2009): 578-585.



ศูนย์วิทยทรัพยากร
จุฬาลงกรณ์มหาวิทยาลัย



APPENDICES

ศูนย์วิทยทรัพยากร
จุฬาลงกรณ์มหาวิทยาลัย

APPENDIX A

Particle Size Distribution (PSD)

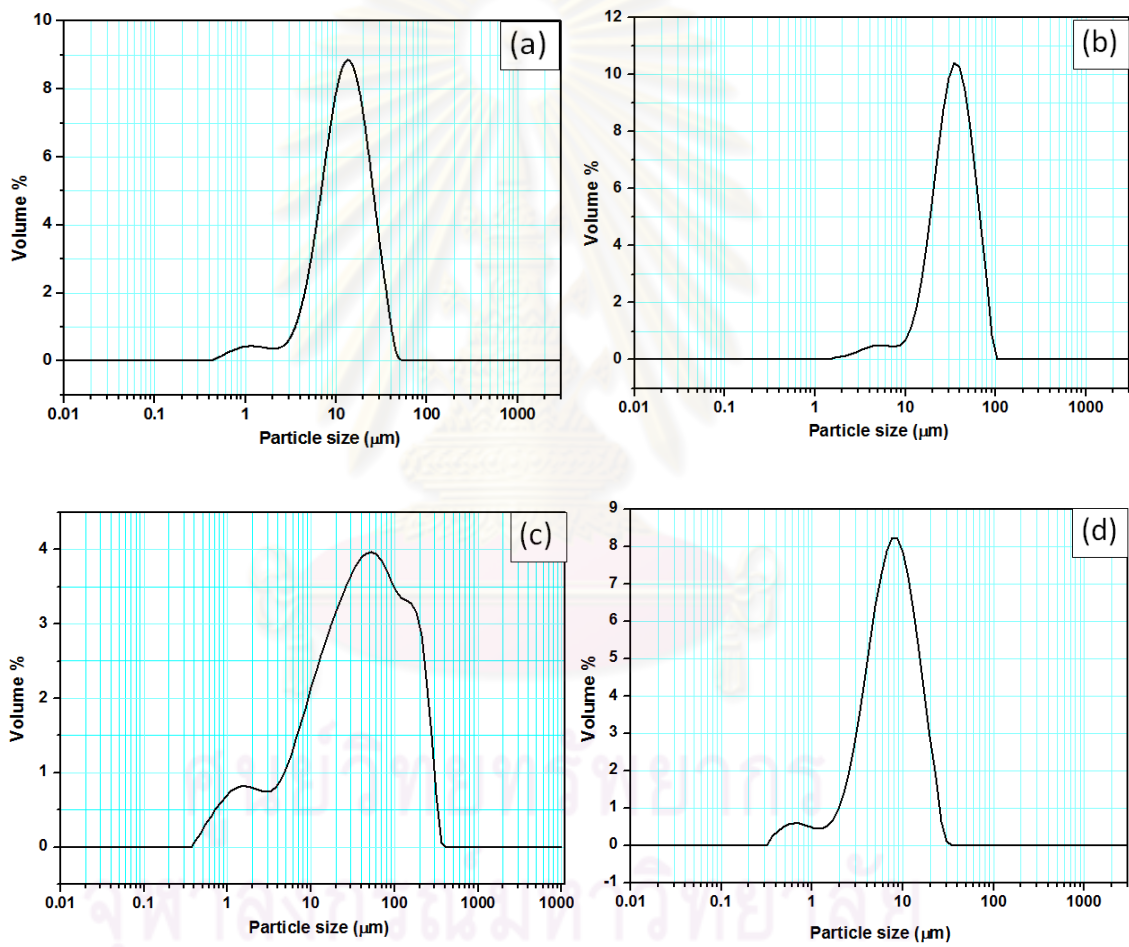


Figure A.1: The particle sizes distribution of raw materials (a) BaCO₃ (b) 3 mol% Ytria Stabilized Zirconia (c) micro-Y₂O₃ (d) nano-Y₂O₃ powders

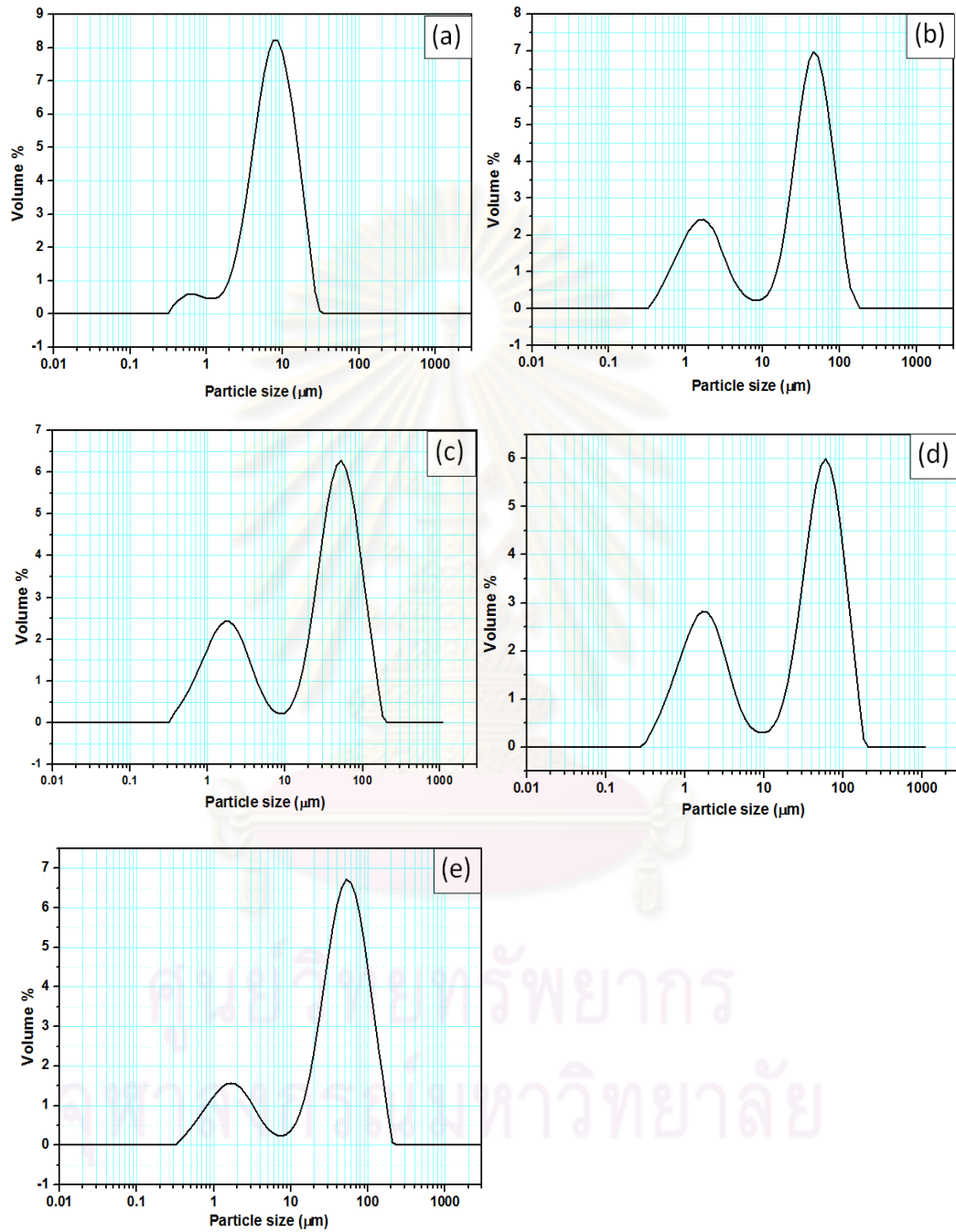


Figure A.2: The particle size distribution of micro-Y₂O₃-BYZ (a) 6 at.% (b) 10 at.% (c) 20 at.% (d) 30 at.% (e) 40 at.%

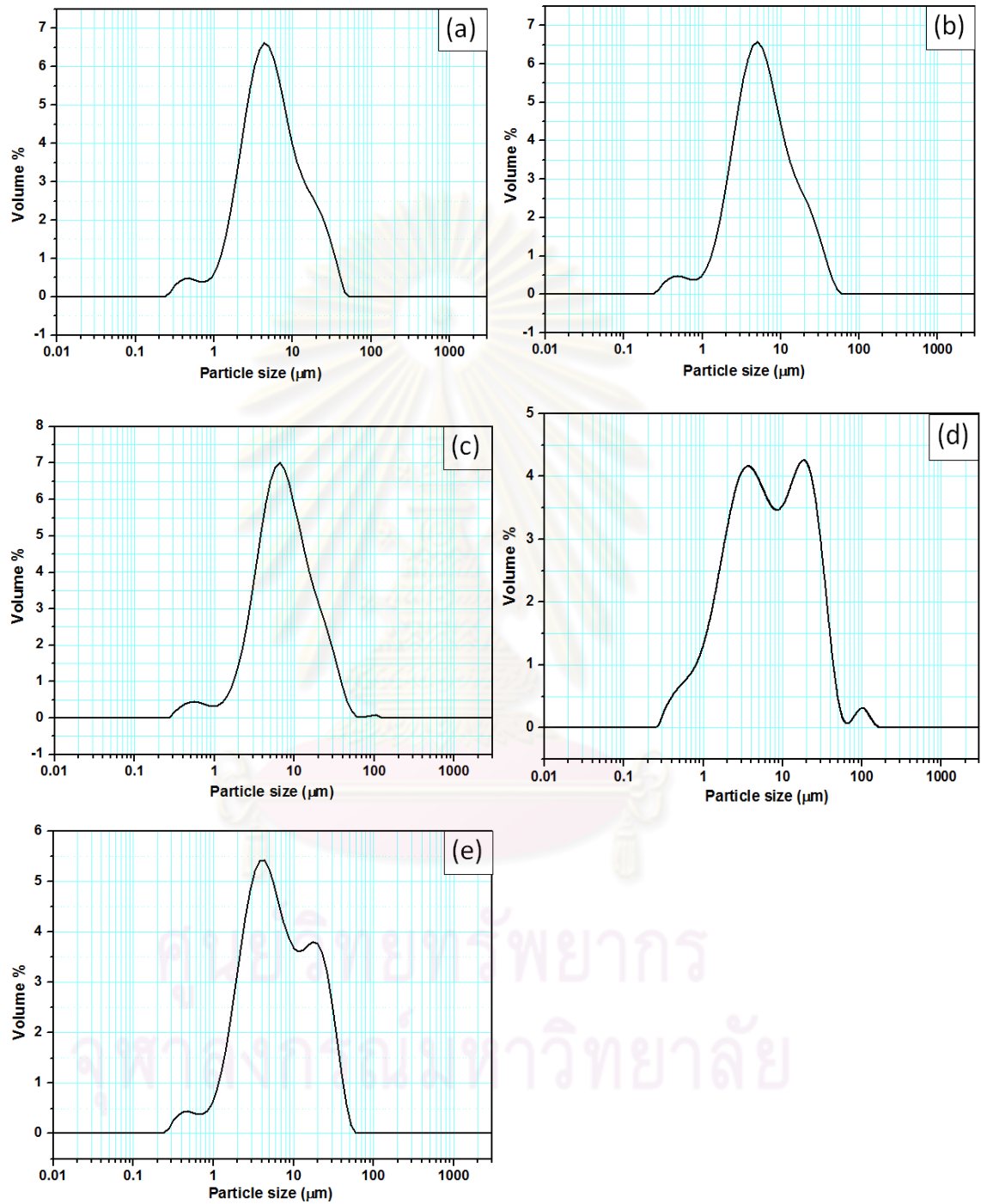


Figure A.3: The particle size distribution of nano-Y₂O₃-BYZ (a) 6 at.% (b) 10 at.% (c) 20 at.% (d) 30 at.% (e) 40 at.%

APPENDIX B

Densities of BYZ Pellet Sample

Table B.1: Relative density of green and sintered bodies of micro-Y₂O₃-BYZ

BaZr _{1-x} Y _x O _{3-δ}	Green body densities(%)	Sintered body densities(%)
x= 0.06	56.92	93.66
x= 0.10	56.58	95.22
x= 0.20	55.86	95.42
x= 0.30	55.33	92.67
x= 0.40	54.05	83.32

Table B.2: Relative density of green and sintered bodies of nano-Y₂O₃-BYZ

BaZr _{1-x} Y _x O _{3-δ}	Green body densities(%)	Sintered body densities(%)
x= 0.06	57.81	98.43
x= 0.10	57.70	98.70
x= 0.20	56.33	98.90
x= 0.30	57.35	98.60
x= 0.40	55.20	97.16

APPENDIX C

JCPDS

BaZrO₃ (JCPDS no. 00-006-0399)

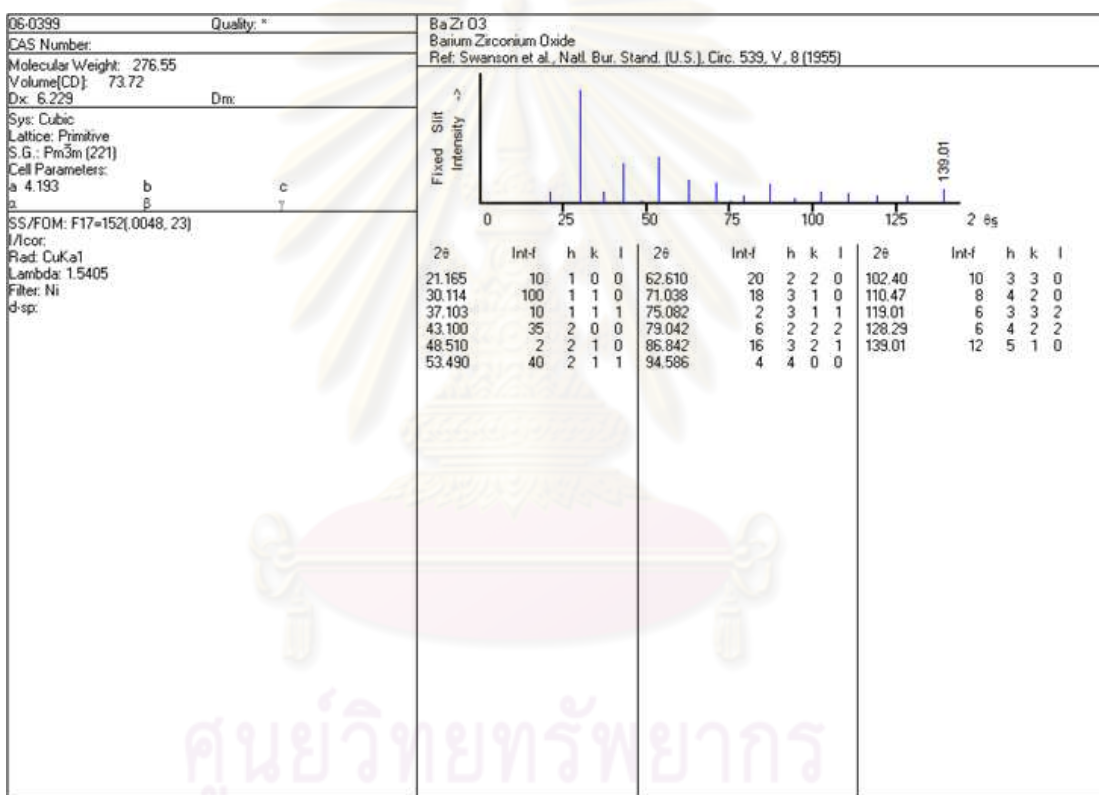


Figure C.1: The JCPDS of Barium Zirconate

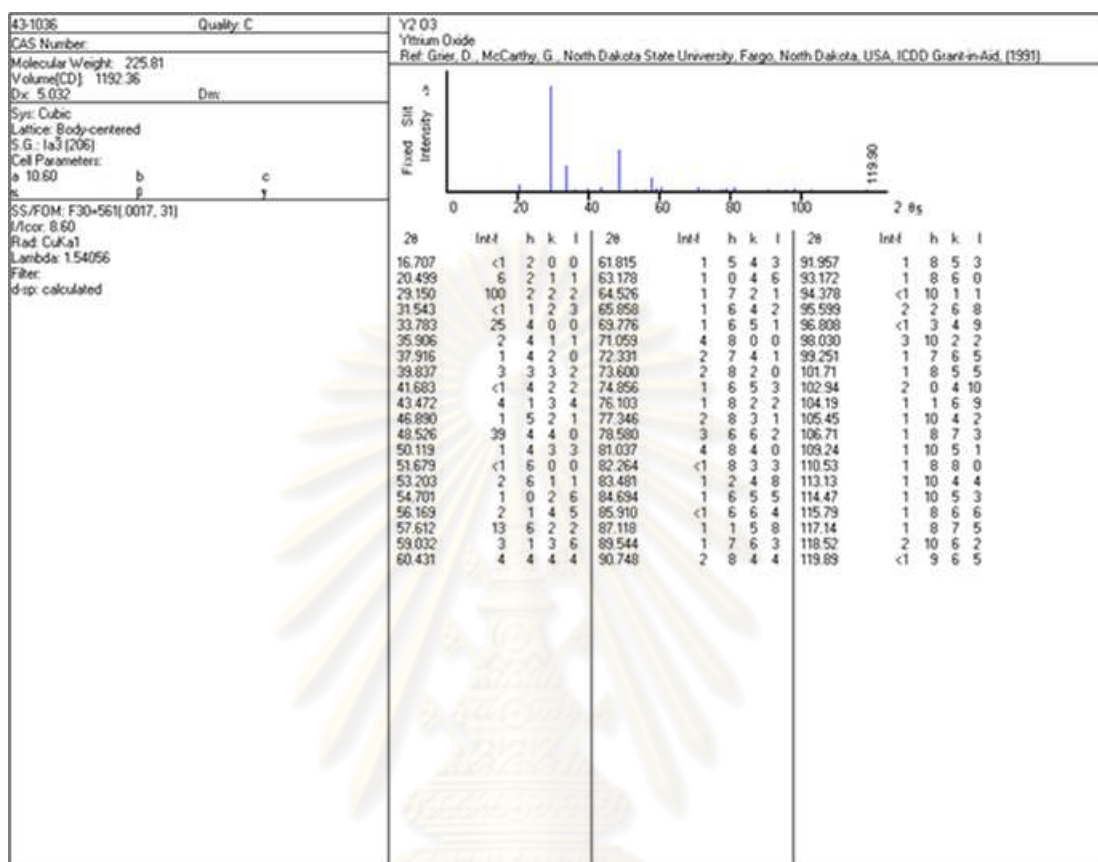
Y_2O_3 (JCPDS no. 00-043-1036)


Figure C.2: The JCPDS of Yttrium Oxide

ศูนย์วิทยทรัพยากร
จุฬาลงกรณ์มหาวิทยาลัย

YSZ (JCPDS no. 00-030-1468)

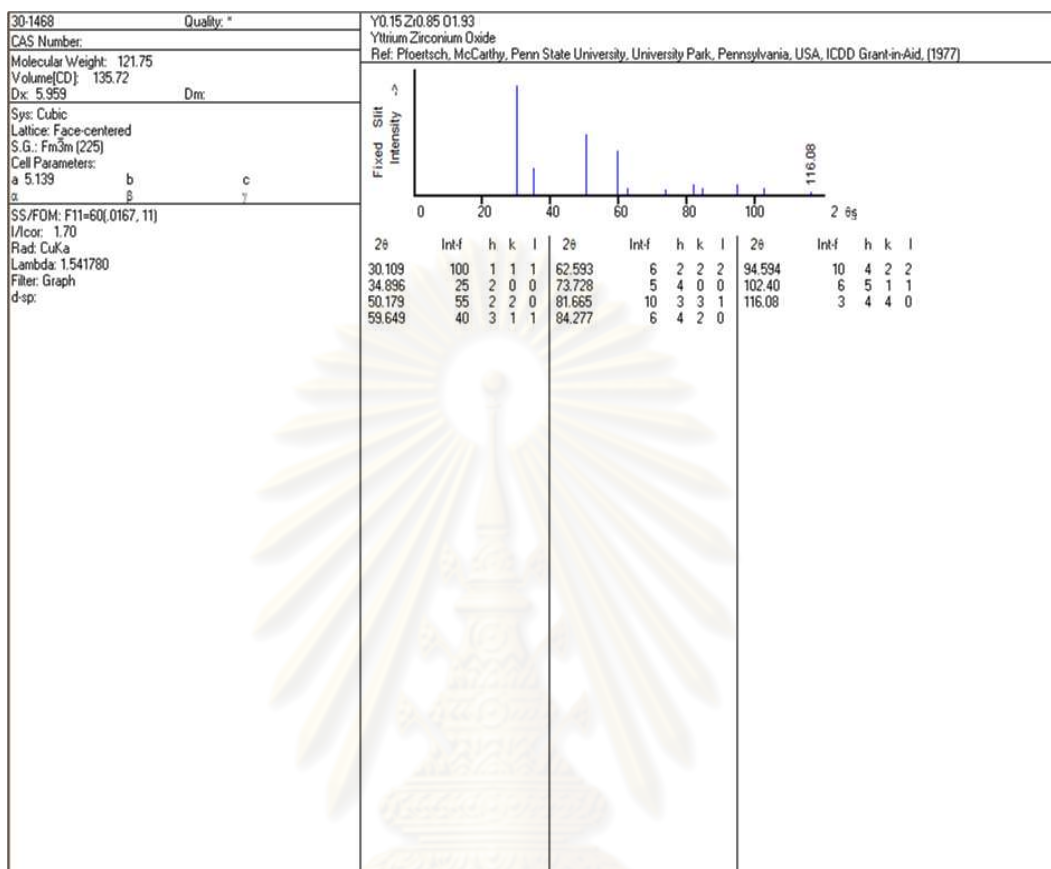


Figure C.3: The JCPDS of Yttrium Zirconium Oxide

ศูนย์วิทยทรัพยากร
จุฬาลงกรณ์มหาวิทยาลัย

VITAE

Miss. Onthida Kosasang was born on October 15, 1985 in Sakonnakhon province, Thailand. She has obtained the Bachelor Degree of Science in Physics from Khon Kaen University in 2006. She continued her further study in Master's degree in the field of Ceramic Technology at Chulalongkorn University and graduated in 2009. She has been supported the education by the Development and Promotion of Science and Technology Talent scholarship (DPST) since high school to Master's degree.

Publications:

O. Kosasang, K. Somroop , P. Chindaudom and R. Pornprasertsuk. Effect of doping concentration on the proton conductivity of Y-doped BaZrO₃ thin films. *ECS Transactions* 19,27 (2009): 145-151.

R. Pornprasertsuk, **O. Kosasang** , K. Somroop, S. Jinawath and F. B. Prinz. Proton conductivity studies of Y-doped BaZrO₃: Theoretical and experiment approaches. *ECS Transactions* 25,35 (2010): 367-381.

Sangwanna. U, Buaheepkaew. M, **Kosasang. O** and Saewong. P. Properties of waste derived mullite. *Material Science Forum*, 544-545 (2007) : 605-608